UNIVERSIDADE DA BEIRA INTERIOR
Engenharia

Substitution of a conventional Gas Turbine by a HT-PEMFC APU

Feasibility Study

(Versão revista após discussão)

Bruna Carolina Castro Pereira Araújo

Dissertação para obtenção do Grau de Mestre em

Engenharia Aeronáutica

(ciclo de estudos integrados)

Orientador: Prof. Doutor Francisco Miguel Ribeiro Proença Brójo

Covilhã, junho de 2019

To my parents and nephew.

”We cannot solve a crisis without treating it as a crisis…if solutions within the system are so impossible to find, then… we should change the system itself.”
-Greta Thunberg

Acknowledgments

I would first like to express my sincere gratitude to my advisor, Professor Francisco Brójo, who guided me and was always patiently willing to help me. His office was always open whenever I ran into a trouble spot or had a question about my research or writing. He consistently allowed this work to be my own work but steered me in the right direction whenever I needed it.

I would also like to thank my colleagues at Universidade da Beira Interior, for their amazing support and friendship. Ana, André, António, Cátia, Coelho, Daniel, Francisco, Ginja, Gonçalo, Inês, Nídia, Nuno, Maria, Oliveira, Paulo, Rodolfo, Rocha and Mister Romeiro. I could never thank you enough for all this journey we spent together.

In addition, I would like to thank my family, especially my parents and my brother for their invaluable efforts and trust. You are always there for me. And for everything you have done, there are no words to express my gratitude and love towards you.

I would also like to thank my boyfriend for the incredible support, patience, and help at all times.
Finally, there are my friends, who were incredible and indispensable during this journey. Ana, Andreia, Beatriz Coelho, Beatriz Silva, Dévora, Jó, João, Joana, Liliana, Luís, Maria, Rita, Rui and Sofia. Thank you for helping me stay focused and for being a happy distraction when I needed one.

Resumo

Uma Unidade Auxiliar de Energia (APU) é um sistema bastante utilizado na produção de energia elétrica em aeronaves. Alcançar melhorias na economia de combustível desses veículos depende diretamente do tipo e do ponto de operação da APU. Essas melhorias devem estar focadas não só na redução dos custos de operação e manutenção, mas também na redução ou até mesmo eliminação de emissões e ruídos. A evolução de uma APU é, portanto, uma questão importante para todos aqueles que direta ou indiretamente estão associados a um aeroporto.

Este trabalho aborda um sistema APU de uma célula de combustível de membrana polimérica de troca protónica de alta temperatura (HT-PEMFC) usado como caso de estudo e sugerido como uma alternativa mais sustentável para o Airbus A320. Por conseguinte, existem três objetivos principais para este trabalho, onde o estudo e a implementação de medidas operacionais de uma ferramenta de software através do MATLAB é a chave para realizá-las.

O primeiro objetivo é analisar vários parâmetros de um HT-PEMFC, a fim de prever o comportamento da célula. Além disso, uma vez que a operação da pilha depende do combustível fornecido ao sistema, que neste caso é o metano, e que este não pode ser diretamente alimentado ao HT-PEMFC, é necessário o processamento do combustível. Para isso é feita uma Reforma de Metano a Vapor e uma Reação de Deslocamento de Água a fim de produzir um gás rico em hidrogénio e com uma baixa percentagem de monóxido de carbono. A máxima potência de saída deste sistema fornecido com metano é estimado em 250 kW para uma temperatura de operação da célula de 180℃ e sob uma pressão de 1.5 atm. As eficiências globais de energia e exergia alcançadas para este sistema são de 41.29 % e 39.95 %, respetivamente.

O segundo objetivo é realizar a análise termodinâmica do sistema HT-PEMFC APU baseada na primeira e segunda leis da termodinâmica. As equações de balanço de massa, energia, entropia e exergia são escritas e aplicadas ao sistema e a cada um dos seus componentes. As irreversibilidades ocorridas nas diferentes unidades do sistema integrado são investigadas através da análise de exergia destruída nessa unidade. Deste modo, as unidades com maior destruição exergética estão associadas às reações químicas que nelas sucedem.

O último objetivo tem como função encontrar o ponto de equilíbrio entre o aumento de peso do sistema proposto (HT-PEMFC APU) e o combustível economizado devido à sua maior eficiência. Visa ainda comparar as emissões de gases de escape entre os dois sistemas, para um mesmo voo realizado por um Airbus A320 entre Porto e Frankfurt.

Finalmente, os resultados desta pesquisa são muito encorajadores, e mesmo que o seu potencial de economia seja improvável de ser alcançado num cenário real devido à natureza e imprevisibilidade do tráfego aéreo, é uma solução atraente para países que enfrentam uma legislação cada vez mais forte e, deste modo, garantir um ar mais limpo e um futuro mais sustentável.

Palavras-chave

APU, HT-PEMFC, Célula de Combustível, Reforma a Vapor, Reacção de Deslocamento da Água, Balanços Termodinâmica, Energia, Exergia, Emissões, Pesos Preliminares

Abstract

An Auxiliary Power Unit (APU) is a system widely used for electric power generation in aircraft. The improvements in fuel economy and emissions of these vehicles directly depend on the type and operating point of the APU. These improvements should not only concern reducing operating and maintenance costs, but also emissions and noise. Improving an APU is, therefore, an important issue for all those directly or indirectly associated with an airport.

This work deals with a High-Temperature Proton Exchange Membrane Fuel Cell (HT-PEMFC) APU system used as a case study and suggested as a more sustainable alternative for the Airbus A320. Consequently, there are three main goals for this work, where the study and implementation of operational measures in a software tool using MATLAB is the key to accomplishing them.

The first objective is to analyze several parameters of a HT-PEMFC, in order to predict the behavior of the fuel cell as a stack. In addition, since the operation of the stack depends on the fuel supplied to the system, which in this case is methane, and that methane cannot be directly fed to the HT-PEMFC, a previous fuel process is necessary. Therefore, Methane Steam Reforming and Water Gas Shifting processes are implemented to produce a hydrogen-rich gas with a low percentage of carbon monoxide. The maximum output power of this methane-supplied system is estimated at 250 kW for an operating temperature of 180°C under 1.5 atm of pressure. The overall energy and exergy efficiencies achieved for this system are 41.29 % and 39.95 %, respectively.

The second objective is to perform the thermodynamic analysis of HT-PEMFC APU based on the first and second laws of thermodynamics. The mass, energy, entropy, and exergy balance equations are written and applied to the system and its components. The irreversibilities occurring in different devices of the integrated system are investigated through the exergy destruction analysis in those units. The units with the most significant exergy destruction are associated with the chemical reactions that occur in them.

The ultimate goal is to find the breakeven weight between the additional weight of the HT-PEMF proposed system and the fuel saved due to higher efficiency of the system. Moreover, it compares the emissions of the conventional APU and the HT-PEMFC systems, during a flight from Porto to Frankfurt carried out by an Airbus A320.

Finally, the results of this research are very encouraging, and even though its fuel consumption saving potential is unlikely to be achieved in a real-world scenario due to the nature and unpredictability of air traffic, it is an attractive solution for countries facing ever stronger legislation to ensure cleaner air and a more sustainable future.

Keywords

APU, HT-PEMFC, Fuel Cell, Steam Reforming, Water Gas Shifting, Thermodynamic Balances, Energy, Exergy, Emissions, Preliminary Weights.

Contents

List of Figures

List of Tables

Acronyms List

AC	Alternating Current
AEA	All Electric Aircraft
APU	Auxiliary Power Unit
ATRA	Advanced Technology Research Aircraft
CC	Combustor Chamber
DC	Direct Current
DEPFC	Direct Ethanol Polymer Fuel Cell
ETOPS	Extended Twin Operations
FC	Fuel Cell
FT	Fischer-Tropsch
GT	Gas Turbine
HT-PEMFC	High Temperature Proton Exchange Membrane Fuel Cell
HRSG	Heat Recovery Steam Generator
HX	Heat exchanger
ICAO	International Civil Aviation Organization
ISA	International Standard Atmosphere
LT-PEMFC	Low Temperature Proton Exchange Membrane Fuel Cell
MEA	More Electric Aircraft
ORC	Organic Rankine Cycle
PEM	Polymer Electrolyte Membrane
PEMFC	Polymer Electrolyte Membrane Fuel Cell
SOFC	Solid Oxide Fuel Cell
SOFC-GT	Solid Oxide Fuel Cell - Gas Turbine
SR	Steam Reformer
MSR	Methane Steam Reforming
UAV	Unmanned Aerial Vehicle
WGS	Water Gas Shifting

Nomenclature

a_{H_2O}	Water activity
A_{cell}	Active surface area of the cell, m^2
c_p	Specific heat capacity at constant pressure, $\mathrm{J\,mol^{-1}\,K^{-1}}$
C_i	Specie i concentration
C_i^0	Reference standard concentration of specie i, $\mathrm{mol\,cm^{-1}}\ atm^{-3}$
$C_{i,Pt}$	Specie i concentration in the thin film at platinum-electrolyte boundary, $\mathrm{mol\,cm^3}$
$C_{dissolve}$	Hydrogen and oxygen concentration in the thin film at gas pore-electrolyte boundary, $\mathrm{mol\,cm^3}$
D_i	Diffusion coefficient of specie i
D^{PA}	Diffusion through ionomer, $\mathrm{cm^2\,s^{-1}}$
D_{ij}^{eff}	Effective binary diffusion, $\mathrm{cm^2\,s^{-1}}$
ex	Specific exergy, $\mathrm{kW\,kmol^{-1}}$
ex_{ch}	Chemical exergy, $\mathrm{J\,mol^{-1}}$
ex_{ch}^0	Standard chemical exergy, $\mathrm{kW\,kmol^{-1}}$
ex_{ph}	Physical exergy, $\mathrm{J\,mol^{-1}}$
E^0	Ideal cell voltage at standard conditions, V
E_{rev}	Nernst potential, V
E_{act}	Activation energy, $\mathrm{J\,mol^{-1}}$
$\dot{E}x$	Exergy, kW
$\dot{E}x_{dest}$	Exergy destruction rate, kW
F	Faraday constant, $96\,485\,\mathrm{C\,mol^{-1}}$
g	Gravitational acceleration, $9.81\,\mathrm{m^2\,s^{-1}}$
G^0	Gibbs potential, $\mathrm{J\,mol^{-1}}$
h	Specific enthalpy, $\mathrm{J\,kmol^{-1}}$
h_i^0	Enthalpy at standard conditions, $\mathrm{J\,kmol^{-1}\,K^{-1}}$
h_f^0	Standard enthalpy of formation, $\mathrm{kJ\,kmol^{-1}}$
H	Henry's constant for the given species solubility in the electrolyte, $\mathrm{m^3}atm\ \mathrm{mol^{-1}}$
i	Current density, $\mathrm{A\,m^{-2}}$
i_0	Exchange current density, $\mathrm{A\,m^{-2}}$
i_0^{CO}	Exchange current density for hydrogen oxidation after CO poisoning
i_0^{ref}	Exchange current density at reference temperature, $\mathrm{A\,cm^{-3}}$
$\dot{I}$	Irreversibility, kW
I	Current, A
I_{cell}	Cell current, A
I_{stack}	Stack current, A
K_{eq}	Equilibrium constant
l_m	Membrane thickness, m
LHV	Lower Heating Value, $\mathrm{J\,mol^{-1}}$
L/D	Lift to drag ratio
L_c	Catalyst loading, weight of platinum per unit area, $\mathrm{mg\,cm^{-2}}$
m	Mass, g
$\dot{m}$	Mass flow rate, $\mathrm{kg\,s^{-1}}$
M	Molecular weight, $\mathrm{g\,mol^{-1}}$
n	Mole number, mol
$\dot{n}$	Molar flow rate, $\mathrm{mol\,s^{-1}}$

N_c	Number of cells
N_{mod}	Number of modules
pp	Partial pressure, Pa
P	Pressure, Pa
P_0	Environmental dead state pressure, Pa
P_{an}	Pressure at anode, Pa
P_c	Gas critical pressure, Pa
P_{ca}	Pressure at cathode, Pa
P_{fc}	Fuel cell pressure, W
P_{ref}	Reference pressure, Pa
P_{tot}	Pressure of the flow at the reformer, Pa
$p^*_{H_2O}$	Saturation vapor pressure of pure water at given temperature, atm
$\dot{Q}$	Heat transfer rate, W
R	Universal gas constant, $8.3145\,\mathrm{J\,mol^{-1}\,K^{-1}}$
RH	Relative humidity, %
s	Specific entropy, $\mathrm{J\,mol^{-1}\,K^{-1}}$
s^0_i	Entropy at standard conditions, $\mathrm{J\,kmol^{-1}\,K^{-1}}$
sfc	Specific fuel consumption, $\mathrm{mg\,N^{-1}\,s^{-1}}$
$\dot{S}_{gen}$	Entropy generation rate, $\mathrm{W\,K^{-1}}$
S_{Pt}	Surface area of platinum (Pt) per geometric electrode area,
t	Time, s
t_{GDL}	Gas diffusion layer thickness, m
T	Temperature, K
T_0	Environmental dead state temperature, K
T_c	Gas critical temperature, K
T_p	Saturation temperature, K
T_{ref}	Reference temperature, K
U_a	Air utilization ratio
U_f	Fuel utilization ratio
$V_{act,an}$	Activation losses at anode, V
$V_{act,ca}$	Activation losses at cathode, V
V_{ohm}	Ohmic resistance, V
V_{cell}	Output cell voltage, V
$\dot{W}$	Power, W
$\dot{W}_{APU}$	APU electrical power output, W
$\dot{W}_{comp,a}$	Air compressor power, W
$\dot{W}_{comp,f}$	Fuel compressor power, W
$\dot{W}_{fc}$	Fuel cell stack electrical power output, W
$\dot{W}_p$	Pump power, W
$\dot{W}_t$	Turbine power, W
X	Mole fraction
z	Number of electrons

Greek symbols

α	Charge transfer coefficient
β	Electro-osmotic drag coefficient of water
δ	Component thickness, m
$\Delta\bar{h}$	Enthalpy change, $\mathrm{J\,kmol^{-1}}$
ΔG	Standard Gibbs free energy of a reaction, kJ
ΔH^0	Standard enthalpy change, $\mathrm{J\,mol^{-1}}$
ΔP	Boost in pressure of liquid water, Pa
ΔS^0	Standard entropy change, $\mathrm{J\,mol^{-1}\,K^{-1}}$
η	Energy efficiency
γ	Ratio of specific heats
κ	Reaction order
σ	Conductivity, $\mathrm{S\,cm^{-1}}$
λ	Fuel to air ratio
ψ	Exergy efficiency
τ	Tortuosity
θ_{CO}	Fraction of catalyst surface covered by CO
ε	Porosity, %
υ	Specific volume, $\mathrm{m^3\,kg^{-1}}$
φ	Air stoichimetry
ω	Phosphoric acid weight concentration, wt%

Subscripts

a	Air
act	Activation
an	Anode
c	Critic
ca	Cathode
cog	Cogeneration
comp	Compressor
cc	Combustion chamber
dest	Destruction
ele	Electrical
eg	Exhaust gases
f	Fuel
fc	Fuel cell
fp	Fuel processor
F	Flight
gen	Generation
i	Stream
j	Specie
ohm	Ohmic
r	Reformer
ref	Reference
rev	Reversible
sat	Saturation
st	Steam
t	Turbine
th	Thermal
w	Water shifting

Chapter 1

Introduction

1.1 Motivation

Since dawn of mankind, energy is the matter that drives evolution. Energy is the origin of a major technological progress and its increasing people's quality of life, but at what price?
The world has witnessed a frightful energy condition. Frightful because traditional resources are coming to an end, and its massive exploitation is sideways with our health, our economy and our environment.
For the last two centuries, the world energy condition to rely on obsolete energy, more precisely, fossil fuels is literally being fatal. These non-renewable energies are accountable for irreversible environmental damage, causing many diseases and the dreadful wars in their profit.
After the Industrial Revolution and especially after World War II, enormous amounts of carbon dioxide were released to the atmosphere, from industrial activity. Since the beginning of industrialization, 200 years ago, the planet suffered the fastest environmental changes in the history of the Earth.
Nonetheless, carbon dioxide is one of the most important gases in our atmosphere and is one of the greenhouse effects responsible for making this planet habitable. The problem starts when the emissions are in colossal scale and increase the planet capacity to absorb the infrared radiation, influencing its natural balance of energy.
The consequences of relying on fossil fuels are starting to be notable at plain sight, where glacial melting is an example. As the reason for that, it is important to understand what activities are in the origin of these emissions to study different ways to improve or even replace it for zero-emissions technology.
Nowadays, the outcome polution of the transport sector is one of the major responsible accounting for 14% of greenhouse emissions, where 3% is coming from the aviation industry [1, 2]. From those 3 %, the airport ground-based emissions coming from Auxiliary Power Unit (APU) holds 20% [3].
APU is an auxiliary power unit used in most commercial aircraft, some private jets and helicopters which the main purpose is to provide electrical, pneumatic and hydraulic power to the aircraft. Nevertheless, APU is the cause of 50% of the aircraft maintenance costs, 12% of delays and more than 5% of the daily fuel consumption [1, 3, 4].
The degradation of quality of life by the increasing number of airplanes and routes on the aviation industry is not only provided from air pollution, the hazards of noise pollution and how it influences human physical and psychological health have to be considered.
Aware of this increasing problem that was compromising the planet, the United Nations Organization defended that a more restricted environmental and energetic policy to control the greenhouse gas emissions was required, which was proposed in 1997 to most of the industrialized countries, designated Kyoto's Protocol[1], and more recently the Paris Agreement was approved in 2015.
However, the challenge is urgent when the safety of the planet is at risk, and the need to replace fossil energy for cleaner ones is inevitable [5]. Renewable energies can play a driving role in overcoming the threats of decline and collapse.
The solution goes through finding new lasting and non-polluting energy sources able to respond or even overcome today's needs. Accordingly, these concerns led to a tremendous progress in the efforts to move

[1]Ratification by at least 55 states to the Convention, effective from February 12^{th} 2005 to December 31^{st} 2012. https://unfccc.int/resource/docs/convkp/kpeng.pdf

towards more electric aircraft (MEA) or even all electric aircraft (AEA). A renewable energy system will result in a zero emission, noise reduction flight using an AEA, and once adapted in large scale could reduce the aviation sector percentage on greenhouse emissions. In this regard, the base of this work is studying the replacement of the conventional APU for a more rationally-efficient component.
Fuel cells show high potential with outstanding efficiency and clean energy [6]. For that reason, herein a promising alternative to the current APU is presented. Fuel cells can serve as an emergency power source and continuously produce electrical energy to supply an entire flight [7, 8]. This renewable energy system, usually fueled by hydrogen, is being applied to cars and trucks, and the aeronautical industry is already making progress in this area.
There are two types of fuel cells that stand out for aeronautical application: low-temperature proton exchange membrane fuel cell (LT-PEMFC) and high-temperature solid oxide fuel cell (SOFC) [9]. More recently, a direct ethanol polymer fuel cell (DEPFC) for APU application was tested [10].
The APU technology studied in this work is a high-temperature proton exchange membrane fuel cell (HT-PEMFC) with the purpose of a more sustainable aircraft.
In this brief reflection, renewable energies compromise a world of unending opportunities which can be looked with enthusiasm and hope. The opportunity to live in a safer world goes through the study and implementation of these sustainable energies capable of establishing a symbiotic relationship between technology and the environment. In this study, the potential of exergy analysis for the environment and sustainable development implications are reviewed.

1.2 Objectives

In general, the objective of the present work is to verify the feasibility of replacing the conventional gas turbine by a high-temperature proton exchange membrane fuel cell APU. A process of hydrogen energy recovery qualified to provide auxiliary power to the aircraft on the ground and during flight. More specifically, the goals are:

- Understand fuel processing of natural gas into hydrogen and its conversion into electric energy through a fuel cell;
- Build a mathematical model for a high-temperature proton exchange fuel cell using reformed fuel;
- Study the system using the first and second law of thermodynamics (energetic and exergetic analyses);
- Identify and evaluate the irreversibilities within the process;
- Estimate the weight of the HT-PEMFC APU;
- Determine the system global performance.

1.3 Dissertation Outline

This dissertation is structured into six chapters. The first and current chapter consists of a brief presentation and organization of the topic. Furthermore, the major reasons for the development of this work and its importance for the future are assigned .

Chapter 2 consists of a literature review on the major topics addressed through this dissertation. A detailed APU introduction is followed by the methodology and approach used.

The case study of this work is presented in Chapter 3. There is a presentation of the overall system proposed and the validation of that system.

In Chapter 4, a mathematical model for fuel processor and fuel cell are described. Additionally, some important tools used in the model validation are introduced.

In Chapter 5, results are interpreted and explained. Also, the viability of the system is analyzed and discussed.

This dissertation is concluded in Chapter 6, where a global analysis, difficulties and conclusion are discussed as well as the suggestion of identified future topics for future work opportunities.

Chapter 2

Literature Review

In this chapter, the history of the auxiliary power unit and its general concept are introduced. The different types of APUs already in activity or under research are presented and described.
A more detailed review of the concepts of fuel cell-based APU and its main design considerations are explained. In addition, the concepts of energy and exergy, along with their importance for this work, are introduced.
Finally, the thermodynamic model for the validation of the system is described. This part will be the basis for the methodology developed.

2.1 History of the APU

During World War I, the first auxiliary engine was used on the British Coastal class blimp. In a time where radio proved indispensable to communication with another recent development, airplanes, the APU supplied the power for radio transmissions, and in case of an emergency, could power an auxiliary air blower. One of the first records of a military fixed-wing aircraft to have an APU in its design was the Supermarine Nighthawk (see Figure 2.1), an anti-Zeppelin Night fighter whose function was to power a searchlight.

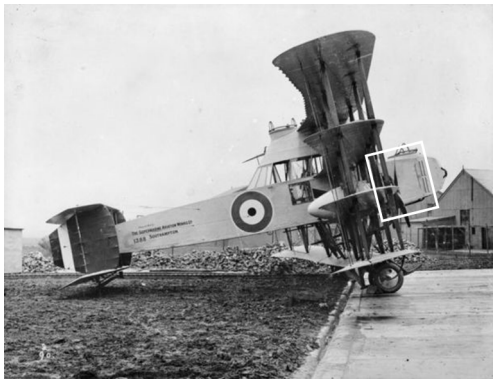

Figure 2.1: Supermarine PB31E Nighthawk with an auxiliary power unit installed aft of the main engine [11].

Later, during World War II, the first operational jet engine was built, the Junker Jumo 004 (see Figure 2.2a). Its operation depended on a starter system, which was designed by the German engineer Norbert Riedel. One of the models developed by Riedel operated as a manual pull-handle to start the piston engine, which in turn rotated the compressor. The system consisted of a 7.5 kW two-stroke flat engine considered as the pioneering example of a mechanical auxiliary power unit to start the main engine and was built into the nose-cone of the turbojet as presented in Figure 2.2b [12].

Meanwhile, US military aircraft were also being equipped with APUs, typically known as putt-putts, even in official training documents. The putt-putt on the Boeing B-29 Superfortress bomber was fitted in the unpressurized section at the rear of the aircraft. Various models of four-stroke, Flat-twin or V-twin engines were used. The putt-putt provided power for starting the main engines and was used after take-off to a

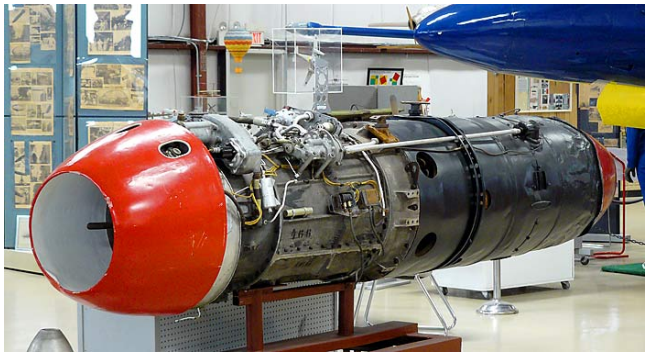

(a) Junker Jumo 004 - the first axial-flow turbojet.

(b) Riedel APU used to start the Junker Jumo 004.

Figure 2.2: Turbojet Junker Jumo 004 started with a a Riedel APU [13].

height of 3,000 m, and restarted when the B-29 was descending to land [12].
In 1963, the Boeing 727 was the first commercial aircraft to have an operating gas turbine APU providing electrical energy, legally allowed at smaller airports.
Nowadays, APUs are powering regional, executive, commercial and military airplanes including both fixed wing and rotary wing.

2.2 Auxiliary Power Unit

The auxliary power unit or APU is a self-contained unit responsible for providing electrical, pneumatic and hydraulic power to the aircraft, on the ground and during flight. These forms of power can be directly provided or converted using additional onboard equipment - e.g. valves for hydraulic energy [14, 15].Generally located at the rear of the aircraft due to its void space and the need for an opening to expel the exhaust gases [14, 16]. The APU relies on ambient air and fuel from the engines to produce compressed air and electricity. The air intake for the APU is located underneath the tail cone as shown in Figure 2.3, and the opening is controlled by an electrical flap which allows external air to reach the compressor inlet. The fuel is provided from fuel tanks and is the same fuel used for main engines. The APU requires an integral independent oil system for lubrication and cooling [15].
An APU is an engine for functions other than propulsion. Actually, the purpose of an APU is to make the

Figure 2.3: Maintenance of an APU onboard of a A320 [17].

airplane self sustainable on the ground and providing the additional source of power during flight. Figure 2.4 shows the different applications of power required for the aircraft operation and presents detailed

information on their power consumption.

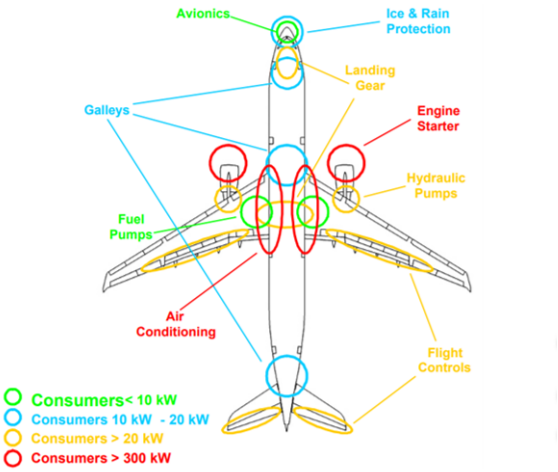

Figure 2.4: Distribution of energy for the airplane and its power consumption [6].

During ground operations, the APU supports the electric and pneumatic systems even before the main engines start. This way saves fuel since the engines are only turned on for take-off time. Furthermore, it supplies bleed air for starting the engines and air conditioning system. During take-off still supplies bleed air for air conditioning, thus avoiding a reduction in engine thrust caused by the use of engine bleed air for this purpose when optimum aircraft performance is required. Is responsible for backing up the electrical and pneumatic systems in flight and can be used in emergency situations, such as engine failure. In that case, APU has to assure the operation of electrical power for the avionics and the hydraulic power to control the control surfaces [14].

Accordingly to literature, the APU is a fundamental system for flights with two-engine aircraft and long routes over water or terrain without an alternative airport - Extended Twin Operations (ETOPS) flights. Moreover, if the aircraft safety architecture depends on an available APU is indispensable to have one [15].

2.3 Types of APU

Figure 2.5 highlights APUs already in use or under research with an aeronautical application in view.

2.3.1 Gas Turbine APU

A gas turbine is the conventional APU used in airplanes, favorable for its high power-to-weight ratio [18]. The base design is a single-shaft gas turbine, powering an electrical generator and an air compressor, operating accordingly with the Brayton thermodynamic cycle. As demonstrated in Figure 2.6b the Temperature-entropy (T-s) diagram of the Brayton cycle starts with inlet air (0-2) being compressed (2-3) to increase its pressure and temperature, afterward fuel is injected and mixed with hot air for combustion (3-4). Finally, the exhaust gases pass through the turbine (4-5) and are exhausted through the nozzle (5-8) [18].
The gas turbine APU can be divided into three main sections, as presented in Figure 2.6a:

- The power section is a turbine engine and produces all the power for the APU;

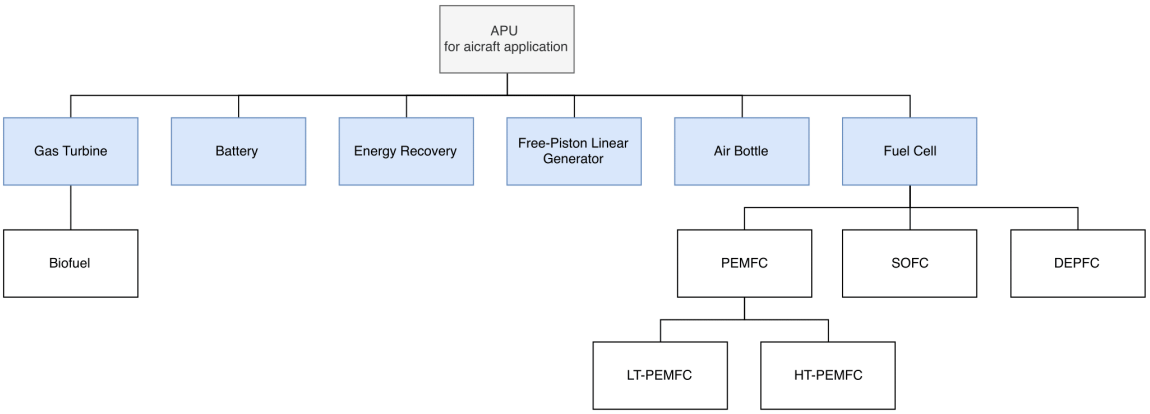

Figure 2.5: Types of APUs for aircraft application

- The load compressor is responsible for supplying all the pneumatic pressure to the aircraft;
- The gearbox transfers the APU power to an electric generator that in turn supplies electricity to the airplane.

The power source of an APU is generally a battery or a hydraulic accumulator [14].

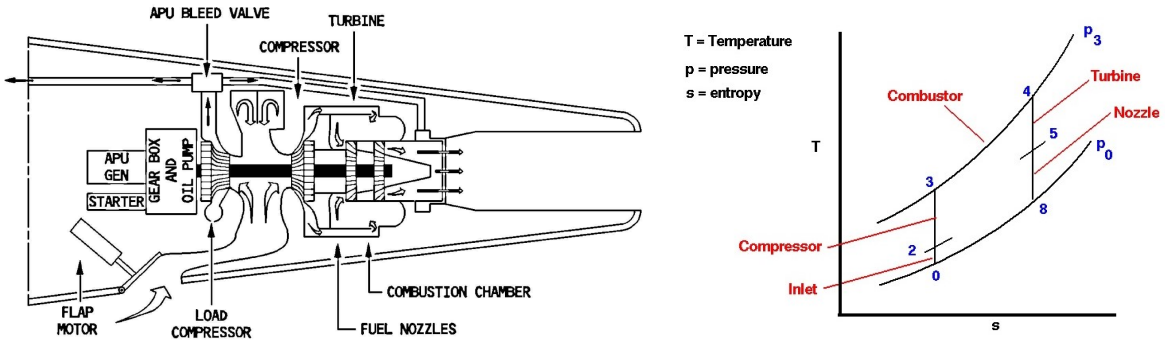

(a) Gas Turbine APU sections [15].

(b) T-s diagram of Brayton Cycle [19].

Figure 2.6: Typical gas turbine APU (on the left) using the Brayton cycle (on the right).

The design of the gas turbine APU has hardly changed over time, keeping the concept of single cycle gas turbine and reliable technology. The technological reliability is a strong feature when it comes to costs and compatibility with existing aircraft architectures [15]. In contrast, presents relatively low efficiency (30-40% in flight and less than 20% on the ground), high noise and environmental pollution and requires high maintenance support [20, 21]. Nevertheless, it is important to note that APU manufacturers are making efforts towards increasing fuel savings and the life cycle of the APU while decreasing its maintenance. Environmental regulations on air quality and vehicle exhaust emissions and noise are placing severe restrictions in the aviation sector. In fact, International Civil Aviation Organization (ICAO) has developed Strategic Objective C, Environmental Protection. ICAO proposition aims to minimize the adverse effects of global civil aviation on the environment, which can be attained by developing, adopting, and promoting new or amended measures to:

- Limit or reduce the number of people affected by significant aircraft noise.
- Limit or reduce the impact of aviation emissions on local air quality.
- Limit or reduce the impact of aviation greenhouse gas emissions on the global climate.

The growing demand for air transport results in the need to operate with new technologies, such as the use of sustainable energy for auxiliary power generation. This will reduce fuel consumption and emissions from air and land operations while investing in newer and more eco-efficient aircraft.

2.3.1.1 Biofuel auxiliary power unit

An increase on airport operations results in the need to reduce emissions to control air quality within and around airports. One way to minimize the problem is by developing more environmentally friendly fuels, to reduce dependence on petroleum and consequently emissions.

Gasification is the thermochemical conversion of organic material into a valuable gaseous product, called syngas, and a solid product called char. The biomass gasification (BG) represents an efficient process for the production of second-generation biofuels. The Fischer-Tropsch (FT) process is a combination of chemical reactions that convert a mixture of carbon monoxide and hydrogen into liquid hydrocarbons. The synthetic fuel may be generated from coal, natural gas or biomass. BG and FT synthesis can in principle be combined to produce renewable transportation fuels (biofuels).
Carbon efficiency is defined as the proportion of the biomass carbon that ends up in FT products containing at least five carbon atoms. Using conventional FT technology the process ranges in carbon efficiency from 25 to 50 % and thermal efficiency of about 50% [22, 23]. Tests made to measure the emissions for APUs using a coal-derived FT fuel showed significant reductions on oxygen emissions and particle mass and generation smaller size particles and 10% reduction in CO emissions were observed for the alternative fuels [24, 25].

The use of alternative fuels on APUs reduces the overall aircraft emissions as they present a good compatibility, however the use of a more sustainable aviation fuel is currently minimal and is likely to remain limited in the short term [25, 26].

2.3.2 Energy Recovery APU

An energy recovery APU is an Organic Rankine Cycle (ORC) combined with the main engine to power the aircraft (Figure 2.7). In this concept, instead of releasing the exhaust gases into the atmosphere, the thermal energy is reused.
The heat exchanger that connects both cycles uses the high-temperature exhaust gases from the aircraft engine to provide the thermal energy to the coolant fluid in counter-current. After being heated, the pressurized coolant changes its state. The now vaporized refrigerant goes through the ORC and to a power turbine where it converts the thermal energy into mechanical and then into electric energy through a generator. The low boiling point of the cold fluid increases the enthalpy of the working fluid so that it is possible to generate energy through a turbine without the need for a compressor [27]. Nevertheless, the system requires a pump to increase the pressure of the refrigerant to the turbine operation.

A major advantage of this configuration is the capacity to operate throughout the entire flight envelope and reducing fuel consumption by harvesting waste heat from aircraft engines. Regarding environmental issues, it is a great improvement of the gas turbine because it minimizes the waste energy discarded to the environment and is a very quiet system since there are almost no moving parts. Nevertheless, the available power is limited to the waste heat, space, efficiency and permissible temperature. Hence, it requires further development for being economically and technologically reliable.
To conclude, Boeing's preliminary analysis showed that 0.5% or more fuel reduction is feasible, hence a $\sim$0.03% reduction in carbon emissions [28].

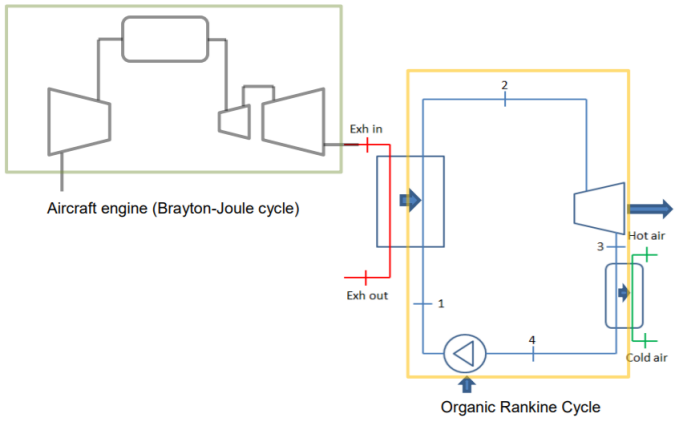

Figure 2.7: A proposed energy recovery APU [27].

2.3.3 Batteries

A battery is a device containing one or more cells that convert chemical energy directly into electrical energy. Engineers have discovered the unlimited potential for its development and improvement, and for that reason they are incorporated in almost every aircraft. For an application where the weight is an issue, the lithium-ion (Li-Ion) batteries are commonly used in aircraft because they exhibit a large energy density.

Usually, airplanes contain two batteries, the main battery and the APU battery (see Figure 2.8). The main battery feeds the aircraft systems even before the engines and the APU start. It is used to support ground operations such as refueling and powering the braking system when the airplane is towed. In addition, the main battery provides backup power for critical systems during a flight in the event of a generation or distribution system failure [29].

Meanwhile, the APU battery supplies power to start the APU, which in turn can start the main engines. Once the engines are running, the electrical energy to power the systems comes from their own generators. A battery is a very efficient source of power and environmentally friendly technology. However, some unfortunate events that occurred with the Boeing 787 called into question the reliability of Li-Ion batteries for aircraft application [30, 31]. Battery overcharging and leakage are some of the threats that can lead to a catastrophic occurrence; therefore, special care and consideration must be taken to ensure safe operations regarding the use and transportation of Li-Ion batteries when in an aircraft environment.

Figure 2.8: Batteries APU system for Boeing 787 adapted from [28].

2.3.4 Air Bottle

This alternative APU uses compressed air as a power storage. Ambient air pressurized by a compressor and stored in a bottle is used by the conversion system to transmit power to the aircraft.

For high-pressure systems, air is usually stored in metal bottles at pressures ranging from 7000 to 21,700 kPa, depending on the particular system. This type of air bottle has two valves, one of which is a charging valve. A ground-operated compressor can be connected to this valve to add air to the bottle. The other valve is a control valve. It acts as a shutoff valve, keeping air trapped inside the bottle until the system is operated. However, the high-pressure storage cylinder is a lightweight system, its operation is limited by the small supply of bottled air as it is not possible to be recharged during flight.
In addition, this system is not designed for continuous operation. Instead, the bottled air supply is reserved for emergency operation of systems such as the landing gear or brakes if, for example, the hydraulic system fails and extend the gear prior for landing depends on an air-driven hydraulic pump (see Figure 2.9), or temporarily systems such as engine start, door sealing or opening, de-icing, driving hydraulic pumps, alternators, starters and water injection pumps [32]. The usefulness of this type of system depends on air-pressurizing units onboard the aircraft. Nevertheless, it is not recommended for large and heavy mechanical devices as it would require a large compression stage to have sufficient energy, and larger air tanks [33].

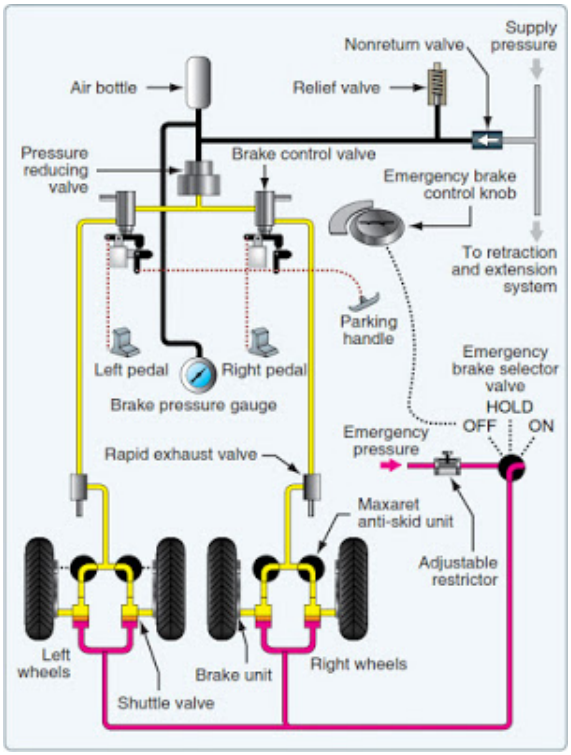

Figure 2.9: Aircraft pneumatic brake system [32].

2.3.5 Free-Piston Linear Generator

A free-piston linear generator (FPLG), as illustrated in Figure 2.10, consists of an internal combustion engine (ICE), a linear electric generator (permanent magnets and electromagnetic coils) and a controllable gas spring. Unlike the conventional ICE, the FPLG converts the linear movement of the piston directly into electrical energy, without resorting to a crankshaft. This concept allows a highly efficient conver-

sion [34, 35, 36]. In addition, the FPLG generates electricity with excellent emission values, meeting the requirements for a technological change [36, 37]. A fuel-air mix is ignited in the combustion chamber driving the piston from the top dead center (TDC) to the bottom dead center (BDC), where the gas spring actuates. During its path, the permanent magnets (rotor) attached to the piston move inside of the electromagnetic coils (stator). The linear motion between stator and rotor results in the generated electric power. At the BDC, the gas spring stores energy in terms of compressed air and returns the piston to the TDC. The FPLG presents a compact, mechanically simple design for an APU that can be man-portable or vehicle distributed. Due to its stiffness, the gas spring works as an actuating variable of the system allowing the engine to achieve a variable compression ratio. Because of that, the FLPG is adaptable to a wide range of fuels as JP-4, JP-8, natural gas, diesel fuels, and other potential alternative fuels [37].

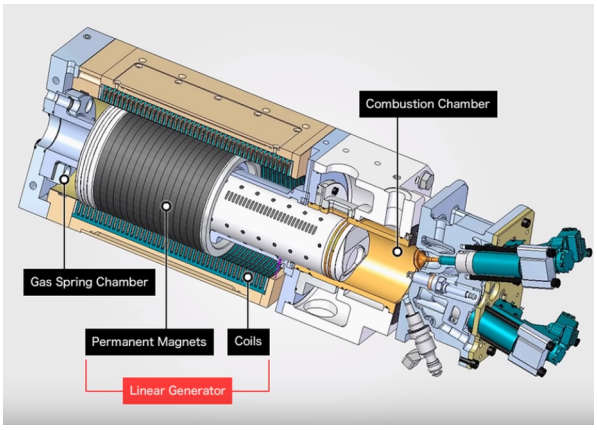

Figure 2.10: Toyota Central RD developing free piston engine linear generators [38].

2.3.6 Fuel Cell Stack

A fuel cell APU is a stack of unit cells electrically connected in series to produce the desired voltage, forming modules. Modules are connected in parallel to obtain the total power for the system stack. The power density of the cells is a crucial parameter for aeronautical applications due to its relation to the weight of the stack. Higher power densities, normally, represent smaller and lighter stacks, however, it has to be within the limits of current density [10].
A unit cell is composed of three components: an anode, a cathode, and an electrolyte. The electrolyte used characterizes the type of fuel cell.
A fuel cell is an electrochemical device that combines fuel and an oxidant to produce electricity. The fuel is typically hydrogen which is supplied to the anode while the oxidant goes to the cathode, with water and heat as the by-products. It is similar to a battery in structure but as long as fuel is supplied it will continue to operate, without the need to recharge. The functionality of a fuel cell is very simple. At the anode there is separation of the hydrogen (H_2), producing positively charged ions (H^+) and electrons. Only the H^+ pass through the electrolyte from the anode to the cathode. Meanwhile, the electrons are forced to migrate out of the electrolyte and through a wire that connects the anode and the cathode, this way electricity is produced . At the cathode, the H^+ ions are recombined with electrons and react with oxygen, producing water (H_2O) as shown in Figure 2.11.
The conversion of chemical energy into electrical energy takes place without combustion occurring, so it is a highly efficient, clean, and quiet process. A significant advantage of the fuel cell APU is that it can store and quickly replenish a large amount of energy, such as the conventional APU [40].

During operation large quantities of heat can be generated, in several cases, part of that heat can be

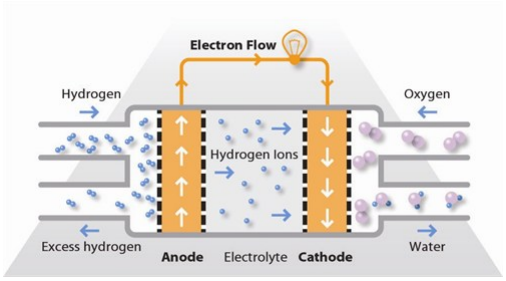

Figure 2.11: Basic schematic of a unit cell [39].

recovered and supplied to other processes [39]. Heating reactants, fuel processing, or expansion in a turbine to produce power from hot output streams are some examples [9]. The remaining fuel is converted irreversibly into heat. The exergy analysis evaluates opportunities for onboard heat recovery from the fuel stack.
Additionally, the re-utilization of the produced pure water by the fuel cell has shown to be profitable for the airplane system, has it no longer requires to carry water on the plane [10].

2.3.6.1 Proton Exchange Membrane Fuel Cell

The current PEMFC technology reports two types of systems, low-temperature (LT-PEMFC) and high temperature (HT-PEMFC) fuel cells, differing in operating temperatures, type of electrolytes and electrocatalyst loadings [41]. PEM fuel cells are highly mature due to its advancements through the automotive industry [6]. The most developed and reliable technology is the LT-PEMFC, which operates at temperatures lower than 100°C. More recently studies have focused on a HT-PEMFC and are showing remarkable developments towards this technology in the aeronautical sector.

LT-PEMFC
LT-PEMFC operates at temperatures between 80 and 100℃ and uses pure hydrogen since it is highly sensitive to sulfur and carbon monoxide [6]. Therefore, if other, less pure fuel is used, fuel processing to remove undesirable substances is required.
Furthermore, the low-temperature system requires some additional units for high-temperature processes, such as the fuel reforming process, or heat exchangers for their reactants. These systems, however efficient, are an extra weight on the aircraft [9]. Another undesirable situation that comes with low temperatures is the slow rate of oxygen reduction half-reaction that is more than 100 times slower than the hydrogen oxidation half-reaction [9].
The hydrogen oxidation half-reaction:

$$H_2 \rightarrow 2H^+ + 2e^- \quad (2.1)$$

The oxygen reduction half-reaction:

$$O_2 + 4H^+ + 4e^- \rightarrow 2H_2O \quad (2.2)$$

On the other hand, low operating temperatures result in short start-up times. Also, PEMFCs have higher power densities than any other type of fuel cell and, has mentioned earlier, is an advantage in the aeronautical industry due to its relation to lower stack weight [8].
Figure 2.12 demonstrates the configuration inside of Boeing Phantom Works, the first two-seater manned by a combination of a LT-PEMFC and a Li-Ion battery powering an aircraft. The maximum power reached

Figure 2.12: Boeing Phantom Works [28].

by the fuel cell was 24 kW, making the aircraft to reach an altitude of 1000 meters [28].

HT-PEMFC

The HT-PEMFC operates at temperatures of 120-200°C. The higher operating temperatures increase reaction rates, prevent water management issues and provide a higher tolerance to poisons. The last point refers to CO poisoning and the fact that there is no longer the need to depend on hydrogen and instead, hydrocarbons or other low purity gases can serve as fuel, which is easier to produce onboard an aircraft.

Acid-doped polybenzimidazoles (PBI) membranes are likely the best candidate to an electrolyte for HT-PEMFCs, due to excellent thermal stability, low gas permeability and good proton transport above 150 °C even at low humidification conditions. Essentially, PBI-based membranes exhibit high proton conductivity when doped with strong acids such as phosphoric acid (H_3PO_4) [41].

HT-PEMFC APU minimizes catalyst poisoning by reformed fuels and simplifies the fuel reformer's components. Thus, fuel processor can be simplified. Temperatures above 180℃ would have an adverse effect on the durability of the component and degradation of the membrane. A cooling system can be used to keep the temperature within the desired temperature range [8]. The Antares DLR-H2 platform is a high-tech motor glider aircraft developed by DLR[1] in collaboration with Lange Aviation[2], presented in Figure 2.13. Using a HT-PEMFC, Antares is the world's first piloted aircraft capable of taking off using only power from fuel cells [42, 43].

Described as a "flying test laboratory" Antares DLR-H2 main purpose is not to study the fuel cell as the main power source of an aircraft but to serve as reliable source research under real operational conditions for future application in commercial aviation as an auxiliary power unit. A test on an Airbus A320 wide-body Advanced Technology Research Aircraft (ATRA) with a fuel cell-powered electric nose wheel showed an emission reduction up to 19% during ground operations [42].

This type of platforms are essential to demonstrate experimentally the use of fuel cells and to evaluate possible heat recovering and water production. This way the fuel cell APU can be tested and optimized at low cost.

Note that these fuel cells still belong to the overall class of low-temperature fuel cells, in contrast to the high-temperature fuel cells as SOFC that operates at temperatures above 600°C, as referred to in the section that now follows.

[1]The German Aerospace Center (DLR) is the national aeronautics, space, transportation, and energy research center and the official space agency of the Federal Republic of Germany.

[2]Lange Aviation GmbH is a German company that manufactures gliders and develops electric power-plants for other aircraft.

Figure 2.13: Antares DLR-H2 platform [42]

2.3.6.2 Solid Oxide Fuel Cell

Solid oxide fuel cells have an electrolyte that is a solid, non-porous metal oxide, usually yttria-stabilized zirconia (Y_2O_3-stablilized $ZrO2$). In this case, the electrolyte transports oxygen ions (O^{2-}) instead of hydrogen ions (H^+) [20].
A SOFC has outstanding efficiencies and operates at high temperatures (600-1000 °C), which allows reforming the fuel within the fuel cell [6, 44, 40]. The benefits are the elimination of the external reformer and using a variety of hydrocarbon fuels, which consequently presents a lighter and simpler overall system which is an important aspect when the purpose is to be applied onboard an aircraft. This fuel cell tolerates high amounts of carbon monoxide, in fact, it can even use CO as fuel [45]. A possible design is the combination of the gas turbine and the solid oxide fuel cell as a hybrid system. Literature shows that both systems are more effective in a hybrid configuration than as separate cycles and can achieve efficiencies of 75%, which is much better than any gas turbine technology developed [9, 21].
The benefits of maintaining the gas turbine with the fuel cell are an increase in system efficiency, faster startup time, and improved thermal integration. In return, the fuel cell helps to increase large savings in fuel consumption, operating costs and emissions [6, 46].
In a study based on the Boeing 777 electrical demand, a typical SOFC-GT APU implemented at the tail end of the aircraft is shown in Figure 2.14a. Figure 2.14b presents the scheme for the APU application onboard of the Boeing 777. It is possible to observe the water, fuel and air flows through the different components. Heat recovering related to cell over-potential is feasible for cabin and jet fuel heating. Once there is no longer the need for cabin heating, smaller stacks can be projected. In addition, hot water produced by the stack could also be recovered for use in the lavatory or for human consumption, after proper treatment. Hence, the aircraft would no longer need to carry fresh water for onboard utilization [10]. There is a prospective study on fuel cells for the aviation/aerospace field, especially in the context of reducing emissions and reducing fuel consumption.

2.3.6.3 Direct Ethanol Polymer Fuel Cell

Direct ethanol polymer fuel cell (DEPFC) is a relatively recent fuel cell, operating in a temperature range of 75-90ºC. Similarly to PEMFC, uses a polymer membrane as an electrolyte.
The use of hydrogen faces some difficulties for onboard transportation, such as safety and weight requirements. DEPFC may overcome these difficulties since ethanol is directly introduced into the fuel cell

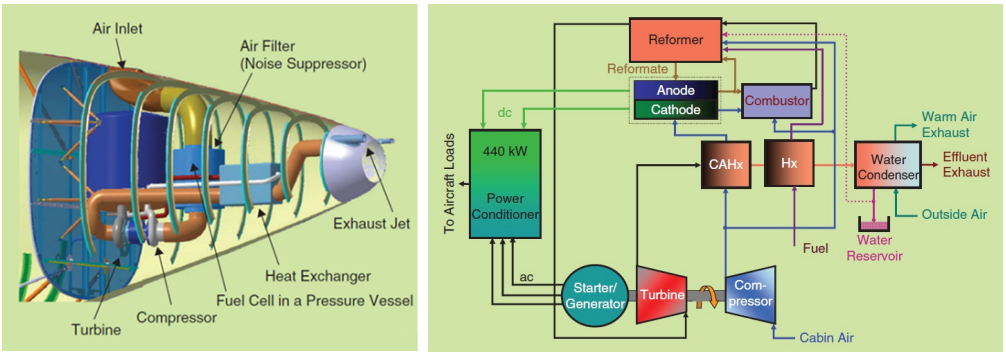

(a) SOFC-GT APU packaging concept. (b) Basic schematic of a fuel cell for APU application.

Figure 2.14: SOFC-GT APU implemented at the tail end of an aircraft [21].

without requiring previous fuel processing.
Ethanol as fuel has several positive aspects, including low cost, high energy density and can be easily transported and stored.

On the other hand, pure ethanol is directly reduced to water and carbon dioxide within the fuel cell, i.e., it is not zero emission and, instead of pure oxygen, highly humid air must be admitted to the cathode in order to avoid membrane from drying. In this way, cell temperature should not exceed 100 °C at 1 atm.

The polymer membrane should provide a suitable barrier to mix fuel and reagent gases, an important factor contributing to the low efficiency of DEPFC. Another factor that contributes to the low efficiencies is the high amounts of heat produced by the fuel cell. In practice, with some improvements in efficiency and cell voltage, DEPFC APU could become a promising alternative for small airplanes and towards a MEA configuration [9, 10, 39].

2.4 Advantages and Disadvantages of the different types of APU

Table 2.1 presents the most important advantages and disadvantages of the APUs previously mentioned.

Table 2.1: Comparison of the different APUs mentioned in this work.

APU system	Advantages	Disadvantages
Gas Turbine	Proven technology Provides aircraft power on the ground when engines are not operating Provides power to start main engine Operates independent of engines and does not affect engine operations	Some installation may not allow in-flight operation; non-operating APU is dead-weight Ownership costs are higher than those for aircraft engines
Energy Recovery	Provides electrical power from waste heat No fuel burn and no moving parts Operates over the entire aircraft flight envelope	New technology and unproven High cost and low efficiency Further development is needed Power output limited by available waste heat, space, device efficiency, and sustainable temperature
Batteries	Zero emissions, zero noise Reliable Operate efficiently over a wide environmental envelope Require minimal maintenance	Long time to charge Short range capacity Low energy density Risk of fire Low Technology Readiness Levels (TRL)
Air Bottle	Simple design	Very limited use Limited air supply Short range capacity
FPLG	High thermal efficiency Compact Easy to maintain Various power sources can be used	Under development Uncertain reliability Low TRL
Fuel Cell	Very efficient Operates independent of engines and does not affect engine operations Operates over the entire flight envelope	New technology Currently heavy and reliability is uncertain Requires a second fuel source (hydrogen) or a fuel reformer system for the aviation fuel Low TRL

2.5 Considered parameters for aeronautical application

This work introduces the concept of an HT-PEMFC as an APU. Analyzing some parameters for the study of the fuel cell onboard an aircraft allows the creation of a more viable concept.

2.5.1 Fuel and Oxidant supply

Hydrogen is a promising fuel, but there are some concerns about its production, storage, and distribution aboard an aircraft. Improving these aspects would lead to better use of hydrogen. Figure 2.15 analyses the system efficiency based on the methods for fuel supply and combined with the possible ways of oxidant supplying. This study was made for cruise conditions in a steady-state simulation.

One way to store hydrogen in an aircraft is in pressurized tanks which require large high-pressure vessels. Also, when at a temperature of -253 °C hydrogen can be stored in a liquid state, i.e., cryogenic hydrogen storage. Despite presenting high energetic power is a complex and expensive process.

Another option is as a dissolved gas in a metal hydride storage system, which is the safest method and is very volumetrically efficient. Although, hydrogen presents low mass energy densities.

Providentially, pure hydrogen is not the only option to run fuel cells. It can be supplied by reformation of various fuels to generate hydrogen, including natural gas, aviation jet fuel, hydrocarbons, among others [8].

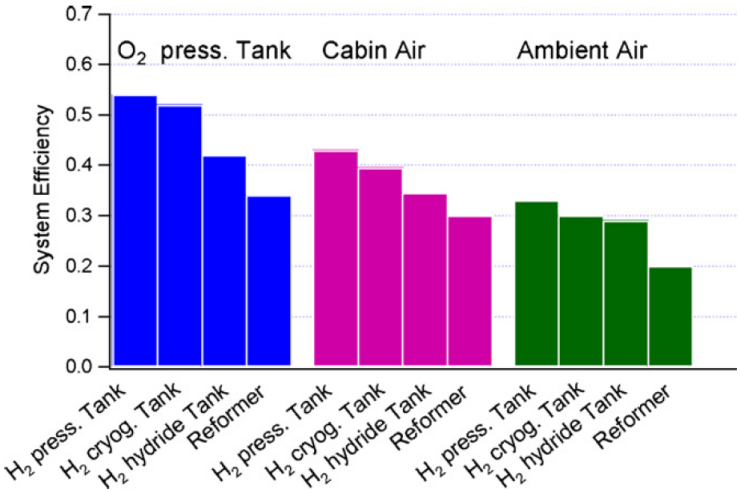

Figure 2.15: Evaluation of system efficiency for various hydrogen supply and oxidant supply concepts under cruise operation conditions [43].

In the framework of this study, it is better to supply oxygen from ambient air, or even better cabin air than carrying an oxidizer onboard which would lead to a significant increase in aircraft weight [6].
From here, the most promising architectures for APU application is the integration of pressurized hydrogen storage and supplying the air from the cabin as it presents the best combination between complexity and efficiency and displays the highest potential for long-range applicability in aircraft structures [43, 6]. Meanwhile, the systems with fuel reforming present the lower efficiency and a more complex system.

Table 2.2: Hydrogen production costs in euros of 1990 [22].

Type of energy	Cost of H2 production (1990 € per kWh)
Biomass	448
Coal	453
Electricity	439
Natural Gas	219
Oil based	439
Solar	2549

Analyzing Table 2.2, we can assert that the cheapest method to produce hydrogen is from natural gas, while the most expensive process is from solar energy.
After analyzing the cost of hydrogen production per kWh, it is fundamental to interpret the fine compositions of the reformed fuel as they directly relate to the performance of a fuel cell system. Therefore, Table 2.3 exhibits the composition of hydrogen (H_2), carbon dioxide (CO_2), water vapor (H_2O) and nitrogen (N_2) of several fuels after exposed to steam reforming. Steam reforming tests to different fuels show that methane steam reforming produces a higher volume percentage of hydrogen.

2.5.2 Altitude Sensitivity

Considering fuel cells depending on ambient air, then APUs are limited at very high altitudes due to difficulties associated with reduced air density [48]. As the altitude increases, the ambient air pressure decreases, as well as the stoichiometric factor of the air and the partial pressure of the oxygen.
Altitude tests present notable performance loss at $0.7\mathrm{bar}/2200\mathrm{m}$ altitude [7, 49, 50]. Above that altitude,

Table 2.3: Volume percentage composition of products from different processes for producing hydrogen-rich feed for fuel cells [47].

Steam-reforming of	Composition of resulting fuel (vol%)			
	H_2	CO_2	H_2O	N_2
Methane	64.1	16.3	17.8	1.8
Methanol	61.8	21.1	14.1	3.0
Ethanol	62.6	21.4	12.5	3.5
Gasoline, diesel fuel, and jet fuel	58.2	19.7	20.6	1.5

the voltage response of the fuel cell decreases as the cathode oxygen partial pressure also decreases leading to a performance decline [7]. The drying of the membrane due to cathode air pressure decline seems to cause the problem as it lowers the voltage of the cell and therefore the maximum operable current. This current drastically affects the power and efficiency of the fuel cell [41].

Several studies suggest that fuel cell systems should operate with high air stoichiometries (often $\lambda_c \simeq 2.5$ is used for altitudes higher than $2000\mathrm{m}$), as it lowers the power loss of the fuel cell due to prevent any cathode concentration depletion [7, 51]. Literature also reveals that there is a fuel efficiency increase of 5% in obtaining air from cabin other than ambient air at high altitude conditions [6, 52]. The reason for that is that using cabin air allows reducing the effects of varying atmospheric pressure.

2.6 Energy and Exergy Analysis

Data obtained from energy and exergy analysis of a system allows respectively, to measure the energy conversion, and to locate, identify and quantify the magnitude of waste and losses for the optimization of a thermal system. Thermodynamics is the science that studies systems and how they interact with their surroundings, governed by the two laws of thermodynamics.
The first law of thermodynamics states that energy cannot be created or destroyed, it can only be transformed from one form to another. Hence, the total amount of energy remains the same within a system, for that reason the first law is generally called as the principle of conservation of energy.
The Second Law of Thermodynamics asserts that energy has quality as well as quantity, and actual processes occur in the direction of decreasing quality of energy. The quantification of energy quality, or the potential to perform work, according to the Second Law, cames from the definition of exergy and entropy properties. Contrary to energy, exergy is consumed in all the actual processes, as entropy is produced. Entropy is never destroyed, is always created in real processes.
Exergy represents the maximum amount of useful work obtained while two systems interact to equilibrium. The second system is a reference system, generally considered the environment. Exergy depends on the system and the reference environment which is arbitrary. When a system and the environment are at equilibrium the opportunities to perform work cease to exist, this is called the dead state. At the dead state, exergy is null because it is no longer possible to make changes between the two systems or any interaction [18].
Energy and exergy analysis are complementary. While the energy balance allows a quantitative interpretation of the energy involved, the exergy balance provides qualitative information of that energy, pointing out the critical points of the system due to its irreversibilities and losses. This information can be used for designing, evaluating, optimizing and improving energy systems.
Efficiency based on First Law focuses its attention on reducing losses by treating all forms of energy as equal, whether mechanical or thermal energy. Exergy efficiency is generally lower than energy efficiency,

due to the presence of process irreversibilities, which destroy part of the initial exergy. Nevertheless, the exergetic efficiency provides a more accurate understanding of system performance.
Fuel cells are not heat engines yet produce heat that must be removed. Depending on the size of the system, the temperature of the available heat and the requirements of its application this thermal energy can be either rejected, used to produce steam or hot water, or converted to electricity via a gas turbine or steam bottoming cycle or some combination of this [40]. One way to increase the system efficiency is by one of the methods of heat recovering described above. The use of the water produced or the highly efficient heat recovery must be planned as part of the basic engineering structure.

2.6.1 Thermodynamic Balances

In thermodynamics, an abstract fixed region can be applied to a system to solve conservation principles. The fixed region studies the masses and different forms of energy crossing a defined boundary (control surface) of the region and is known as control volume [18].
The general balance equation for any quantity in a system can be written as

$$Input + Generation - Output - Consumption = Accumulation\,Variation \quad (2.3)$$

From this equation, we can write the mass, energy, entropy, and exergy balances. Furthermore, the first and second law efficiency are also defined from balance equations.

2.6.1.1 Mass Balance

For steady state and steady flow conditions the total mass flow rate entering the control volume remains unchanging in time. Thus, the inlet mass flow rate ($\dot{m}_{in}$) is equal to the outlet mass flow rate ($\dot{m}_{out}$). In these conditions, the principle of mass conservation, on rate form, can be defined by Eq. 2.4.

$$\sum \dot{m}_{in} = \sum \dot{m}_{out} \quad (2.4)$$

where all incoming and outgoing streams are considered.

2.6.1.2 Energy Balance

For a control volume at steady state, the total amount of energy present at any instant remains constant, i.e., the total energy rate going in ($\dot{E_{in}}$) and out ($\dot{E_{out}}$) across the boundary are equal as can be seen in Eq. 2.5.

$$\sum \dot{E}_{in} = \sum \dot{E}_{out} \quad (2.5)$$

The conservation of energy in a control volume, assuming steady-state flow and neglecting potential and kinetic differences, can be expressed by Eq. 2.6.

$$\dot{Q}_{cv} - \dot{W}_{cv} + \sum \dot{m}_{in}\bar{h}_{in} - \sum \dot{m}_{out}\bar{h}_{out} = 0 \quad (2.6)$$

where $\bar{h}$ represents the specific enthalpy, $\dot{Q}_{cv}$ and $\dot{W}_{cv}$ are the energy rates transfer by heat and by work, respectively, across the control surface. The work rate is considered positive when produced by the system, in other words, whenever it is transferred from the system to the surroundings.

2.6.1.3 Entropy Balance

Unlike energy that is conserved, entropy is generated as a result of process irreversibilities. These irreversibilities result in an increase over the control volume, so the output entropy exceeds the input entropy. From the second law of thermodynamics, and assuming steady-state conditions, entropy balance can be defined, inside the control volume, as follows.

$$\sum \dot{m}_{in}\bar{s}_{in} - \sum \dot{m}_{out}\bar{s}_{out} + \sum \frac{\dot{Q}_{cv}}{T_{cv}} + \dot{S}_{gen} = 0 \quad (2.7)$$

where $\bar{s}$ stands for specific entropy, $\dot{S}_{gen}$ is the rate of entropy generation, and T_{cv} is the temperature of the control surface, considered uniform, through which heat is transferred. Entropy can be transferred as mass (first and second portion of the equation) and as heat (third portion). Note that the entropy transferred through work is null.

2.6.1.4 Exergy Balance

The different forms of exergies are physical exergy (ex_{ph}), chemical exergy (ex_{ch}), kinetic exergy (ex_{kin}) and potential exergy (ex_{pot}), and the total exergy is the sum of all these forms of exergy as presented in Eq. 2.8.

$$ex = ex_{ph} + ex_{ch} + ex_{kin} + ex_{pot} \quad (2.8)$$

Exergy balance comes from combining the first and second law of thermodynamics. During steady-state conditions, the exergy balance equation can be defined as follows:

$$\dot{E}x_{dest} = \sum \left(1 - \frac{T_0}{T}\right)\dot{Q} + \sum \dot{m}_{in}\dot{e}x_{in} - \sum \dot{m}_{out}\dot{e}x_{out} + \dot{E}x_w \quad (2.9)$$

where $\dot{E}x_{dest}$ is the rate of exergy destruction, $\dot{E}x_w$ is the exergy of work and T_0 is the temperature at reference conditions.

2.6.2 System Efficiency

2.6.2.1 Energy and Exergy

The energy efficiency (η) and exergy efficiency (ψ) for a combined system can be determined from Eq. 2.10 and 2.11. According to the first law of thermodynamics, the energy efficiency of a system is defined by the ratio of outcome power and the power supplied to the system as follows:

$$\eta = \frac{\sum \dot{E}_{out}}{\sum \dot{E}_{in}} \quad (2.10)$$

The second law of thermodynamics defines the exergy efficiency or rational efficiency, which measures how close a system is to its maximum efficiency, as demonstrated in Eq. 2.11.

$$\psi = \frac{\sum \dot{E}x_{out}}{\sum \dot{E}x_{in}} = 1 - \frac{\sum \dot{E}x_{dest}}{\sum \dot{E}x_{in}} \quad (2.11)$$

The exergy destruction quotient (γ_{dest}) compares the component destruction rate with the rate of global destruction of the entire system as demonstrated in Eq. 2.12.

$$\gamma_{dest} = \frac{\dot{E}x_{dest}}{\dot{E}x_{dest,total}} \quad (2.12)$$

This parameter can provide relevant information about the thermodynamic inefficiencies of a process.

2.6.3 Efficiency of Fuel Cells Applied in Aircraft

Extracted from several papers, Table 2.4 describes the systems and shows the results of energy and exergy efficiency regarding fuel cell APUs and some cases of fuel cell propulsion systems.

Table 2.4: System description, energy and exergy efficiency of fuel cells used as an APU/propulsion application.

Paper	Description	Efficiency	Exergy
Enrico and Toro [46]	Modeling and simulation of a hybrid SOFC-GT APU using liquid fuel (jet-A fuel) and a power output of 250 kW.	n.d.	58.7%
Freeh et al [52]	Simulation of an off-design SOFC-GT APU providing 400kW of power. The study was made for sea level, cruise and part power cruise (250 kW).	42.4% 72.6% 72.8%	n.d.
Rajashekara et al [21]	Modeled a 440 kW SOFC-GT hybrid system APU sized with estimated mass over 880 kg. System performances were calculated at sea level and altitude conditions.	60.6% 73.7%	n.d.
Bavarsad [44]	Solid oxide fuel cell gas turbine hybrid APU powered by natural gas.	65.6%	59%
Choudhary and Krishna [53]	Integration of a SOFC with a turboprop engine for propulsion system.	64.7%	n.d.
Genç and Sarikoç [54]	Substitution of a combustion chamber by a SOFC-GT, resulting in a hybrid power system with heat recovery for an aeronautical vehicle propulsion.	62.1%	54.9%
Ramsdorf and Matelli [10]	DEPFC APU system with a power demand of 82.5 kW and performing on-board waste heat recovery for cabin heating and jet fuel heating.	n.d.	46.2%
Kallo [55]	Antares DLR H2 -Gen 2 can power up to 33 kW, hybrid up to 55 kW	52%	n.d.
Fakehi et al [56]	A hybrid wind-hydrogen system using a 224 kW LT-PEMFC.	40.2%	47%

n.d. - no data

Chapter 3

Case Study

In the current chapter, the power required for the APU, along with the flight data of the aircraft and the electrical demand of the various systems, is specified. After that, a system based on an HT-PEMFC to replace the conventional gas turbine APU is proposed and important assumptions for its simplification are mentioned. Furthermore, the design of the fuel cell system is explained.
Figure 3.1 presents the flow chart for evaluation of the possibility of replacing the conventional gas turbine APU for a new APU concept.

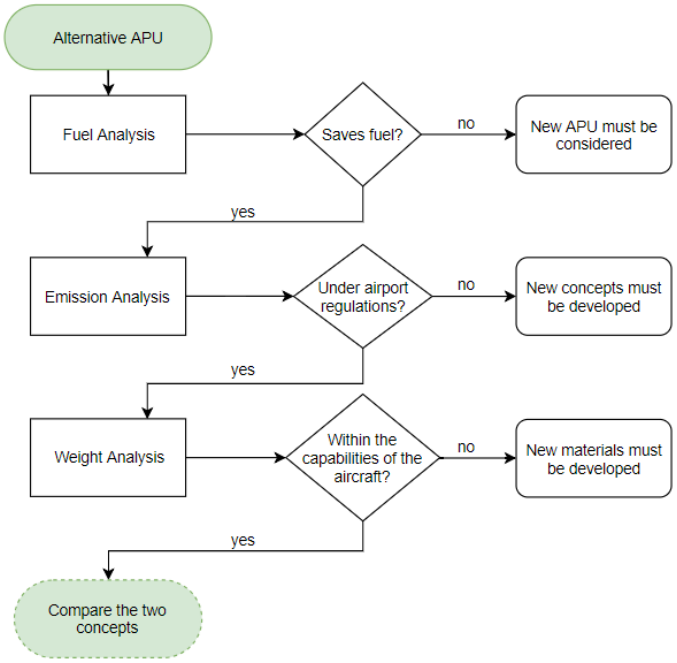

Figure 3.1: Diagram of the alternative APU feasibility evaluation.

3.1 Aircraft and APU considered

For the purpose of this study, it is considered an Airbus A320 and its respective APU, a Honeywell 131-9A (Fig. 3.2), this will be the APU used as reference when calculating the impact on weight, emissions and fuel consumption of the alternative APU.

Equipped with two CFM International CFM56 engines and a Honeywell 131-9A APU the aircraft and APU specifications are presented in Table 3.1.
Aircraft APU provides 115/200 VAC 400 Hz. This turbine provides up to 300 kW when it is at full load (main engines start). In standard conditions the usage of the APU for the aircraft requirements is about 85 kW, through a generator up to 90/120 kVA, using the bleed air for pneumatic purposes. This means that there is enough energy available for other electrical purposes. Figure 3.2 is a diagram demonstrating the

Table 3.1: Airbus A320 [57] and Honeywell 131-9A specifications [58].

System	Parameter	Value	Units
Aircraft (Airbus A320)	MTOW	79,000	kg
	Range	6300	km
	Max Fuel Capacity	26730	L
	Cruise speed	828 (0.78 Ma)	km/h
	L/D	17	
APU (Honeywell 131-9A)	Dry Mass	145	kg
	Shaft Power	447	kW
	Power to Mass Ratio	3.09	kW/kg
	APU Dry Mass/MTOW	0.91	%

electric distribution system for a traditional aircraft, provided from the CFM International CFM56 engines and the Honeywell 131-9A APU (in the middle).

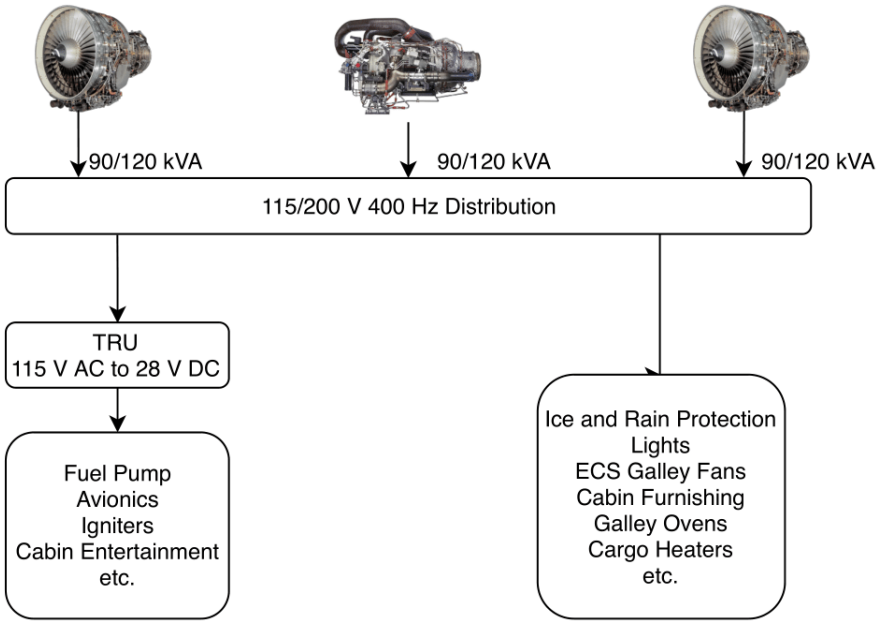

Figure 3.2: Electric distribution systems for traditional aircraft such as A320 and B737.

Figure 3.3 shows the electrical demand expressed as kilo volt-ampere (kVA) for each flight phase in cold day cruise conditions for a traditional aircraft as an A320. <

3.1.1 Weights of APU Integration

In addition to the dry weight of the APU, there are subsystems required for an APU installation, these subsystems should also be considered when analyzing the weight difference between the two APU systems. Annex A.1 shows the estimated mass of all components from the APU system including tubes, ducts, and wires. In the Annex, the negative weights are the ones disregarded for the implementation of the new APU.

3.1.2 Emissions and Fuel Consumption

Table 3.2 is a summary of estimated maximum fuel flow and emissions regarded hydrocarbons (HC), carbon monoxide (CO) and nitrogen oxides (NOx), from Honeywell 131-9A operating at sea level and in

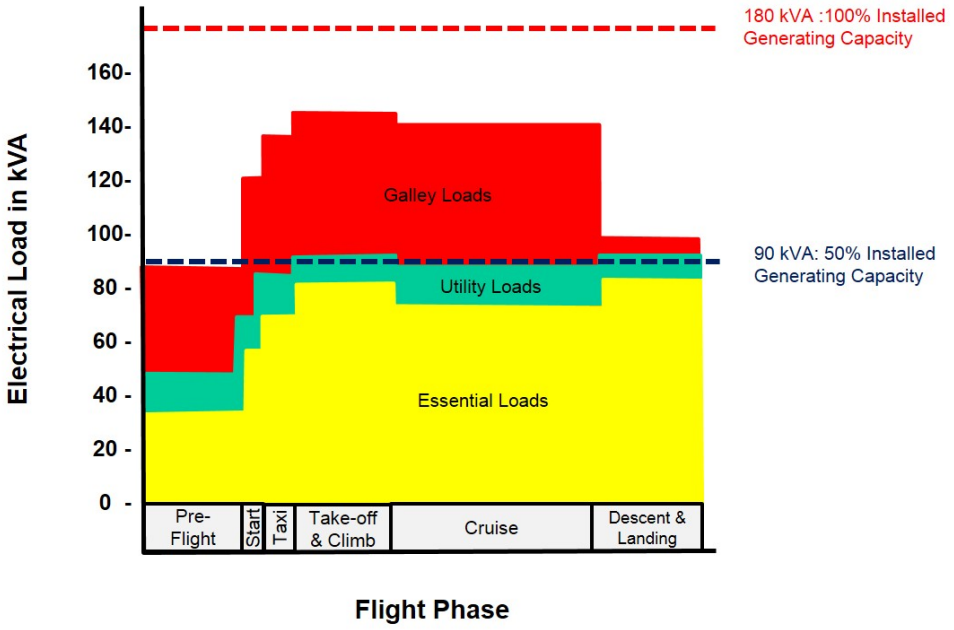

Figure 3.3: Total electrical load on an A320 engine generators during major segments of flight [59].

a standard day.

Table 3.2: APU emissions and fuel consumption [60].

Fuel Flow [kg/h]	HC [g/kg]	CO [g/kg]	NOx [g/kg]
115.5	0.37	4.88	6.64

During cruise conditions, the aircraft fuel consumption is proportional to mass and depends on flight time (or distance). The fuel consumption for a fixed mass (m) to be transported (or saved) is presented in Eq. 3.1 [15].

$$m_f = m\left(e^{t_F \cdot k_E} - 1\right) \quad (3.1)$$

$$k_E = \frac{sfc \cdot g}{L/D} \quad (3.2)$$

Where m_f is the fuel mass to transport the fixed mass m, t_F is the flight time, sfc is the specific fuel consumption, g is the gravitational acceleration and L/D is the lift to drag ratio.

3.2 HT-PEMFC APU System

For this study, it is considered that the APU has to meet the specified power demand and results are compared with the literature (see Table 2.4).
Following the concept of a more electric aircraft, the HT-PEMFC APU is designed to achieve a power demand of 250 kW, which is a lot more than the gas turbine APU can provide. The system fuel is natural gas, requiring some extra components, to be converted into hydrogen. For the cathode side, ambient air is used as an oxidant. The fuel cell is configured to achieve the power goal.

The proposed system displays a combination of power generation and waste heat recovery units. The Fuel Cell, Direct-Current inverter (DC), Gas Turbine, Compressor, Water Gas Shifting, Steam Reformer, and Pump units are used in power generation. Meanwhile, Heat Exchangers, Combustor and Heat Recovering Steam Generator (HRSG) are implemented to perform heat management in order to attain a better efficiency of the system.
The simplified system layout is illustrated in Figure 3.4. In this system are presented five different flows: fuel, air, water, exhaust gases, and the cathode-off gases which correspond to the water vapor produced by the fuel cell and the amount of unused air.

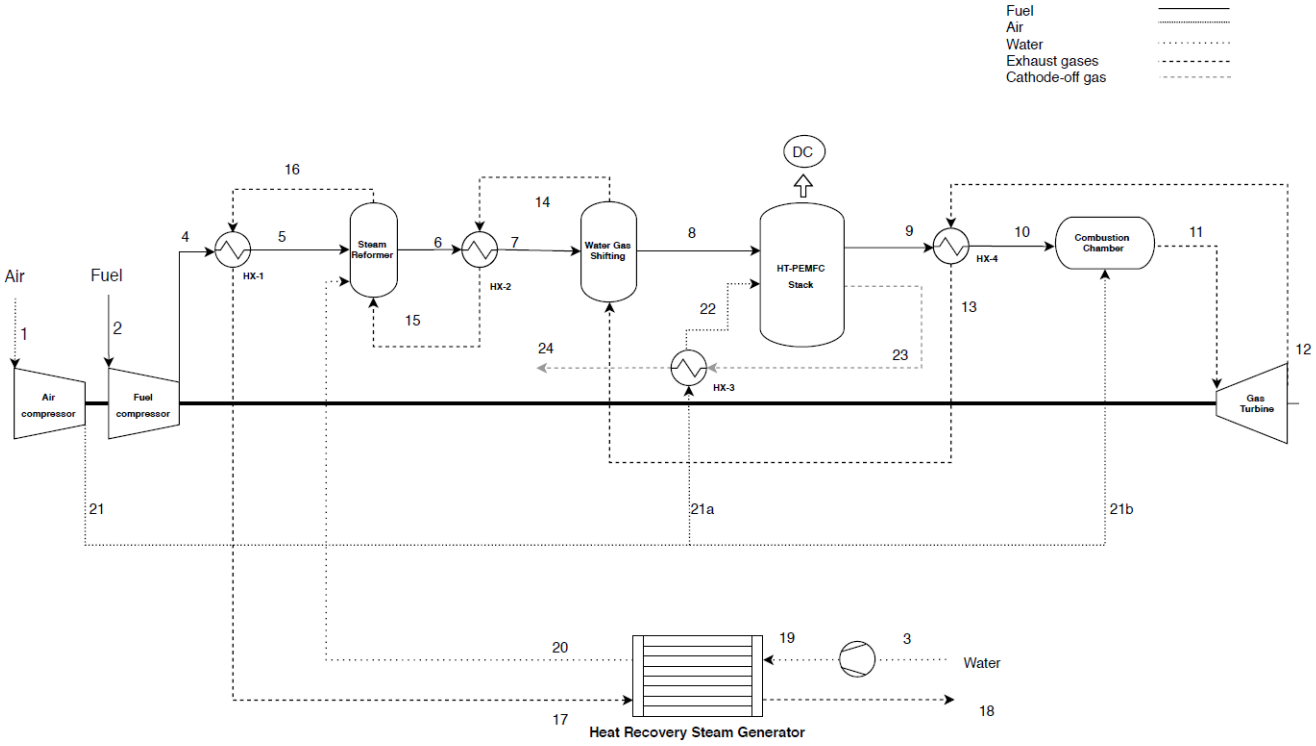

Figure 3.4: Proposed scheme for system layout

3.2.1 Assumptions, Limitations and Delimitations

For this study it is important to understand the system limitations in order to interpret the results. The fuel cell mathematical model assumptions are presented separately from the overall system for a clear understanding. These parameters intend to simplify the model and are listed below.

Fuel Cell:

- Single phase operation
- Isothermal operation
- No reactant crossover in the electrolyte
- The concentration polarization loss is neglected
- Catalyst layer is treated as interface
- Fully developed laminar flow is considered

- The porous electrodes, catalyst layers and membrane are isotropic and homogeneous
- Sulfur effects are neglected

Overall System:

- All gases are considered as ideal gases
- The reference conditions of temperature and pressure are T_0 = 298.15 K and P_0 = 101.325 kPa, respectively
- The mole fractions of atmospheric air components are: y_{O_2} = 0.2054; y_{H_2O} = 0.0217; y_{N_2} = 0.77253; y_{CO_2} = 0.000337 [1]
- All units operate under a steady state condition
- The efficiencies of air compressor, fuel compressor, water pump, gas turbine, heat exchanger, combustor and DC/DC converter are 85%, 85%, 85%, 85%, 95%, 98% and 94%, respectively.
- A fuel utilization ratio of 95%
- Cathode stoichiometric ratio of 2.5
- Kinetic and potential exergies are neglected
- Natural gas contains only methane (CH_4)
- The pressure losses are 2% for each device used in the system

3.2.2 System Configuration

Air enters the air compressor (1) before being supplied to the fuel cell and the combustor chamber. The air compressor is responsible for pressurizing the system on the ground where the pressure difference is constant and is turned off during the cruise phase. During the cruise phase, cabin air is used instead of ambient air, so the air compressor is no longer necessary.
Fuel is also pressurized (2-4), but in this case, compression is required during all the flight envelope. When gas flows through a gas line it loses pressure due to the frictional resistance of the parts exposed to the gas. This pressure drop cannot be countered, so the fuel is pressurized to respond to those losses and to achieve the stack pressure.
Methane is reformed in a steam reformer (5-6) and a water gas shifting (7-8). The steam reformer converts methane into hydrogen and some carbon monoxide, and the water shifting reduces the concentration of carbon monoxide in the fuel. This way, a hydrogen-rich gas is fed to the fuel cell (8) to produce the electrical load required for the aircraft. Direct-Current power and heat are generated as the result of the electrochemical processes in the fuel cell. A DC/DC converter converts the variable low-DC voltage output to usable DC power when required. Part of compressed air (21b) and unused fuel (10) from the anode are burned in the combustor to produce the required heat for the turbine to produce work. The turbine is responsible for providing the essential power to run both compressors and to produce the amount of expand the gases that transport the heat required for heat management.
Heat management in the integrated systems is carried out by heat exchangers (HXs) combined with the exhaust gases from the combustor chamber. The heat from product streams of the reformer and the energy from anode and cathode off-gases are recovered by heat exchangers and the combustor chamber.

[1] for this work the small percentage of Argon is considered as N_2.

The recovered heat is used to preheat the fuel (at HX-1 and HX-4) and air (at HX-3), to lower the temperature of the fuel from reformer to the shifting operating temperature (at HX-2), and to vaporize water for the methane steam reformer whereas retain the temperature of reformer at isothermal operation (at HRSG).
To supply vapor water to the fuel processor, fresh water must be pressurized by a pump (3-19) to the required steam pressure for the HRSG. Gas flow from the recuperator has quality heat that can be utilized to generate saturated steam in the HRSG. The HRSG involves an economizer and an evaporator. The pressurized water is heated by the gas flow to the saturation temperature, T_d, in the economizer. Afterwards, the flow enters the evaporator part where saturated steam is generated. Fig. 3.5 shows the flow arrangement for the HRSG. The steam flow rate is calculated by determining the pinch point temperature, T_p, which is the temperature of gas flow entering the economizer from the evaporator part. The pinch point temperature is generally defined as:

$$T_p = T_d + DT_p \quad (3.3)$$

where DT_p is the minimum temperature difference between the temperature of the gas flow at pinch point and the saturation temperature.

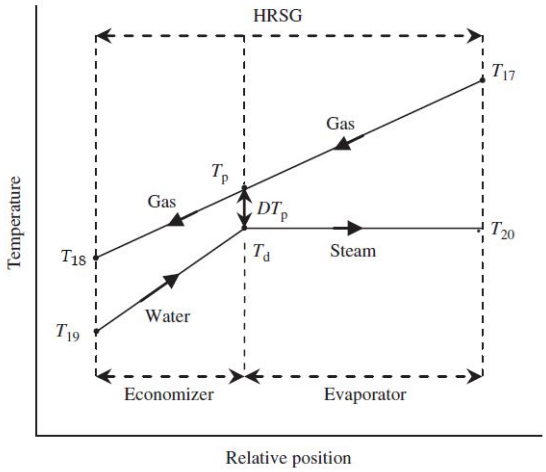

Figure 3.5: HRSG flow arrangement.

Moreover, Table 3.3 summarizes the system describing the flow, temperature, pressure and molar fractions for every known node of the system presented in Fig.4.5. The assumed values are underlined and the values represented with a question mark must be calculated using thermodynamic balances.

3.2.3 Configuration of Stack for Desired Load Condition

While, at sea level, oxygen used in the electrochemical reaction is derived from air and the mass of airflow for the required power ($\dot{W}_{ele}$) is calculated from Eq. 3.4. At cruise conditions the oxygen derives from cabin air. Cabin air as a source of oxygen at high altitudes has proven to allow better efficiency and requires less equipment since there is no need for an extra air compressor [10, 43].
In this work, the oxygen used in the electrochemical reaction is derived from air. The mass of airflow for the required power ($\dot{W}_{ele}$) is calculated according to Eq. 3.4. The hydrogen consumed and the water produced by the fuel cell are described by Eq. **??** and **??**, respectively.

$$\dot{m}_{air} = 3.57 \times 10^{-7} \varphi \frac{\dot{W}_{ele}}{V_{cell}} \quad (3.4)$$

Table 3.3: Description, temperature, pressure and mole fraction of each stream represented in Figure 3.4.

Node	Flow	T [°C]	P [kPa]	Mole fraction							
				y_{CH_4}	y_{CO}	y_{CO_2}	y_{H_2O}(g)	y_{H_2O}(l)	y_{H_2}	y_{O_2}	y_{N_2}
1	Air	$\underline{25}$	$\underline{101.325}$	-	-	0.000337	0.0217	-	-	0.2054	0.77253
2	Fuel	$\underline{25}$	$\underline{101.325}$	1	-	-	-	-	-	-	-
3	Water	$\underline{25}$	$\underline{101.325}$	-	-	-	-	1	-	-	-
4	Fuel	?	?	1	-	-	-	-	-	-	-
5	Fuel	?	?	1	-	-	-	-	-	-	-
6	Reformed Fuel	?	?	?	?	?	?	?	?	?	?
7	Reformed Fuel	?	?	?	?	?	?	?	?	?	?
8	Reformed Fuel	?	?	?	?	?	?	?	?	?	?
9	Anode off-gas	?	?	?	?	?	?	?	?	?	?
10	Anode off-gas	?	?	?	?	?	?	?	?	?	?
11	Exhaust gases	?	?	?	?	?	?	?	?	?	?
12	Exhaust gases	?	?	?	?	?	?	?	?	?	?
13	Exhaust gases	?	?	?	?	?	?	?	?	?	?
14	Exhaust gases	?	?	?	?	?	?	?	?	?	?
15	Exhaust gases	?	?	?	?	?	?	?	?	?	?
16	Exhaust gases	?	?	?	?	?	?	?	?	?	?
17	Exhaust gases	?	?	?	?	?	?	?	?	?	?
18	Exhaust gases	?	?	?	?	?	?	?	?	?	?
19	Water	?	P_{sat}	-	-	-	1	-	-	-	-
20	Water	T_d	P_{sat}	-	-	-	1	-	-	-	-
21	Air	?	?	-	-	0.000337	0.0217	-	-	0.2054	0.77253
21a	Air	?	?	-	-	0.000337	0.0217	-	-	0.2054	0.77253
21b	Air	?	?	-	-	0.000337	0.0217	-	-	0.2054	0.77253
22	Air	?	?	-	-	0.000337	0.0217	-	-	0.2054	0.77253
23	Cathode off-gas	?	?	?	?	?	?	?	?	?	?
24	Cathode off-gas	?	?	?	?	?	?	?	?	?	?

Legend: ? - unknown, $\underline{x}$ - assumed value, T_d - saturation temperature, P_{sat} - saturation pressure

where φ is the stoichiometric air required in cathode reaction, V_{cell} is the cell voltage, F is the Faraday's constant.
To size the stack in order to achieve the desired load condition, unit cells are connected through the bipolar plates to form a stack that supplies direct current in the same way than an APU does. The single cells are connected in series to produce the desired voltage and form modules, those modules are connected in parallel to attain the total power for the system. The fuel cell electrical power output ($\dot{W}_{fc}$) can be calculated from the current density (i) and the cell voltage (V_{cell}) as follows:

$$\dot{W}_{fc} = V_{cell} i A_{cell} N_{cell} \quad (3.5)$$

where A_{cell} is the cell active area and N_{cell} is the number of cells in a module.
With the target operating stack voltage defined, the number of cells in series is given by,

$$N_{cell} = \frac{V_{stack}}{V_{cell}} \quad (3.6)$$

where V_{stack} is the stack voltage.
The operating stack current for required power is given by,

$$I_{stack} = \frac{\dot{W}_{fc}}{V_{cell} N_{cell}} \quad (3.7)$$

Finally, the actual number of cells in parallel for required power is given by

$$N_{mod} = \frac{I_{stack}}{i A_{cell}} = \frac{I_{stack}}{I_{cell}} \quad (3.8)$$

where I_{cell} is the target operating cell current.

Chapter 4

Methodology

This chapter starts with an introduction to the entropy, enthalpy and exergy parameters used in the first and second law of thermodynamics.
Afterward, the two mathematical models used for the HT-PEMFC integrated system are described in detail. The first model concerns the reformer of the natural gas to produce hydrogen to supply to the fuel cell, and water shifting to minimize the carbon monoxide percentage in the reformed fuel, in other words, analyzes the fuel processor system. The second model concerns the fuel cell electrochemical and diffusion model and analysis the actual cell voltage and current density.
In addition, an analysis of the thermodynamic balance of each component and the overall system, using control volumes, is performed.
This chapter finishes with an elaboration diagram of the numerical simulation processes of the MATLAB program created for this study.

4.1 Determination of Thermodynamic Properties

This section intends to demonstrate the enthalpy, entropy and exergy equations of a a stream. To analyze the thermodynamic system and perform its evaluation a MATLAB program was developed. The program respects the equations presented in this section.

4.1.1 Enthalpy and Entropy for Gaseous Currents

The enthalpy and entropy of each stream of the studying system are determined by adding all components involved in the mixture,

$$\bar{h}_i(T_i) = \sum_j X_j \bar{h}_j(T_i) \tag{4.1}$$

$$\bar{s}_i(T_i, P_i) = \sum_j X_j \bar{s}_j(T_i, P_{j,i}) \tag{4.2}$$

where X is the molar fraction of each component j and i represents the stream point. The enthalpy for an ideal gas depends only on the temperature, therefore the terms of $\bar{h}_j$ of each component are evaluated at mixture temperature (T_i). Whereas, entropy depends on the mixture temperature and the component partial pressure ($P_{j,i}$).
Enthalpy and entropy are calculated using the following equations:

$$\bar{h}_j(T_i, P_i) = h_f^0 + \Delta\bar{h} = h_f^0 + [\bar{h}(T_i, P_i) - \bar{h}(T_{ref}, P_{ref})] \tag{4.3}$$

$$\bar{s}_j(T_i, P_{j,i}) = \bar{s}^0(T_i, P_{ref}) - R \ln \frac{P_{j,i}}{P_{ref}} \tag{4.4}$$

$$P_{j,i} = P_i X_{j,i} \tag{4.5}$$

where h_f^0 is the enthalpy of formation, $\Delta\bar{h}$ is the change in specific enthalpy from the temperature of

reference (T_{ref}) to the system temperature T, $\bar{s}$ is the specific entropy at temperature T and pressure P_{ref}, $\bar{R}$ is the universal gas constant.
The values for h_f^0 and $\bar{s}^0$ are constants and can be extracted from thermodynamic tables of ideal gases. $\Delta\bar{h}$ is calculated according to NIST [1] database, that provides the constant values and method to determine the enthalpy and entropy of every substance on a wide range of temperatures. From that point, it is simple to create a program in Matlab able to use the database from NIST and calculate its enthalpy and entropy from Eq. 4.3 and 4.4.

4.1.1.1 Enthalpy and Entropy of Reference

It is still necessary to consider the enthalpy and entropy determination at the reference conditions (T_{ref} and P_{ref}), or dead state, which is demonstrated in Eq. 4.6 and 4.7. Moreover, the calculation for partial pressure $P_{j,i}$ is evidenced by Eq. 4.8.

$$\bar{h}_i^0(T_0) = \sum_j X_j \bar{h}_j(T_0) \tag{4.6}$$

$$\bar{s}_i^0(T_0, P_0) = \sum_j X_j \bar{s}_j(T_0, P_{0_{j,i}}) \tag{4.7}$$

$$P_{0_{j,i}} = P_0 X_j \tag{4.8}$$

where T_0 is the reference temperature and P_0 is the reference pressure.

4.1.2 Physical Exergy and Chemical Exergy

In the purpose of this work kinetic and potential energy effects are regarded as negligible. This can be assumed since they present almost zero influence for the total amount. Hence, Eq. 2.8 results in Eq. 4.9, where the specific physical and chemical exergies are defined by Eq. 4.10 and 4.11, respectively.

$$ex_i = ex_{ph,i} + ex_{ch,i} \tag{4.9}$$

$$ex_{ph,i} = (\bar{h}_i - \bar{h}_i^0) - T_0(\bar{s}_i - \bar{s}_i^0) \tag{4.10}$$

$$ex_{ch,i} = \sum_j X_j ex_{ch,j}^0 + RT_0 \sum_j X_j \ln X_j \tag{4.11}$$

where ex_{ch}^0 is the standard chemical exergy of each component j.

4.1.3 Energy, Entropy and Exergy Rates

The rates considered relative to this work are evaluated for each stream accordingly to the energy flux ($\dot{E}$), entropy flux ($\dot{S}$) and exergy flux ($\dot{E}_x$) by the following equations:

$$\dot{E}_i = \dot{n}_i \bar{h}_i \tag{4.12}$$

$$\dot{S}_i = \dot{n}_i \bar{s}_i \tag{4.13}$$

$$\dot{E}x_i = \dot{n}_i \bar{e}x_i \tag{4.14}$$

[1] The National Institute of Standards and Technology (NIST) is a physical sciences laboratory, and a non-regulatory agency of the United States Department of Commerce. NIST provides convenient access to a variety of physical and chemical property data on well defined chemical species and reactions `http://webbook.nist.gov/chemistry/`.

4.2 HT-PEMFC Integrated System with Onboard Hydrogen Production

4.2.1 Fuel Processor Mathematical Model

The system is supplied with natural gas (methane) that needs to go through a fuel processor before entering the fuel cell. In the fuel processor, methane is converted into the reformate gas via two main reactions: steam reforming (Eq. 4.15) and water gas shifting (Eq. 4.16). Steam reforming is the fundamental reaction to produce hydrogen-rich gas, which is the main component for the HT-PEMFC electrochemical process. Fuel reformed before entering the cell is preferable to the internal reforming since the HT-PEMFC would not withstand the extremely high temperatures (700-1000 ℃) required for an internal reforming [61]. Moreover, since carbon monoxide is poisoning for the HT-PEMFC when in large amounts, and to enhance hydrogen concentration water gas shifting is also required.

The fuel reforming process (Eq. 4.15 and 4.16) converts methane and steam into mostly carbon dioxide and hydrogen with some carbon monoxide also produced. There is also excess water in the reformate stream. In the WGS reactor the CO content should be reduced to an acceptable level of less than 10% [61].

The Steam Reforming reaction is given as:

$$CH_4 + H_2O \rightarrow 3H_2 + CO \quad (4.15)$$

The Water Gas Shifting reaction is given as:

$$CO + H_2O \rightarrow H_2 + CO_2 \quad (4.16)$$

The equilibrium constants of steam reforming and water gas shifting reactions as a function of temperature are represented by Eq. 4.17 and 4.18, respectively [62].

$$K_r = \frac{n_{H_2}^3 n_{CO}}{n_{CH_4} n_{H_2O}} P_{tot}^2 \quad (4.17)$$

$$K_s = \frac{n_{H_2} n_{CO_2}}{n_{CO} n_{H_2O}} \quad (4.18)$$

where n is the number of moles of each component and P_{tot} is the pressure of the flow entering the reformer.

The equilibrium constants and the Gibbs minimization method are correlated as follows:

$$\ln K_{eq}(T) = \frac{-\Delta G(T)}{RT} \quad (4.19)$$

where T is the temperature of each unit and ΔG is the Gibbs free energy.

During reaction proceeding, total Gibbs free energy (G^t) decreases and the equilibrium condition is attained when reaches its minimum value. The Gibbs free energy minimization method is used to estimate composition of the reformate and the flue gas, as demonstrated in Eq. 4.20. To convert the optimization problem to algebraic equations, Lagrange's undetermined method is used, and through an iterative process using the minimization tool in MATLAB, the minimum Gibbs free energy is determined and so are the equilibrium compositions.

$$min(G^t)_{T,P} = min(\sum_i n_i \bar{G}_i) = min\left[\sum_i n_i \left(G_i^0 + RT \ln \frac{\bar{f}_i}{f_i^0}\right)\right] \quad (4.20)$$

Considering the fuel processor required heat, that accounts for preheating the reactants, retaining the reaction temperature of the reformer, and to recover heat from the outlet stream of the reformer, then the required heats of steam reforming and water gas shifting reactions are determined from the difference of products enthalpy and reactants enthalpy as follows:

$$\dot{Q}_r = \dot{n}_{CH_4}(\bar{h}_{CO} + 3\bar{h}_{H_2} - \bar{h}_{H_2O} - \bar{h}_{CH_4}) \quad (4.21)$$
$$\dot{Q}_s = \dot{n}_{CO}(\bar{h}_{CO_2} + \bar{h}_{H_2O} - \bar{h}_{CO} - \bar{h}_{H_2O}) \quad (4.22)$$

where $\dot{Q}_r$ is the heat required for steam reforming and $\dot{Q}_w$ is the heat required for water gas shifting.

$$\dot{Q} = \begin{Bmatrix} \dot{Q} & if & \dot{Q} > 0 \\ 0 & if & \dot{Q} \leqslant 0 \end{Bmatrix} \quad (4.23)$$

Thus, the fuel processor heat is

$$\dot{Q}_{fp} = \dot{Q}_r \quad (4.24)$$

where Q_{fp} is the heat of fuel processor obtained from the surroundings. Is equal to zero if the reaction is exothermic or adiabatic.
Moreover, the fuel processor efficiency is the ratio of lower heating value of hydrogen (LHV_{H_2}) produced and the total energy used for fuel process as presented by Eq. 4.25.

$$\eta_{fp} = \frac{LHV_{H_2}\dot{n}_{H_2}}{LHV_{fuel}\dot{n}_{fuel} + \dot{Q}_{fp}} \quad (4.25)$$

where $\dot{n}_{fuel}$ is the molar flow rate of the fuel.

4.2.2 Fuel Cell Mathematical Model

The mathematical model of the fuel cell under study uses diffusion and electrochemical models. To calculate the concentration at catalyst surface is used Stefan Maxwell equation and the Fick's law and to determine the voltage and current density is used the electrochemical model. For this work it is assumed single-phase, steady state, isothermal operation, one-dimensional electrochemical model. The mathematical model developed in this study is based on a planar design in which its geometric and material related data are reported from literature and presented in Table 5.1.
The fuel cell consist of two diffusion layers, anode and cathode catalyst layers, and the membrane as presented in Figure 4.1. A PBI doped phosphoric acid (PA) membrane is used as electrolyte.

4.2.2.1 Gas Transport in Porous Media

This model considers only one-dimensional diffusion in z direction. Diffusion of multicomponent gas flows through the gas diffusion layer (GDL) can be described using the Stefan-Maxwell equation as shown in Eq. 4.26.

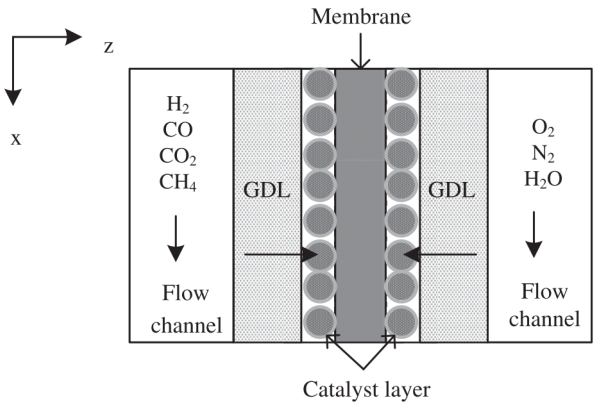

Figure 4.1: Schematic diagram of a HT-PEMFC and the catalyst layer using the thin electrolyte film assumption [61].

$$\frac{\partial X_i}{\partial z} = \frac{RT}{p} \sum_j \frac{X_i \dot{n}_i - X_j \dot{n}_j}{D_{ij}^{eff}} \quad (4.26)$$

X_i is the mole fraction of species i, $\dot{n}_i$ is the mole flux of species i, and D_{ij}^{eff} is the effective binary diffusion coefficient for the i-j pair in the porous medium. D_{ij}^{eff} can be calculated using the corrected Slattery Bird correlation [63] to account for the porosity and tortuosity effects with the Bruggeman correlation [64].

$$D_{ij}^{eff} = \frac{a}{P} \left(\frac{T}{\sqrt{T_{c,i} T_{c,j}}} \right)^b (P_{c,i} P_{c,j})^{1/3} (T_{c,i} T_{c,j})^{5/12} \left(\frac{1}{M_i} + \frac{1}{M_j} \right)^{1/2} \varepsilon^\tau \quad (4.27)$$

where T_c and P_c are the gas critical temperature and pressure, respectively. M is the gas molecular weight, ε is the porosity and τ is the tortuosity. a and b are constants, (a = 0.0002745 and b = 1.832) for diatomic gases.

4.2.2.2 Diffusion in the Porous Cathode

The chemical species in the cathode are O_2, N_2 and H_2O. The species mole flux can be given as follows:

$$\dot{n}_{O_2} = \frac{i}{4F} \quad (4.28)$$

$$\dot{n}_{N_2} = 0 \quad (4.29)$$

$$\dot{n}_{H_2O} = \frac{-i}{2F} \quad (4.30)$$

where i is the current density per geometric electrode area and F is the Faraday's constant.
Substituting the species flux in Eq. 4.26, we have:

$$X_{N_2} = X_{N_2}^0 exp \left(\frac{R \cdot T_{fc} \dot{n}_{O_2} t_{GDL}}{P_{ca} D_{N_2,O_2}^{eff}} \right) \quad (4.31)$$

$$X_{H_2O} = X^0_{H_2O} exp\left(\frac{R\,T_{fc}\dot{n}_{O_2}t_{GDL}}{P_{ca}D^{eff}_{H_2O,O_2}}\right) \quad (4.32)$$

$$X_{O_2} = 1 - (X_{N_2} + X_{H_2O}) \quad (4.33)$$

the subscripts an and ca represent the anode and cathode, respectively. t_{GDL} is the gas diffusion layer thickness, D^{eff} is the effective binary diffusion coefficient, P is the pressure, X^0 is the molar fraction of specie before the reaction occurs.

4.2.2.3 Diffusion in the Porous Anode

The reformate gas in the anode consists of a gas mixture of H_2, CO, CO_2, CH_4, and H_2O. The mole flux of the gases can be given as follows:

$$\dot{n}_{H_2} = \frac{i}{2F} \quad (4.34)$$

$$\dot{n}_{CO} = 0 \quad (4.35)$$

$$\dot{n}_{CO_2} = 0 \quad (4.36)$$

$$\dot{n}_{CH_4} = 0 \quad (4.37)$$

$$\dot{n}_{H_2O} = 0 \quad (4.38)$$

Substituting mole flux of the gases in Eq. 4.26, we derive:

$$X_{CO} = X^0_{CO} exp\left(\frac{RT_{fc}\dot{n}_{CO}t_{GDL}}{P_{an}D^{eff}_{CO,H_2}}\right) \quad (4.39)$$

$$X_{CO_2} = X^0_{CO_2} exp\left(\frac{RT_{fc}\dot{n}_{CO_2}t_{GDL}}{P_{an}D^{eff}_{CO_2,H_2}}\right) \quad (4.40)$$

$$X_{CH_4} = X^0_{CH_4} exp\left(\frac{RT_{fc}\dot{n}_{CH_4}t_{GDL}}{P_{an}D^{eff}_{CH_4,H_2}}\right) \quad (4.41)$$

$$X_{H_2O} = X^0_{H_2O} exp\left(\frac{RT_{fc}\dot{n}_{H_2}t_{GDL}}{P_{an}D^{eff}_{H_2O,H_2}}\right) \quad (4.42)$$

$$X_{H_2} = 1 - (X_{CO} + X_{CO_2} + X_{CH_4} + X_{H_2O}) \quad (4.43)$$

4.2.2.4 Thin Electrolyte Film Model

The PBI doped PA membrane is used as an electrolyte in this model. PA provides paths for proton conductivity in catalyst layer and PBI membrane. The concentrations of H_2 and O_2 vary along the thin electrolyte films of anode and cathode. Oxygen and hydrogen concentration at the catalyst interface is extracted from Fick's law for diffusion as presented in Eq. 4.44 and 4.45, respectively.

$$\frac{N_{O_2}}{S_{Pt,ca}} = \frac{-D_{O_2}^{PA}(C_{O_2,Pt} - C_{O_2,dissolve})}{\delta_{ca}} \quad (4.44)$$

$$\frac{N_{H_2}}{S_{Pt,an}} = \frac{-D_{H_2}^{PA}(C_{H_2,Pt} - C_{H_2,dissolve})}{\delta_{an}} \quad (4.45)$$

S_{Pt} is the real surface area of Platinum (Pt) per geometric electrode area, D^{PA} is the diffusivity through the ionomer, and δ is the avarage film thickness. $C_{dissolve}$ is the equilibrium concentration in the acid film and can be found by the Henry's Law, as shown in Eq. 4.46 and 4.47.

$$C_{O_2,dissolve} = PX_{O_2}H_{O_2} \quad (4.46)$$
$$C_{H_2,dissolve} = PX_{H_2}H_{H_2} \quad (4.47)$$

where P is the pressure, X is the molar fraction and H is the Henry's constant (or solubility) in function of temperature and acid weight concentrations (ω) is defined as follows [65]:

$$H_{O_2} = 10^{-1}\exp(257.13\omega^2 - 431.08\omega + 178.45) + \frac{-93500\omega^2 + 156646\omega - 64288}{T_{fc}} \quad (4.48)$$

The oxygen diffusivity through the ionomer is given by

$$D_{O_2}^{PA} = A\exp\left(\frac{-E_a}{RT}\right) \quad (4.49)$$

where A is the pre-exponential factor and E_a is the diffusion activation energy given by Eq. 4.51 and 4.50, respectively. Both E_a and A depend on the acid weight concentration (ω) as demonstrated in the following equations [65].

$$Ea = -0.011607142857\,\omega^2 + 1.9642142857\,\omega - 75.376 \quad (4.50)$$

$$A = 0.0000025\ \exp(1.76593\,\omega) \quad (4.51)$$

Due to the lack of data on hydrogen solubility in phosphoric acid at high temperatures, hydrogen solubility can be considered a similar behavior as in water systems, we can correlate with the oxygen solubility as

[66]

$$H_{H_2} = 4H_{O_2} \quad (4.52)$$

Similarly, for the hydrogen diffusion coefficient in phosphoric acid electrolyte we can write [66]

$$D_{H_2}^{PA} = 4D_{O_2}^{PA} \quad (4.53)$$

4.2.2.5 Electrochemical Model

The overall electrochemical reaction in a HT-PEMFC can be described as,

$$H_2(g) + \frac{1}{2}O_2(g) \rightarrow H_2O(g) \quad (4.54)$$

At operating conditions, the maximum theoretical potential achieved by a fuel cell is the reversible potential (E_{rev}) that can be described by the Nernest equation (Eq. 4.55).

$$E_{rev}(T,P) = E^0 + \frac{RT}{zF}\ln\left[\frac{(RT)^{1.5}C_{H_2-PT}{C_{O_2-PT}}^{0.5}}{a_{H_2O}}\right] \quad (4.55)$$

where z is the number of electrons transferred for each molecule of fuel, R is the universal gas constant, T is the stack temperature, F denotes the Faraday constant, and E^0 is the ideal cell voltage at the fuel cell operating conditions, as represented by Eq. 4.56.

$$E^0 = \frac{-\Delta G^0}{zF} + \frac{\Delta S^0}{zF}(T_{fc} - T_{ref}) \quad (4.56)$$

The first part of the Eq. 4.56 corresponds to the open circuit voltage of the fuel cell at standard conditions (i.e., 298.15 K and 101,325 kPa), which is equal to 1.18 V, and is related to cell maximum work and the Gibbs free energy as represented. The second part of the equation is the voltage reduction when the temperature increases from 25 ℃ to the desired fuel cell temperature. Moreover, the water activity is given by

$$a_{H_2O} = \frac{p_{H_2O}}{p^*_{H_2O}} = \frac{RH\%}{100} \quad (4.57)$$

where $RH\%$ is the percentage of relative humidity, p_{H_2O} is the water vapor pressure in equilibrium with the electrolyte and $p^*_{H_2O}$ is the saturated water vapour pressure at the same temperature and is given by a polynomial function with temperature range of 273 to 500 K [61].

$$p^*_{H_2O} = (142.076282 \cdot T^4 - 171026.12676 \cdot T^3 + 78013638.11584 \cdot T^2 - 15953375633.8471 \cdot T + 1231888491801.45) \cdot 10^{-10} \quad (4.58)$$

A reversible cell voltage, or ideal, is the voltage that can be obtained if the Gibbs free energy could be converted directly into electrical work without any losses. Practically, there are several irreversibilities within a fuel cell that causes the drop of the operating voltage. The difference between the theoretical voltage for the reaction and the actual cell voltage at a given current density is termed overpotential and is described in Eq. 4.59. The prominent sources of overpotential in a fuel cell are: anode activation losses ($V_{act,an}$), cathode activation losses ($V_{act,ca}$), and ohmic resistance (V_{ohm}). Each of the overpotentials is described in detail below.

$$V_{cell} = E_{rev}(T_{fc}, P_{fc}) - V_{act,an} - V_{act,ca} - V_{ohm} \quad (4.59)$$

Activation losses: In a fuel cell kinetic losses at the anode and cathode influenced by mass transport restriction concentration losses are calculated using the Butler-Volmer equations (Eq. 4.60 and 4.61) [67]. The effect of CO poisoning is included in the equation for anode activation loss. In order to avoid carbon monoxide poisoning at the anode, it is necessary to estimate its contamination on the reformate fuel. Thus, the exchange current density of hydrogen oxidation after CO poisoning (i_0^{CO}) is applied to study CO tolerance, through CO coverage (θ_{CO}) assuming bridge model of CO adsorption on Platinum (Pt) represented by Eq. 4.64.

$$V_{act,an} = \frac{RT_{fc}}{\alpha_{an}F} \sinh^{-1}\left(\frac{i}{2i_{0,an}(1-\theta_{CO})^2}\right) \quad (4.60)$$

$$V_{act,ca} = \frac{RT_{fc}}{\alpha_{ca}F} \sinh^{-1}\left(\frac{i}{2i_{0,ca}}\right) \quad (4.61)$$

where α_{an} and α_{ca} are the charge transfer coefficient of the anode and the cathode, respectively, i_0 is the exchange current density at the studied conditions per Pt unit area, given by Eq. 4.62 and 4.63 for the anode and cathode, respectively [61].

$$i_{0,an} = i_{0,an}^{ref} a_{c,an} L_{c,an} \left(\frac{C_{H_2,Pt}}{C_{Pt,an}^{ref}}\right)^{\kappa_{an}} \exp\left[-\frac{E_{c,an}}{RT_{fc}}\left(1 - \frac{T_{fc}}{T_{ref,an}}\right)\right] \quad (4.62)$$

$$i_{0,ca} = i_{0,ca}^{ref} a_{c,ca} L_{c,c} \left(\frac{C_{O_2,Pt}}{C_{Pt,ca}^{ref}}\right)^{\kappa_{ca}} \exp\left[-\frac{E_{c,ca}}{RT_{fc}}\left(1 - \frac{T_{fc}}{T_{ref,ca}}\right)\right] \quad (4.63)$$

Where i_0^{ref} is the exchange current density at reference temperature T_{ref} and reference dissolved oxygen concentration C_{ref}. a_c is the catalyst-specific accessible electrochemical suface area (covered by the electrolyte), L_c corresponds to the catalyst loading weight of platinum per unit area, C_{Pt} is the reactant concentration on the catalyst surface calculated from 4.45 and 4.44, κ is the reaction order, and E_c is the activation energy.

Because we are working with reformate gas, the effect of CO poisoning on the anode catalyst layer is accounted for using a modified equation of the exchange current density as follows

$$i_0^{CO} = i_0(1-\theta_{CO})^2 \quad (4.64)$$

where i_0^{CO} is the exchange current density for hydrogen oxidation after CO poisoning, i_0 is the exchange current density of hydrogen without CO presence. θ_{CO} is the surface coverage by CO as a function of temperature, we can write:

$$\theta_{CO} = a \ln\frac{[CO]}{[H2]} + b\ln(i) \cdot \ln\frac{[CO]}{[H2]} + c \quad (4.65)$$

where a, b and c are functions of the fuel cell temperature and can be found in [61].

$$a = -0.00012784 \cdot T_{fc}^2 + 0.11717499 \cdot T_{fc} - 26.62908873 \quad (4.66)$$

$$b = 0.0001416 \cdot T_{fc}^2 - 0.12813608 \cdot T_{fc} + 28.852463626 \quad (4.67)$$

$$c = -0.00034886 \cdot T_{fc}^2 - 0.31596903 \cdot T_{fc} - 70.11693333 \quad (4.68)$$

Ohmic losses: This voltage drop is mainly due to electrical resistance to the proton transfer through the membrane and the catalyst layers, as described by Eq. 4.69. Proton conductivity is the ability of a material to pass an electric current by the movement of protons, is one of the key characteristics of PA doped PBI.

$$V_{ohm} = \left(\frac{\sigma_m}{l_m}\right) i \quad (4.69)$$

where i is the current density, l_m is the membrane thickness and σ_m is the proton conductivity of the PBI membrane.

The proton conductivity is provided as a function of temperature (T) and relative humidity (RH) as presented in Eq. 4.70, 4.71 and 4.72.

$$\sigma_m = \frac{A}{T} \exp\left(\frac{-B}{RT}\right) \quad (4.70)$$

$$A = \exp\left[(k_1^a RH^3) + (k_2^a RH^2) + (k_3^a RH) + k_0^a\right] \quad (4.71)$$

$$B = (k_1^b RH^3) + (k_2^b RH^2) + (k_3^b RH) + k_0^b \quad (4.72)$$

Where A is the pre-exponential factor, and B the activation energy.

4.2.3 Efficiency of HT-PEMFC Integrated System

The objective functions that are used in the analysis of the HT-PEMFC integrated system performance are the fuel processor efficiency (η_{FP}), fuel conversion rate (γ_{CH4}), fuel cell efficiency (η_{fc}), and fuel cell exergy efficiency (ψ_{fc}).

The fuel processor efficiency is defined as the ratio of hydrogen produced in the fuel processor and the amount of chemicals available in the input gas (methane) entering the system:

$$\eta_{FP} = \frac{\dot{n}_{H_2} LHV_{H_2}}{\dot{n}_{CH_4} LHV_{CH_4}} \quad (4.73)$$

The fuel conversion rate for evaluating the fuel processor performance is defined as

$$\gamma_{CH4} = \left(1 - \frac{\dot{n}_{CH_4,fp,out}}{\dot{n}_{CH_4,fp,in}}\right) \quad (4.74)$$

where $\dot{n}_{CH_4,fp,in}$ and $\dot{n}_{CH_4,fp,out}$ is the molar flow of CH_4, respectively, on the input and output of the fuel processor.

The electrical efficiency is defined as the ratio of the electrical power output from the fuel cell stack divided by the chemical energy of the hydrogen from the fuel processor:

$$\eta_{ele,fc} = \frac{\dot{W}_{fc}}{\dot{n}_{H_2} LHV_{H_2}} \quad (4.75)$$

Exergy analysis evaluates the heat recovery opportunity of HT-PEMFC stack. This opportunity is created by the heat generated due to cell overpotentials and is calculated as follows:

$$\dot{Q}_{fc} = \dot{W}_{ele}\left(\frac{E_{rev}(T_{fc}, P_{fc})}{V_{cell}} - 1\right) \quad (4.76)$$

The thermal efficiency of the fuel cell is analyzed from the electric power generated and the lower heating value (LHV) of hydrogen as:

$$\eta_{thermal,fc} = \frac{\dot{Q}_{fc}}{\dot{n}_{H_2} LHV_{H_2}} \quad (4.77)$$

The cogeneration efficiency of the fuel cell is defined as:

$$\eta_{cog,fc} = \frac{\dot{W}_{fc} + \dot{Q}_{fc}}{\dot{n}_{H_2} \dot{e}x_{H_2}} \quad (4.78)$$

The electrical exergy efficiency ($\psi_{ele,fc}$), the thermal exergy efficiency ($\psi_{thermal,fc}$) of the fuel cell are defined as Eq. 4.79 and 4.80, respectively. The fuel cell cogeneration exergy efficiency ($\psi_{cog,fc}$) is shown in Eq. 4.81.

$$\psi_{ele,fc} = \frac{\dot{W}_{fc}}{\dot{n}_{H_2} \dot{e}x_{H_2}} \quad (4.79)$$

$$\psi_{thermal,fc} = \frac{\left(1 - \frac{T_0}{T_{fc}}\right)\dot{Q}_{fc}}{\dot{n}_{H_2} LHV_{H_2}} \quad (4.80)$$

$$\psi_{cog,fc} = \frac{\dot{W}_{fc} + \left(1 - \frac{T_0}{T_{fc}}\right)}{\dot{n}_{H_2} \dot{e}x_{H_2}} \quad (4.81)$$

4.3 Auxiliary Units

In this section, auxiliary units behavior are presented using thermodynamic balances.

4.3.1 Air Compressor

The ideal performance of a compressor is usually associated with an isentropic process where no entropy is created. The isentropic efficiency of the compressor is defined by the ratio of its ideal work (w_{cs}) and its actual work (w_{ca}) for the same initial conditions and the same exiting pressure, and is calculated using Eq. 4.82.

$$\eta_{comp,a} = \frac{w_{cs}}{w_{ca}} = \frac{h_{21s} - h_1}{h_{21} - h_1} \quad (4.82)$$

The ideal temperature of the working fluid leaving the control volume (T_{21s}) can be determined using the

following equality.

$$\frac{T_{21s}}{T_1} = \left(\frac{P_{21}}{P_1}\right)^{\frac{\gamma-1}{\gamma}} \quad (4.83)$$

where T_1 is the temperature of the air entering the compressor, P_1 and P_{21} are the inlet and outlet pressure of air, respectively, and γ is the ratio of specific heats.

$$\bar{h}_{21s} = \sum_j X_j \bar{h}_j(T_{21s}) \quad (4.84)$$

$$\bar{s}_{21s} = \sum_j X_j \bar{s}_j(T_{21s}, P_{j,21}) \quad (4.85)$$

4.3.2 Fuel Compressor

The isentropic efficiency of the fuel compressor is defined in the same way as the air compressor as presented in Eq. 4.86.

$$\eta_{comp,f} = \frac{w_{cs}}{w_{ca}} = \frac{h_{4s} - h_2}{h_4 - h_2} \quad (4.86)$$

The ideal temperature of the working fluid leaving the control volume (T_{4s}) can be determined using the following equality.

$$\frac{T_{4s}}{T_2} = \left(\frac{P_4}{P_2}\right)^{\frac{\gamma-1}{\gamma}} \quad (4.87)$$

where T_2 is the temperature of the fuel entering the compressor, P_2 and P_4 are, respectively, the fuel inlet and outlet pressures.

$$\bar{h}_{2s} = \sum_j X_j \bar{h}_j(T_{2s}) \quad (4.88)$$

$$\bar{s}_{2s} = \sum_j X_j \bar{s}_j(T_{2s}, P_{j,2}) \quad (4.89)$$

4.3.3 Pump

The power requirement of the pump is calculated as follows:

$$\dot{W}_p = \dot{n}_{water} \frac{\Delta P \upsilon}{\eta_p} \quad (4.90)$$

where ΔP is the boost in pressure of liquid water, υ is the specific volume of water at reference conditions and η_p is the efficiency of the pump. The amount of water introduced in the system is estimated from an optimization of the fuel processor. This estimation depends on the temperature of the steam reformer and water gas shifting and the steam-to-carbon ratio.

4.3.4 Combustion Chamber

Methane is mixed with the injected cathode exhaust and the compressed preheated air in the combustion chamber. The fuel-air equivalence ratio (λ) is given by the following equation.

$$\lambda = \frac{\dot{n}_f}{\dot{n}_a} \quad (4.91)$$

where $\dot{n}_f$ and $\dot{n}_a$ are the respective molar flow rate of the fuel and the air. The complete combustion reaction can be written as:

$$\lambda \underbrace{(y_{CH_4}CH_4 + y_{CO}CO + y_{H_2}H_2 + y_{CO_2}CO_2 + y_{H_2O}H_2O)}_{fuel} + \underbrace{(y_{O_2}O_2 + y_{CO_2}CO_2 + y_{H_2O}H_2O + y_{N_2}N_2)}_{air}$$
$$\longrightarrow \underbrace{y_{CO_2}CO_2 + y_{H_2O}H_2O + y_{N_2}N_2 + y_{O_2}O_2}_{exhaust\ gases} \quad (4.92)$$

The final equations for the mole fractions of exhaust gases can be determined using the atomic balance of the elements present in the combustion equation, thus, carbon (C), hydrogen (H), nitrogen (N) and oxygen (O), this can be seen in the following equations:

C: $y_{CO_2} + \lambda(y_{CH_4} + y_{CO} + y_{CO_2,fuel}) = y_{CO_2,out}$

H: $y_{H_2O} + \lambda(0.5y_{CH_4} + y_{H_2} + y_{H_2O,fuel}) = y_{H_2O,out}$

N: $y_{N_2} = y_{N_2,out}$

O: $y_{O_2} - \lambda(1.25y_{CH_4} + 0.5(y_{CO} + y_{H_2})) = y_{O_2,out}$

The theoretical fuel-air ratio is calculated from:

$$FAR_{theoretical} = \frac{\dot{m}_{fuel}}{\dot{m}_{air}} = \frac{\dot{n}_{fuel}}{\dot{n}_{air}} \frac{M_{fuel}}{M_{air}} \quad (4.93)$$

where M_{air} and M_{fuel} are the molecular weight of air and fuel, respectively.
The actual fuel-air ratio is related to the combustion chamber efficiency (η_{cc}) as follows:

$$\eta_{cc} = \frac{FAR_{theoretical}}{FAR_{actual}} \quad (4.94)$$

Moreover, the adiabatic flame temperature (T_P) can be found using an iterative enthalpy balance method, where T_P is assigned a starting value and the iteration stops when $H_P(T_P) \approx H_R(T_R)$, i.e. the enthalpy of the product mixture meets the enthalpy of reactants [68].
Therefore, a combustion chamber under adiabatic conditions and no work interactions is governed by the following equation

$$\sum_{prod} \dot{n}_j[\bar{h}_f^0 + (\bar{h} - \bar{h}^0)]_j = \sum_{reag} \dot{n}_j[\bar{h}_f^0 + (\bar{h} - \bar{h}^0)]_j \quad (4.95)$$

where j is the species component.
This method assumes complete combustion to the major products.

4.3.5 Gas Turbine

The exhaust gases from the combustion chamber are then expanded through the gas turbine where its pressure and temperature drops. The stream outgoing the turbine will then be recovered and supplied to several units for heat management. The work provided by the gas turbine is used to drive both of the compressors (fuel and air compressor), thus:

$$\dot{W}_t = \dot{W}_{comp,air} + \dot{W}_{comp,fuel} \quad (4.96)$$

The turbine inlet temperature is known from the previous calculations as it corresponds to the adiabatic flame temperature, therefore its outlet temperature can be determined using the isentropic efficiency of the turbine, which is governed by the ratio of its actual work (w_{t_a}) and its ideal work (w_{t_s}).

$$\eta_t = \frac{w_{t_a}}{w_{t_s}} = \frac{h_{11} - h_{12}}{h_{11} - h_{12s}} \quad (4.97)$$

The pressure drop during exhaust gases expansion can be determined according to Eq. 4.98.

$$\frac{P_{12}}{P_{11}} = \left(\frac{T_{12s}}{T_{11}}\right)^{\frac{\gamma}{\gamma-1}} \quad (4.98)$$

To determine the isentropic enthalpy and entropy, the following equation are added to the MATLAB program.

$$\bar{h}_{12s} = \sum_j X_j \bar{h}_j(T_{12s}) \quad (4.99)$$

$$\bar{s}_{12s} = \sum_j X_j \bar{s}_j(T_{12s}, P_{j,12}) \quad (4.100)$$

4.3.6 Heat Exchangers

The general equation for a heat exchanger can be described as follows.

$$\eta_{HX} = \frac{\dot{n}_{cold}(h_{out} - h_{in})}{\dot{n}_{hot}(h_{in} - h_{out})} \quad (4.101)$$

where the $\dot{n}_{cold}$ and $\dot{n}_{hot}$ represent the cold and the hot streams, respectively involved in the process. The heat recovery steam generator is an energy recovery heat exchanger that combines a gas turbine cycle and a vapor power cycle. The efficiency of the HSRG can be calculated as follows.

$$\eta_{HRSG} = \frac{\dot{n}_w(h_{19} - h_{20})}{\dot{n}_{eg}(h_{17} - h_{18})} \quad (4.102)$$

where $\dot{n}_{eg}$ is the molar flow of the exhaust gases. Similarly to the HRSG, the heat exchangers can be found through recuperator effectiveness, this way the general equation above can be written as:

$$\eta_{HX-1} = \frac{\dot{n}_4(h_5 - h_4)}{\dot{n}_{eg}(h_{16} - h_{17})} \quad (4.103)$$

$$\eta_{HX-2} = \frac{\dot{n}_{eg}(h_{15} - h_{14})}{\dot{n}_6(h_6 - h_7)} \quad (4.104)$$

$$\eta_{HX-3} = \frac{\dot{n}_{21}(h_{22} - h_{21a})}{\dot{n}_{23}(h_{23} - h_{24})} \quad (4.105)$$

$$\eta_{HX-4} = \frac{\dot{n}_{9}(h_{10} - h_{9})}{\dot{n}_{eg}(h_{12} - h_{13})} \quad (4.106)$$

for heat exchanger 1, heat exchanger 2, heat exchanger 3, and heat exchanger 4, respectively.

4.4 Thermodynamic Balances

The proposed system feasibility is evaluated using the concept of control volume. A fixed volume is defined for each unit by a control surface (discontinuous line) and its thermodynamics is evaluated. Thermodynamic evaluation is performed to every unit using molar flow, energy, entropy, and exergy balances in this exact order.
The control volume of each unit is illustrated, followed by the respective thermodynamic balance equations.

4.4.1 Air Compressor

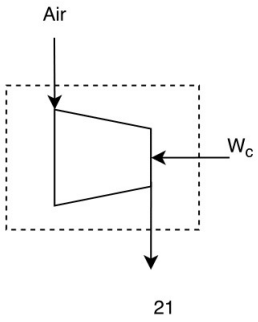

Figure 4.2: Air Compressor control volume

Molar balance:

$$\dot{n}_1 = \dot{n}_{21} = \dot{n}_{air} \quad (4.107)$$

Energy balance:

$$\dot{n}_1\bar{h}_1 - \dot{n}_{21}\bar{h}_{21} + \dot{W}_{comp,a} = 0 \quad (4.108)$$
$$\dot{W}_{comp,a} = \dot{n}_{air}(\bar{h}_{21} - \bar{h}_1) \quad (4.109)$$

Entropy balance:

$$\dot{n}_1\bar{s}_1 - \dot{n}_{21}\bar{s}_{21} + \dot{S}_{gen,comp} = 0 \quad (4.110)$$
$$\dot{S}_{gen,comp} = \dot{n}_{air}(\bar{s}_{21} - \bar{s}_1) \quad (4.111)$$

Exergy balance:

$$\dot{n}_1 \bar{e}x_1 - \dot{n}_{21} \bar{e}x_{21} + \dot{W}_{comp,a} - \dot{E}x_{dest,comp} = 0 \quad (4.112)$$

$$\dot{E}x_{dest,comp} = \dot{n}_{air}(\bar{e}x_1 - \bar{e}x_{21}) + \dot{W}_{comp,a} \quad (4.113)$$

4.4.2 Fuel Compressor

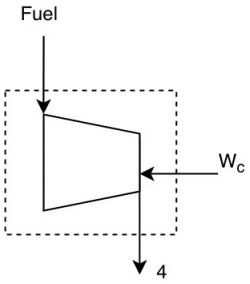

Figure 4.3: Fuel Compressor control volume

Molar balance:

$$\dot{n}_2 = \dot{n}_4 = \dot{n}_{fuel} \quad (4.114)$$

Energy balance:

$$\dot{n}_2 \bar{h}_2 - \dot{n}_4 \bar{h}_4 + \dot{W}_{comp,f} = 0 \quad (4.115)$$

$$\dot{W}_{comp,f} = \dot{n}_{fuel}(\bar{h}_4 - \bar{h}_2) \quad (4.116)$$

Entropy balance:

$$\dot{n}_2 \bar{s}_2 - \dot{n}_4 \bar{s}_4 + \dot{S}_{gen,comp} = 0 \quad (4.117)$$

$$\dot{S}_{gen,comp} = \dot{n}_{fuel}(\bar{s}_4 - \bar{s}_2) \quad (4.118)$$

Exergy balance:

$$\dot{n}_2 \bar{e}x_2 - \dot{n}_4 \bar{e}x_4 + \dot{W}_{comp,f} - \dot{E}x_{dest,comp} = 0 \quad (4.119)$$

$$\dot{E}x_{dest,c_f} = \dot{n}_{fuel}(\bar{e}x_2 - \bar{e}x_4) + \dot{W}_{comp,f} \quad (4.120)$$

4.4.3 Pump

Molar balance:

$$\dot{n}_3 = \dot{n}_{19} = \dot{n}_{water} \quad (4.121)$$

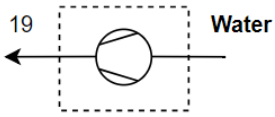

Figure 4.4: Pump control volume

Energy balance:

$$\dot{n}_3\bar{h}_3 - \dot{n}_{19}\bar{h}_{19} + \dot{W}_p = 0 \quad (4.122)$$

$$\dot{W}_p = \dot{n}_{water}(\bar{h}_{19} - \bar{h}_3) \quad (4.123)$$

Entropy balance:

$$\dot{n}_3\bar{s}_3 - \dot{n}_{19}\bar{s}_{19} + \dot{S}_{gen,p} = 0 \quad (4.124)$$

$$\dot{S}_{gen,p} = \dot{n}_{water}(\bar{s}_{19} - \bar{s}_3) \quad (4.125)$$

Exergy balance:

$$\dot{n}_3\bar{e}x_3 - \dot{n}_{19}\bar{e}x_{19} + \dot{W}_p - \dot{E}x_{dest,p} = 0 \quad (4.126)$$

$$\dot{E}x_{dest,p} = \dot{n}_{water}(\bar{e}x_3 - \bar{e}x_{19}) + \dot{W}_p \quad (4.127)$$

4.4.4 Steam Reformer

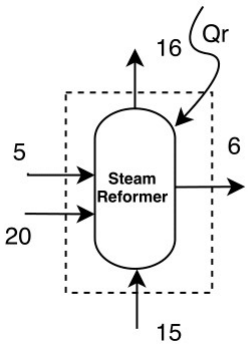

Figure 4.5: Steam reformer control volume

Molar balance:

$$\dot{n}_5 + \dot{n}_{20} = \dot{n}_6 \quad (4.128)$$

$$\dot{n}_{15} = \dot{n}_{16} \quad (4.129)$$

Energy balance:

$$\dot{n}_5\bar{h}_5 + \dot{n}_{20}\bar{h}_{20} - \dot{n}_6\bar{h}_6 + \dot{Q}_r = 0 \quad (4.130)$$

$$\dot{Q}_r = \dot{n}_6\bar{h}_6 - \dot{n}_5\bar{h}_5 - \dot{n}_{20}\bar{h}_{20} \quad (4.131)$$

Entropy balance:

$$\dot{n}_5\bar{s}_5 + \dot{n}_{20}\bar{s}_{20} - \dot{n}_6\bar{s}_6 + \frac{\dot{Q}}{T_r} + \dot{S}_{gen,r} = 0 \quad (4.132)$$

$$\dot{S}_{gen,r} = \dot{n}_6\bar{s}_6 - \dot{n}_5\bar{s}_5 - \dot{n}_{20}\bar{s}_{20} - \frac{\dot{Q}}{T_r} \quad (4.133)$$

Exergy balance:

$$\dot{n}_5\bar{e}x_5 + \dot{n}_{20}\bar{e}x_{20} - \dot{n}_6\bar{e}x_6 + \left(1 - \frac{T_0}{T_r}\right)\dot{Q}_r - \dot{E}x_{dest,r} = 0 \quad (4.134)$$

$$\dot{E}x_{dest,r} = \dot{n}_5\bar{e}x_5 + \dot{n}_{20}\bar{e}x_{20} - \dot{n}_6\bar{e}x_6 - \left(1 - \frac{T_0}{T_r}\right)\dot{Q}_r \quad (4.135)$$

where T_r is the temperature of the steam reformer, and $\dot{Q}_r$ is the heat required by the reformer to perform the reaction and maintain the temperature of the unit, provided by the turbine.

4.4.5 Water Gas Shifting

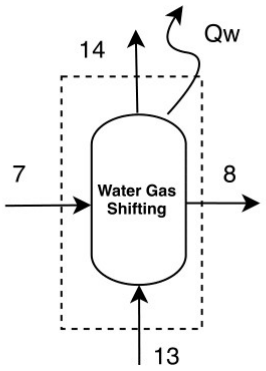

Figure 4.6: Water Gas Sifting control volume

Molar balance:

$$\dot{n}_7 = \dot{n}_8 \quad (4.136)$$

$$\dot{n}_{13} = \dot{n}_{14} \quad (4.137)$$

Energy balance:

$$\dot{n}_7\bar{h}_7 - \dot{n}_8\bar{h}_8 + \dot{Q}_w = 0 \quad (4.138)$$

$$\dot{Q}_w = \dot{n}_8\bar{h}_8 - \dot{n}_7\bar{h}_7 \quad (4.139)$$

Entropy balance:

$$\dot{n}_7\bar{s}_7 - \dot{n}_8\bar{s}_8 + \frac{\dot{Q}_w}{T_w} + \dot{S}_{gen,w} = 0 \quad (4.140)$$

$$\dot{S}_{gen,w} = \dot{n}_8\bar{s}_8 - \dot{n}_7\bar{s}_7 - \frac{\dot{Q}_w}{T_w} \quad (4.141)$$

Exergy balance:

$$\dot{n}_7\bar{e}x_7 - \dot{n}_8\bar{e}x_8 + \left(1 - \frac{T_0}{T_w}\right)\dot{Q}_w - \dot{E}x_{dest,w} = 0 \quad (4.142)$$

$$\dot{E}x_{dest,w} = \dot{n}_7\bar{e}x_7 - \dot{n}_8\bar{e}x_8 + \left(1 - \frac{T_0}{T_w}\right)\dot{Q}_w \quad (4.143)$$

4.4.6 HT-PEMFC

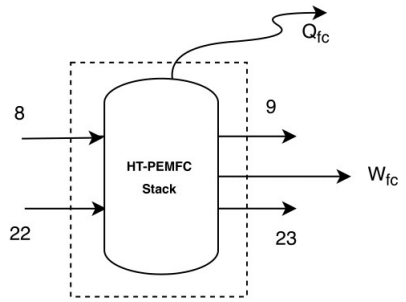

Figure 4.7: Fuel cell control volume

Molar balance:

$$\dot{n}_8 + \dot{n}_{22} = \dot{n}_9 + \dot{n}_{23} \quad (4.144)$$

Energy balance:

$$\dot{n}_8\bar{h}_8 + \dot{n}_{22}\bar{h}_{22} - \dot{n}_9\bar{h}_9 - \dot{n}_{23}\bar{h}_{23} - \dot{Q}_{rxn} - \dot{W}_{fc} = 0 \quad (4.145)$$

$$\dot{W}_{fc} = \dot{n}_8\bar{h}_8 + \dot{n}_{22}\bar{h}_{22} - \dot{n}_9\bar{h}_9 - \dot{n}_{23}\bar{h}_{23} - \dot{Q}_{rxn} \quad (4.146)$$

Entropy balance:

$$\dot{n}_8\bar{s}_8 + \dot{n}_{22}\bar{s}_{22} - \dot{n}_9\bar{s}_9 - \dot{n}_{23}\bar{s}_{23} - \frac{\dot{Q}_{rxn}}{T_{rxn}} + \dot{S}_{gen,fc} = 0 \quad (4.147)$$

$$\dot{S}_{gen,fc} = \dot{n}_9\bar{s}_9 + \dot{n}_{23}\bar{s}_{23} - \dot{n}_8\bar{s}_8 - \dot{n}_{22}\bar{s}_{22} + \frac{\dot{Q}_{rxn}}{T_{fc}} \quad (4.148)$$

Exergy balance:

$$\dot{n}_8\bar{e}x_8 + \dot{n}_{22}\bar{e}x_{22} - \dot{n}_9\bar{e}x_9 - \dot{n}_{23}\bar{e}x_{23} - \left(1 - \frac{T_0}{T_{fc}}\right)\dot{Q}_{rxn} - \dot{W}_{fc} - \dot{E}x_{dest,fc} = 0 \quad (4.149)$$

$$\dot{E}x_{dest,fc} = \dot{n}_8\bar{e}x_8 + \dot{n}_{22}\bar{e}x_{22} - \dot{n}_9\bar{e}x_9 - \dot{n}_{23}\bar{e}x_{23} + \left(1 - \frac{T_0}{T_{fc}}\right)\dot{Q}_{rxn} - \dot{W}_{fc} \quad (4.150)$$

4.4.7 Combustion Chamber

Molar balance:

$$\dot{n}_{10} + \dot{n}_{21b} = \dot{n}_{11} \quad (4.151)$$

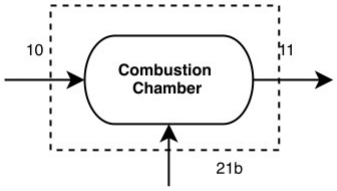

Figure 4.8: Combustion Chamber control volume

Energy balance:

$$\dot{n}_{10}\bar{h}_{10} + \dot{n}_{21b}\bar{h}_{21b} - \dot{n}_{11}\bar{h}_{11} = 0 \quad (4.152)$$
$$\dot{n}_{10}\bar{h}_{10} + \dot{n}_{21b}\bar{h}_{21b} = \dot{n}_{11}\bar{h}_{11} \quad (4.153)$$

Entropy balance:

$$\dot{n}_{10}\bar{s}_{10} + \dot{n}_{21b}\bar{s}_{21b} - \dot{n}_{11}\bar{s}_{11} + \dot{S}_{gen,cc} = 0 \quad (4.154)$$
$$\dot{S}_{gen,cc} = \dot{n}_{11}\bar{s}_{11} - \dot{n}_{10}\bar{s}_{10} + \dot{n}_{21b}\bar{s}_{21b} \quad (4.155)$$

Exergy balance:

$$\dot{n}_{10}\bar{e}x_{10} + \dot{n}_{21b}\bar{e}x_{21b} - \dot{n}_{11}\bar{e}x_{11} - \dot{E}x_{dest,cc} = 0 \quad (4.156)$$
$$\dot{E}x_{dest,cc} = \dot{n}_{10}\bar{e}x_{10} + \dot{n}_{21b}\bar{e}x_{21b} - \dot{n}_{11}\bar{e}x_{11} \quad (4.157)$$

4.4.8 Gas Turbine

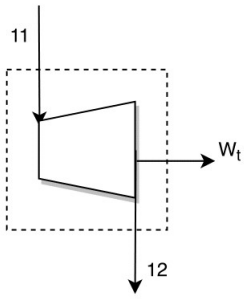

Figure 4.9: Gas turbine control volume

Molar balance:

$$\dot{n}_{11} = \dot{n}_{12} = \dot{n}_{eg} \quad (4.158)$$

Energy balance:

$$\dot{n}_{11}\bar{h}_{11} - \dot{n}_{12}\bar{h}_{12} - \dot{W}_t = 0 \quad (4.159)$$
$$\dot{W}_t = \dot{n}_{eg}(\bar{h}_{11} - \bar{h}_{12}) \quad (4.160)$$

Entropy balance:

$$\dot{n}_{11}\bar{s}_{11} - \dot{n}_{12}\bar{s}_{12} + \dot{S}_{gen,t} = 0 \quad (4.161)$$

$$\dot{S}_{gen,t} = \dot{n}_{eg}(\bar{s}_{12} - \bar{s}_{11}) \quad (4.162)$$

Exergy balance:

$$\dot{n}_{11}\bar{e}x_{11} - \dot{n}_{12}\bar{e}x_{12} - \dot{W}_t - \dot{E}x_{dest,t} = 0 \quad (4.163)$$

$$\dot{E}x_{dest,t} = \dot{n}_{eg}(\bar{e}x_{11} - \bar{e}x_{12}) - \dot{W}_t \quad (4.164)$$

4.4.9 Heat Exchangers

4.4.9.1 HX-1

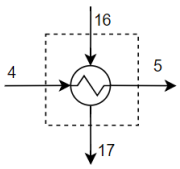

Figure 4.10: HX-1 control volume

Molar balance:

$$\dot{n}_4 = \dot{n}_5 = \dot{n}_{CH_4} \quad (4.165)$$

$$\dot{n}_{16} = \dot{n}_{17} = \dot{n}_{eg} \quad (4.166)$$

Energy balance:

$$\dot{n}_4\bar{h}_4 + \dot{n}_{16}\bar{h}_{16} = \dot{n}_5\bar{h}_5 + \dot{n}_{17}\bar{h}_{17} \quad (4.167)$$

Entropy balance:

$$\dot{S}_{gen,hx} = \dot{n}_5\bar{s}_5 + \dot{n}_{17}\bar{s}_{17} - \dot{n}_4\bar{s}_4 - \dot{n}_{16}\bar{s}_{16} \quad (4.168)$$

Exergy balance:

$$\dot{E}x_{dest,hx} = \dot{n}_4\bar{e}x_4 - \dot{n}_5\bar{e}x_5 + \dot{n}_{16}\bar{e}x_{16} - \dot{n}_{17}\bar{e}x_{17} \quad (4.169)$$

4.4.9.2 HX-2

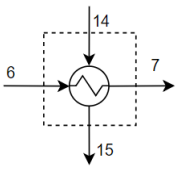

Figure 4.11: HX-2 control volume

Molar balance:

$$\dot{n}_6 = \dot{n}_7 \quad (4.170)$$
$$\dot{n}_{14} = \dot{n}_{15} \quad (4.171)$$

Energy balance:

$$\dot{n}_6\bar{h}_6 + \dot{n}_{14}\bar{h}_{14} = \dot{n}_7\bar{h}_7 + \dot{n}_{15}\bar{h}_{15} \quad (4.172)$$

Entropy balance:

$$\dot{S}_{gen,hx} = \dot{n}_7\bar{s}_7 + \dot{n}_{15}\bar{s}_{15} - \dot{n}_6\bar{s}_6 - \dot{n}_{14}\bar{s}_{14} \quad (4.173)$$

Exergy balance:

$$\dot{E}x_{dest,hx} = \dot{n}_6\bar{e}x_6 - \dot{n}_7\bar{e}x_7 + \dot{n}_{14}\bar{e}x_{14} - \dot{n}_{15}\bar{e}x_{15} \quad (4.174)$$

4.4.9.3 HX-3

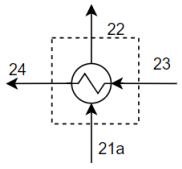

Figure 4.12: HX-3 control volume

Molar balance:

$$\dot{n}_{21a} = \dot{n}_{22} \quad (4.175)$$
$$\dot{n}_{23} = \dot{n}_{24} \quad (4.176)$$

Energy balance:

$$\dot{n}_{21a}\bar{h}_{21a} + \dot{n}_{23}\bar{h}_{23} = \dot{n}_{22}\bar{h}_{22} + \dot{n}_{24}\bar{h}_{24} \quad (4.177)$$

Entropy balance:

$$\dot{S}_{gen,hx} = \dot{n}_{22}\bar{s}_{22} + \dot{n}_{24}\bar{s}_{24} - \dot{n}_{21a}\bar{s}_{21a} - \dot{n}_{23}\bar{s}_{23} \quad (4.178)$$

Exergy balance:

$$\dot{E}x_{dest,hx} = \dot{n}_{21a}\bar{e}x_{21a} - \dot{n}_{23}\bar{e}x_{23} + \dot{n}_{22}\bar{e}x_{22} - \dot{n}_{24}\bar{e}x_{24} \quad (4.179)$$

4.4.9.4 HX-4

Molar balance:

$$\dot{n}_9 = \dot{n}_{10} \quad (4.180)$$
$$\dot{n}_{12} = \dot{n}_{13} \quad (4.181)$$

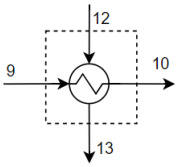

Figure 4.13: HX-4 control volume

Energy balance:

$$\dot{n}_9\bar{h}_9 + \dot{n}_{12}\bar{h}_{12} = \dot{n}_{10}\bar{h}_{10} + \dot{n}_{13}\bar{h}_{13} \quad (4.182)$$

Entropy balance:

$$\dot{S}_{gen,hx} = \dot{n}_{10}\bar{s}_{10} + \dot{n}_{13}\bar{s}_{13} - \dot{n}_9\bar{s}_9 - \dot{n}_{12}\bar{s}_{12} \quad (4.183)$$

Exergy balance:

$$\dot{E}x_{dest,hx} = \dot{n}_9\bar{e}x_9 - \dot{n}_{10}\bar{e}x_{10} + \dot{n}_{12}\bar{e}x_{12} - \dot{n}_{13}\bar{e}x_{13} \quad (4.184)$$

4.4.10 Heat Recovery Steam Generator

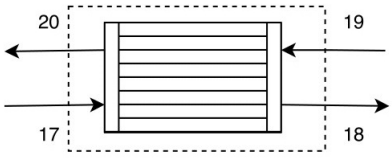

Figure 4.14: Heat Recovering Steam Generator control volume

Molar balance:

$$\dot{n}_{19} = \dot{n}_{20} \quad (4.185)$$
$$\dot{n}_{17} = \dot{n}_{18} \quad (4.186)$$

Energy balance:

$$\dot{n}_{19}\bar{h}_{19} + \dot{n}_{17}\bar{h}_{17} = \dot{n}_{20}\bar{h}_{20} + \dot{n}_{18}\bar{h}_{18} \quad (4.187)$$

Entropy balance:

$$\dot{S}_{gen,hrsg} = \dot{n}_{18}\bar{s}_{18} + \dot{n}_{20}\bar{s}_{20} - \dot{n}_{19}\bar{s}_{19} - \dot{n}_{17}\bar{s}_{17} \quad (4.188)$$

Exergy balance:

$$\dot{E}x_{dest,hrsg} = \dot{n}_{19}\bar{e}x_{19} - \dot{n}_{20}\bar{e}x_{20} + \dot{n}_{17}\bar{e}x_{17} - \dot{n}_{18}\bar{e}x_{18} \quad (4.189)$$

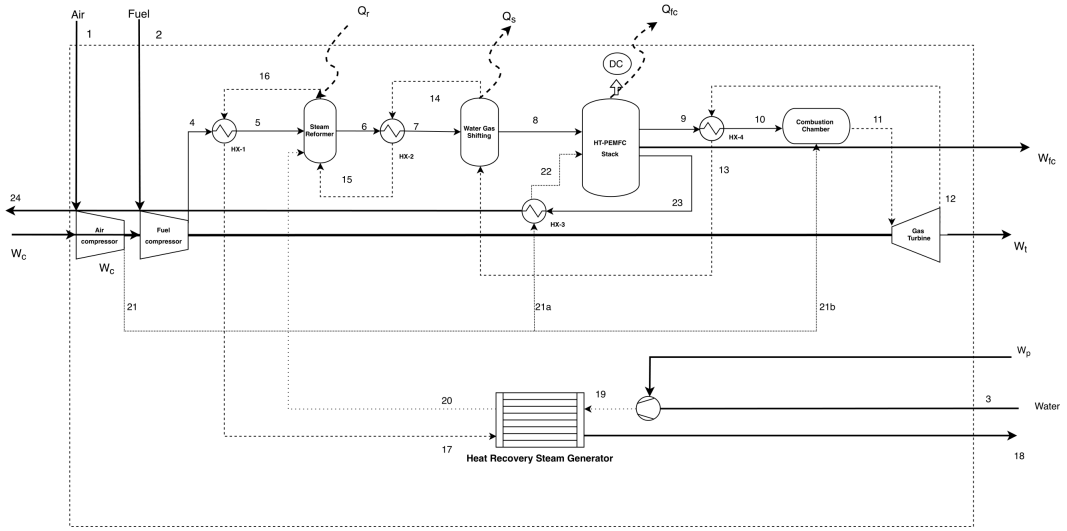

Figure 4.15: Overall system control volume

4.5 Overall System

Molar balance:

$$\dot{n}_1 + \dot{n}_2 + \dot{n}_3 = \dot{n}_{18} + \dot{n}_{24} \quad (4.190)$$

Energy balance:

$$\dot{E}_1 + \dot{E}_2 + \dot{E}_3 = \dot{E}_{18} + \dot{E}_{24} + \dot{W}_{fc} + \dot{W}_t - \dot{W}_{comp,a} - \dot{W}_{comp,f} + \dot{Q}_{fc} + \dot{Q}_{hx} \quad (4.191)$$

Entropy balance:

$$\dot{S}_{gen,GL} + \dot{S}_1 + \dot{S}_2 + \dot{S}_3 = \dot{S}_{18} + \dot{S}_{24} + \left(1 - \frac{T_0}{T_{fc}}\right)\dot{Q}_{fc} + \left(1 - \frac{T_0}{T_{hx}}\right)\dot{Q}_{hx} \quad (4.192)$$

Exergy balance:

$$\dot{E}x_1 + \dot{E}x_2 + \dot{E}x_3 - \dot{E}x_{dest,GL} = \dot{E}x_{18} + \dot{E}x_{24} + \dot{W}_{fc} + \dot{W}_t - \dot{W}_{comp,a} - \dot{W}_{comp,f} \quad (4.193)$$

4.5.1 Entropy Generation and Exergy Destruction

The overall entropy generation rate ($\dot{S}_{gen,total}$) and the overall exergy destruction rate ($\dot{E}x_{dest,total}$) can be calculated by adding the individual entropy generation rates and the exergy destruction rates, respectively, of each unit of the system. The $\dot{S}_{gen,total}$ and the $\dot{E}x_{dest,total}$ are calculated using the Eq. 4.194 and 4.195, respectively.

$$\dot{S}_{gen,total} = \dot{S}_{gen,comp_{air}} + \dot{S}_{gen,comp_{fuel}} + \dot{S}_{gen,p} + \dot{S}_{gen,r} + \dot{S}_{gen,w} + \dot{S}_{gen,fc} + \dot{S}_{gen,cc} + \dot{S}_{gen,t} + \dot{S}_{gen,hx_1} + \dot{S}_{gen,hx_2} + \dot{S}_{gen,hx_3} + \dot{S}_{gen,hx_4} + \dot{S}_{gen,hrsg} \quad (4.194)$$

$$\dot{E}x_{dest,total} = \dot{E}x_{dest,comp_a} + \dot{E}x_{dest,comp_f} + \dot{E}x_{dest,p} + \dot{E}x_{dest,r} + \dot{E}x_{dest,w} + \dot{E}x_{dest,fc} + \dot{E}x_{dest,cc} + \dot{E}x_{dest,t} + \dot{E}x_{dest,hx_1} + \dot{E}x_{dest,hx_2} + \dot{E}x_{dest,hx_3} + \dot{E}x_{dest,hx_4} + \dot{E}x_{dest,hrsg} \quad (4.195)$$

4.6 Overall System efficiency

The electrical energy efficiency (η_{ele}) of the system is evaluated considering the APU power output ($\dot{W}_{APU}$) and the LHV of the fuel input and it can be determined as follows:

$$\eta_{ele} = \frac{\dot{W}_{APU}}{\dot{n}_{fuel} LHV_{fuel}} \quad (4.196)$$

The electrical exergy efficiency (ψ_{ele}) of the system depends of the APU power output and the exergy of the input fuel as demosntrated by Eq. 4.197.

$$\psi_{ele} = \frac{\dot{W}_{APU}}{\dot{n}_{fuel} \dot{e}x_{fuel}} \quad (4.197)$$

where $\dot{n}_{fuel}$ is the molar flow of the input fuel and LHV_{fuel} is the respective lower heating value. The net power output of the system can be calculated from the produced power of the fuel cell and gas turbine and the required power by the pump and compressor as shown in Eq. 4.198.

$$\dot{W}_{APU} = \dot{W}_{fc} + \dot{W}_t - \dot{W}_p - \dot{W}_{comp,a} - \dot{W}_{comp,f} \quad (4.198)$$

In addition, the thermal efficiency ($\eta_{thermal}$) and the cogeneration efficiency ($\eta_{sys,cog}$) of the HT-PEMFC APU system where both the electrical and thermal output are included are calculated in Eq. 4.199 and 4.200, respectively. The $Q_{thermal}$ is the heat recovery from the fuel cell and the auxiliary units.

$$\eta_{thermal} = \frac{\dot{Q}_{thermal}}{\dot{n}_{fuel} LHV_{fuel}} \quad (4.199)$$

$$\eta_{sys,cog} = \frac{\dot{W}_{APU} + \dot{Q}_{thermal}}{\dot{n}_{fuel} LHV_{fuel}} \quad (4.200)$$

The thermal exergy efficiency ($\psi_{thermal}$) and the cogeneration exergy efficiency ($\psi_{sys,cog}$) of the system are shown in Eq. 4.201 and 4.202, respectively.

$$\psi_{thermal} = \frac{\left(1 - \frac{T_0}{T_{HF}}\right) \dot{Q}_{thermal}}{\dot{n}_{fuel} \dot{e}x_{fuel}} \quad (4.201)$$

$$\psi_{sys,cog} = \frac{\dot{W}_{APU} + \left(1 - \frac{T_0}{T_{HF}}\right) \dot{Q}_{thermal}}{\dot{n}_{fuel} \dot{e}x_{fuel}} \quad (4.202)$$

The degree of thermodynamic perfection (ε) of the overall process is defined as Eq. 4.203.

$$\varepsilon = \frac{\dot{E}x_{18} + \dot{E}x_{24} + \dot{W}_{APU}}{\dot{E}x_1 + \dot{E}x_2 + \dot{E}x_3} \quad (4.203)$$

4.7 Numerical solution

At design conditions, the composition of the reformate gas fed to HT-PEMFC can be calculated from the fuel processor model using the Gibbs minimization method to calculate the equilibrium compositions of species i.
The performance of the cell is estimated from the Stefan Maxwell, Fick's law and electrochemical model. Stefan Maxwell equation is integrated and changed from ordinary differential equation to algebraic equation, which is solved to give the gas composition at the interface between electrode and electrolyte film. The CO poisoning model is included in the calculation of the anode activation loss.
In addition, considering the auxiliary units, the power requirement of the compressors and pump are calculated based on isentropic efficiency. The combustor model is used to determine its product compositions and the adiabatic flame temperature, and the heat recovery model empowers the heat exchangers and the heat recovery steam generator for heat management of the overall system along with the gas turbine. In addition, the power of the HT-PEMFC APU is determined to meet the electrical needs of the aircraft during the entire flight envelope. Finally, the energy and exergy analysis of the system are evaluated and the overall system efficiency is determined considering the electrical and thermal system, as well as the combination of both (cogeneration system). A modular sequential approach of these processes used to create the MATLAB program is shown in Figure 4.16.

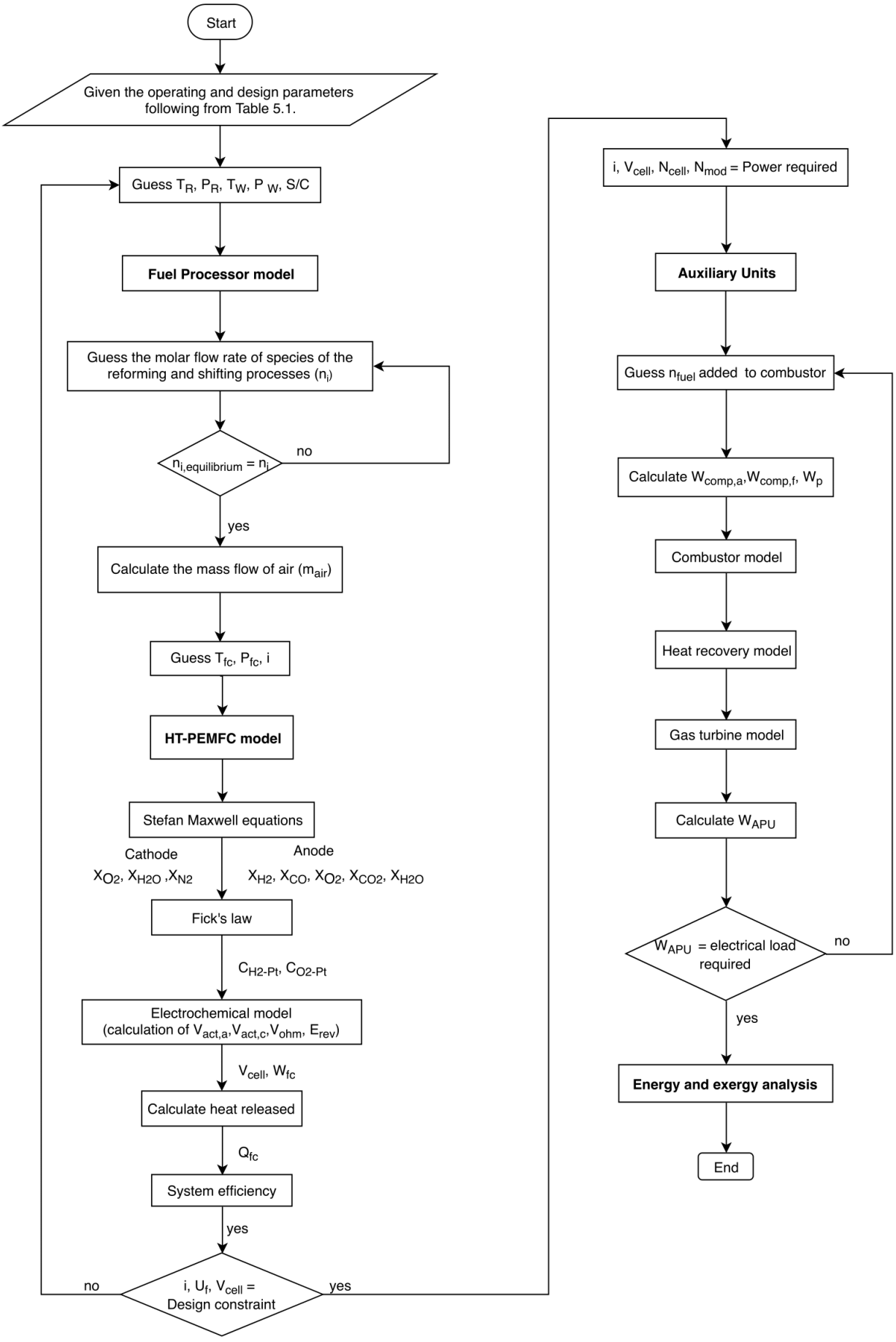

Figure 4.16: Workflow of the created MATLAB program.

Chapter 5

Results and Discussion

This chapter summarizes the results extracted from the simulation of the HT-PEMFC integrated system. Both the Fuel Processor and the HT-PEMFC mathematical models are validated against experimental data. A single point of operation is then selected for the fuel processor and for the HT-PEMFC and its parameters are defined.

In addition, the thermodynamic balances applied to every unit using control volumes are presented, and every node of the APU system is described in detail. HT-PEMFC APU performance is simulated and the first and second law of thermodynamics are calculated. Efficiency evaluation of the overall process and the individual performance of the units are revealed during this chapter.

After defining the system parameters (see Table 5.1) and the design point, the size of the stack and the auxiliary units are estimated to predict the weight of the HT-PEMFC APU proposed in this case study. Preliminary weight estimates the HT-PEMFC most prominent configurations and compares to the conventional APU through a break-even point as a function of stack cell voltage and flight distance.

5.1 Development of Algorithm for Predicting Stack Performance

The cell voltage and system efficiency at different conditions are investigated to result in the most efficient and lightest feasible stack. The MATLAB program presented in 4.16 addresses to analyze the performance of the fuel cell with respect to reformer temperature, reformer pressure, shifting temperature, steam-to-carbon ratio (S/C), fuel cell temperature and fuel cell pressure. The input parameters used in this simulation are defined in Table 5.1.

5.1.1 Fuel Concentration as Functions of Reformer and Shifting Parameters

In this study, the HT-PEMFC is integrated with a fuel processor, so the operating conditions of the reformer and shifting units have a direct impact on the fuel composition that is consumed by the fuel cell as on the performance of the HT-PEMFC APU. The fractions of CO and H_2 are the main focus as they directly influence the fuel cell efficiency, although the reformed fuel contains other components as CO_2, H_2O and CH_4.
The methane steam reforming is an endothermic reaction that occurs at high temperatures (527-627 °C) and the exothermic water gas sifting reaction takes place at low temperatures (177-377 °C).
Table 5.2 provides the final compositions of H_2 and CO for different reforming and shifting temperatures and S/C ratios obtained. From the results, we can conclude that H_2 fraction increases with increasing reformer temperature and the S/C ratio and decreasing shifting temperature. On the other hand, the fraction of CO decreases with the decrease of the reformer temperature and the shifting temperature, and with the increase of the S/C ratio. Nevertheless, a lower S/C ratio results in energy savings in the form of reduced heat input to the reformer and in savings in process steam.

Table 5.1: Parameters used in the simulation of HT-PEMFC stack [65].

Parameters	Value	Unit
GDL thickness, z	0.0002	m
Membrane thickness, l_m	4×10^{-5}	m
Anode film thickness,σ_{anode}	2.5×10^{-9}	m
Cathode film thickness, $\sigma_{cathode}$	1.48×10^{-9}	m
Anode reference exchange current density, $i_{0,a}^{ref}$	1440	$\mathrm{A\,m^{-2}}$
Cathode reference exchange current density, $i_{0,c}^{ref}$	0.0004	$\mathrm{A\,m^{-2}}$
Anode catalyst surface area, $a_{c,a}$	64	$\mathrm{m^2\,g^{-1}}$
Cathode catalyst surface area, $a_{c,c}$	32.25	$\mathrm{m^2\,g^{-1}}$
Anode catalyst loading, $L_{c,a}$	0.2	$\mathrm{mg\,cm^{-2}}$
Cathode catalyst loading, $L_{c,a}$	0.4	$\mathrm{mg\,cm^{-2}}$
Transfer coefficient at anode, α_a	0.5	-
Transfer coefficient at cathode, α_c	0.75	-
Reaction order at anode, κ_a	1	-
Reaction order at cathode, κ_c	1.375	-
Anode reference concentration, $c_{ref,a}$	0.0002	$\mathrm{mol\,cm^{-3}}$
Cathode reference concentration, $c_{ref,c}$	0.0004	$\mathrm{mol\,cm^{-3}}$
Anode activation energy, $E_{c,a}$	16,900	$\mathrm{J\,mol^{-1}\,K}$
Cathode activation energy, $E_{c,c}$	72,400	$\mathrm{J\,mol^{-1}\,K}$
Anode reference cell temperature, $T_{ref,a}$	433.15	K
Cathode reference cell temperature, $T_{ref,c}$	373.15	K

Table 5.2: Hydrogen and carbon monoxide fractions in the synthesis gas obtained from the steam reforming process.

Reformer Temperature [°C]	Shifting Temperature = 177 °C			Shifting Temperature = 277 °C			Shifting Temperature = 377 °C		
	Steam-to-carbon ratio (S/C)			Steam-to-carbon ratio (S/C)			Steam-to-carbon ratio (S/C)		
	3	4	5	3	4	5	3	4	5
H_2									
527	45.77	50.76	53.62	39.00	44.38	48.26	34.17	39.36	43.41
627	55.46	56.67	56.93	52.20	55.12	56.14	48.77	52.65	55.13
CO									
527	0.10	0.08	0.07	0.30	0.28	0.26	0.62	0.61	0.59
627	0.21	0.12	0.08	0.82	0.56	0.41	1.83	1.44	12.92

Another critical parameter to improve fuel processor performance is the pressure of the reforming. This parameter is analyzed maintaining constant the shifting temperature and the S/C ratio while varying the reforming pressure to 1, 2, 3, 5 and 10 atm and the reforming temperature from 527 to 627 °C. For all cases, the shifting temperature and S/C ratio were set to 150 °C and 2, respectively.
From Table 5.3 it can be noted that while the CO_2 fraction decreases slightly with increasing pressure, the fraction of H_2O and CH_4 more than doubled at the reforming temperature of 527 °C and more than tripled at the reforming temperature of 627 °C for a pressure increase of 1 to 10 atm. This is mainly due to the fact that the equilibrium for the chemical reaction (Eq. 4.17) is favored by low pressures as the reaction rate exceeds the production rate and a more balanced reaction occurs.

5.1.2 Effect of Pressure and Temperature on Cell Performance

The performance of the HT-PEMFC depends on the operating pressure and temperature.
Figure 5.1 and 5.2 show the pressure effects on the fuel cell voltage and efficiency, respectively. In this case, the study was carried out at a constant cell temperature of 150 °C evaluating the behavior of the cell at pressures 1, 1.5, 2, 2.5 and 3 atm. The analysis shows that pressure increase clearly makes the H_2

Table 5.3: Analyzing the performance of the fuel processor by varying the pressure parameter.

Pressure [atm]	Refomer Temperature = 527 °C					Refomer Temperature = 627 °C				
	Mole fraction (%)					Mole fraction (%)				
	H_2	CO	CO_2	H_2O	CH_4	H_2	CO	CO_2	H_2O	CH_4
1	61.8	0.15	15.4	15.1	7.5	73.1	0.54	17.9	5.8	2.6
2	55.7	0.09	13.9	20.2	10.1	69.9	0.34	17.2	8.5	4.1
3	51.7	0.06	12.9	23.6	11.8	67.2	0.26	16.7	10.4	5.1
5	46.1	0.04	11.5	28.2	14.1	64.0	0.18	15.9	13.4	6.6
10	38.1	0.02	9.5	34.9	17.5	58.2	0.11	14.5	18.1	9.0

separation through the membrane easier due to the associated enhancement of the permeation driving force, thus increasing cell performance and voltage.

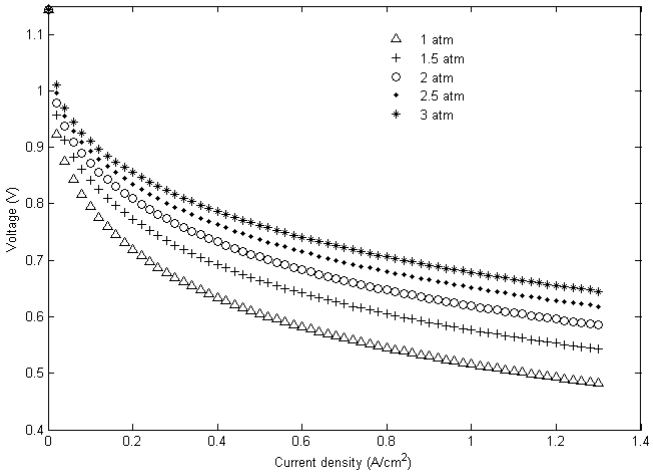

Figure 5.1: Cell performance at constant temperature of 150°C and at pressures of 1, 1.5, 2, 2.5 and 3 atm.

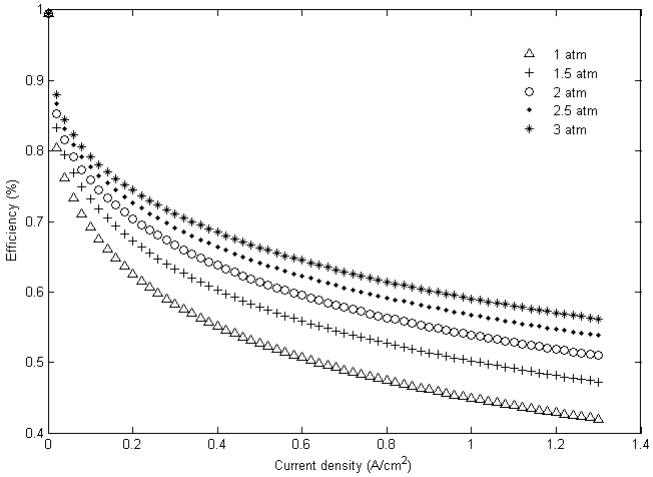

Figure 5.2: Cell efficiency at constant temperature of 150°C and at pressures of 1, 1.5, 2, 2.5 and 3 atm.

The operating temperature of the fuel cell was also evaluated. It is recommended to set the maximum temperature of the fuel cell at 180℃ since operating above this temperature drastically affects the lifetime of the cell [41]. HT-PEMFC uses the proton conducting capabilities of PA in order to conduct protons, as

opposed to water based LT-PEMFCs, this allows operation above 100 °C with the increased boiling point of PA.

Polarization curves are the most commonly used electrochemical method to characterize fuel cells, releasing essential information for the fuel cell analysis. Figure 5.3 presents the polarization curves for temperatures of 150, 160, 170 and 180°C. From simulation results, is verified that the increment of temperature increases the performance of the cell voltage as shown in Figure 5.4. This happens mainly due to an improvement in ionic conductivity with temperature, and is also related to the faster kinetics and greater tolerance to the pollutants achieved at higher temperatures.

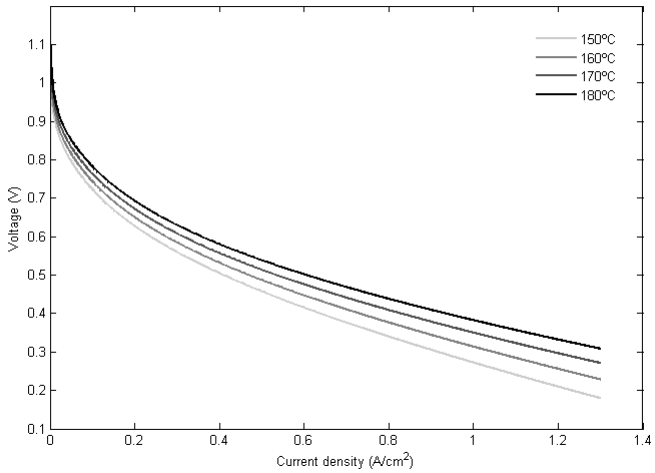

Figure 5.3: Fuel cell voltage at temperatures of 150, 160, 170 and 180°C.

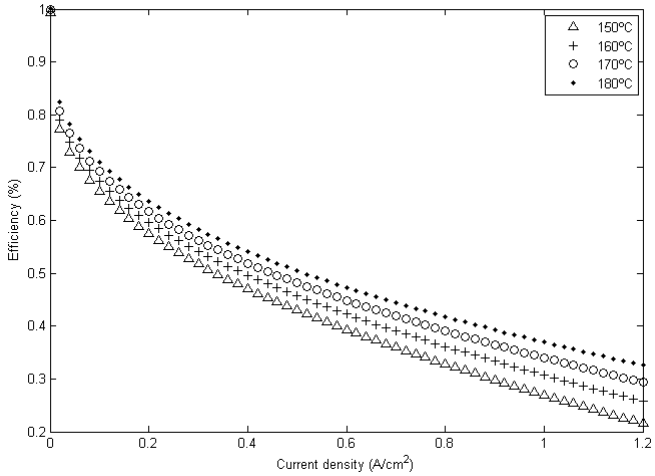

Figure 5.4: Fuel cell performance at temperatures of 150, 160, 170 and 180°C.

It is important to analyze the power density of the fuel cell as it presents one of the most important parameters for stack sizing. Figure 5.5 shows that power density increases with temperature, as expected.

5.1.3 Effects of CO Concentration on Cell Performance

The efficiency of the system depends on the amount of carbon monoxide contained in the fuel when it reaches the HT-PEMFC since it can only handle small amounts of CO. Therefore, it is important to

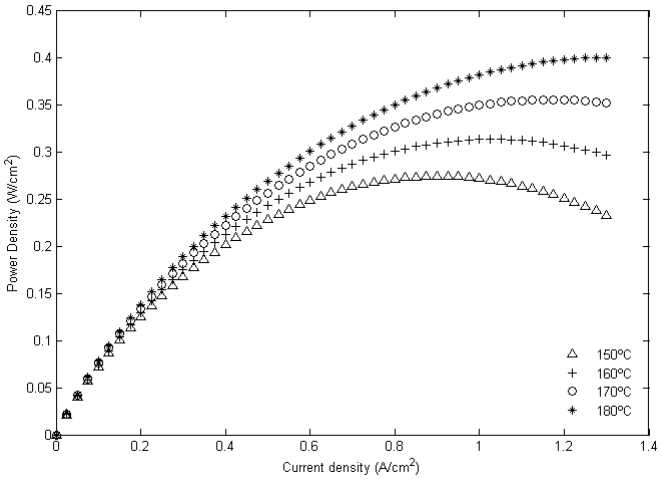

Figure 5.5: Analyzing power density with temperature of 150 ºC, 160 ºC, 170 ºC and 180 ºC.

evaluate the percentage of CO contained in the reformed fuel to assess if it is detrimental to the cell. Figure 5.6 shows the behavior of the fuel cell when supplied with reformed fuel containing different CO concentrations (1%, 2%, 5% and 10%) and pure hydrogen for reference purposes.

It can be stated that increasing CO concentrations result in the decrease of performance, although at low current densities this drop is almost nil and becomes more evident with the increase of current density (above 0.05 A/cm^2). Hence, HT-PEMFC operating on reformed fuel is ideally suited for low current densities as it shows a great CO tolerance, meanwhile pure hydrogen is favorable for high current densities operation. Although HT-PEMFC can operate with high amounts of CO, it is clear in Figure 5.6 how it starts to affect its performance when CO coverage is above 5%.

In addition, tolerance to CO increases with HT-PEMFC operating temperature as demonstrated by Figure 5.7. At 160 ℃, the fuel cell tolerance to 2% and 5% of CO is more sensitive than at 180 ºC, as evidenced by the drop in cell voltage.

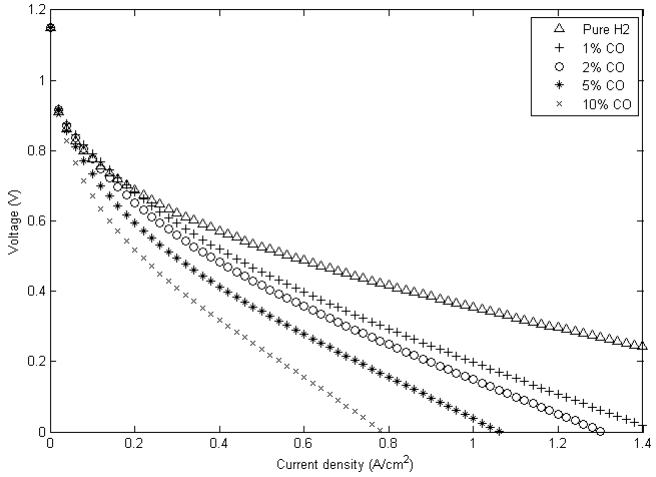

Figure 5.6: Polarization curve with 1%, 2%, 5% and 10% of CO at 160 ºC and 1 atm.

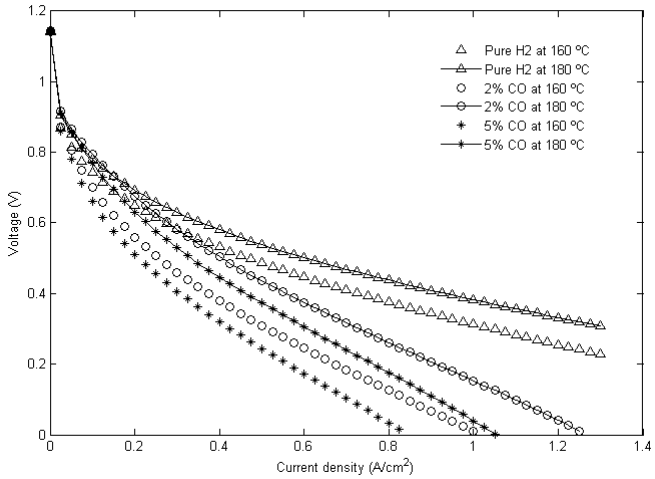

Figure 5.7: CO concentration of 0%, 2% and 5% of CO for temperatures of 160 °C and 180 °C.

5.1.4 Voltage Losses

Ideal cell voltage is not attainable in a real fuel cell. The three major classifications of overpotentials mentioned in Chapter 4 (activation losses at anode, activation losses at cathode and ohmic losses) are deducted from the reversible voltage result in the slope of the open-circuit voltage, as shown in Fig 5.8. At low current densities, the activation polarization dominates, while at average current densities the activation losses start to stagnate and the ohmic losses become more evident.

As evidenced in Eq. 4.60 and 4.61 the aspiration is to maximize the value of the exchange current density in order to minimize activation losses. According to Eq. 4.62 and 4.63, the value of the exchange current density can be increased by increasing the operation temperature, increasing the operation pressure, increasing the roughness of the surface area of the electrodes to increase the active reaction sites, and increasing the reactants concentration to increase the active spots on the electrodes surface area. Dominated by reduction activation losses, mainly because the rate of hydrogen reduction is much slower than the oxidation reaction, leading our focus to increase the exchange current density for the reduction reaction. To minimize the ohmic losses, it is important to design the stack from materials with high conductivities, components with minimum thicknesses, and interconnects with minimum contact resistances through the optimization of the stacks compression pressure. This is particularly important for the electrolyte due to its dominant ionic resistivity. Also, the electrolyte material and the phosphoric acid play a significant role in determining its resistivity and need to be carefully considered.

As seen in Figure fig:temp, a drop in voltage value is expected as a function of generated current. This occurs due to the irreversible internal losses. Fuel cell voltage decreases drastically with increasing current density, causing a considerable decrease in the fuel cell performance, which results of the overlapping of voltage losses shown in Figure 5.8. As expected, voltage losses increase with current density, and activation polarization at cathode have a greater influence.

5.1.5 Model Validation

The fuel cell characteristics obtained from the model and experimental results from Authayanun et al. at different CO conditions are compared in Figure 5.9 [61]. As can be seen in Figure 5.9, there is an acceptable agreement between the model and the experimental results verifying the validity of the model with respect to temperature and CO concentration.

Moreover, in order to verify the fuel processor model, the simulation results were compared with results

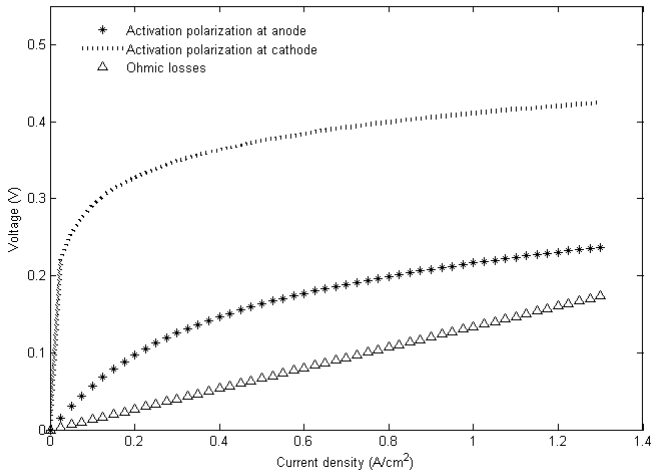

Figure 5.8: Activation polarization at anode, activation polarization at cathode and ohmic losses at 160 °C.

from literature. Two sets of data were selected for this purpose, experimental data by Di Bona et al. [69] and numerical data by Nomnqa et al. [70].
Figure 5.10 compares the simulation, experimental, and numerical results of the dry gas composition at the outlet of the WGS reactor. The simulation results from this work agree well with these data sets.

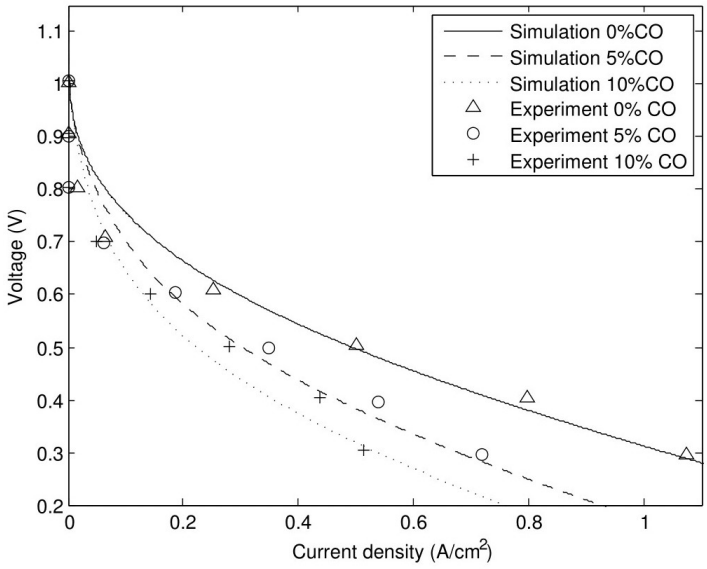

Figure 5.9: Validation of the voltage characteristics of the HT-PEMFC cell for 0%, 5% and 10% CO concentration with experimental results [71].

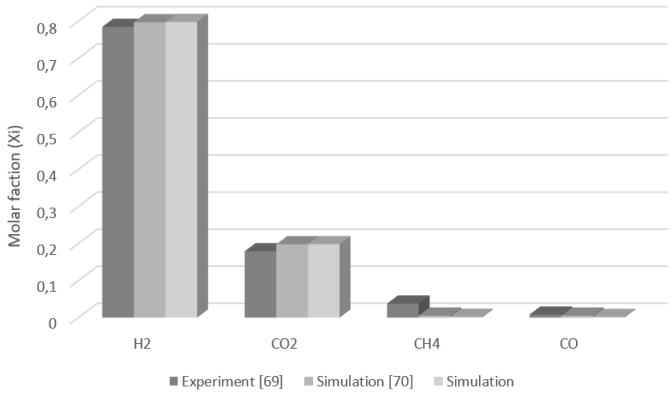

Figure 5.10: Comparison of the experimental and numerical dry reformate gas from the fuel processor.

5.1.6 Design Operating Point

It is essential to select a design point to replace the APU gas turbine with a HT-PEMFC system. This design point represents the operation of a single cell that is the basis for dimensioning the fuel cell stack. The fuel cell stack is the power source of the APU system, so achieving a high power density along with a high cell efficiency is critical.

The maximum power density of the fuel cell increases linearly with temperature, which indicates the benefit of high-temperature operation, as shown in Figure 5.11.

After analyzing several design points by varying the different parameters a single point was chosen with the awareness of the required constraints. In fact, the required constraints such as the CO concentration in the fuel cell anode inlet were met. Results have pointed out that the highest power density of 0.53 W/cm^2 can be achieved for the temperature of 180 °C and at a pressure of 1.5 atm when the CO concentration is 0.1%, which is below the 3% considered admissible to be handled by this type of fuel cells [71].

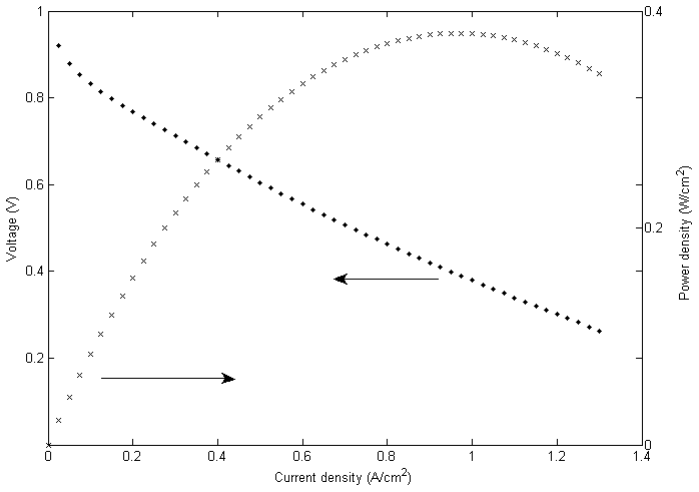

Figure 5.11: Polarization curve and power density curve at 180 °C and 1.5 atm.

Table 5.4 shows the operating conditions and the product compositions of the fuel reforming and shifting processes. An S/C ratio of 3 and reformer temperature of 627 °C have a strong effect on the cell polarization curve, not only when the cell is operating at 180 °C but also at 150 °C.

Table 5.5 presents the input parameters and the results for the stack dimension obtained from the MATLAB program.

Table 5.4: Input parameters and results obtained for the fuel processor.

Parameters	Value	Unit
Input Data		
Reformer Temperature	627	°C
Shifting Temperature	180	°C
Steam-to-carbon ratio	3	
Pressure	1.5	atm
Results		
H_2	64.7	%
CH_4	0.63	%
CO	0.26	%
CO_2	16.0	%
H_2O	18.4	%
Fuel Processor efficiency	91.80	%
Fuel converter ratio	93.36	%

Table 5.5: Input parameters and results obtained for fuel cell stack.

Parameters	Value	Unit
Input Data		
Cell Temperature	180	°C
Cell Pressure	1.5	atm
Cell Area	350	cm^2
Current Density	0.68	$A\,cm^{-2}$
Fuel utilization factor	95	%
Stack Power	262.52	kW
Results		
Cell voltage	0.56	V
Cell overpotential	0.596	V
Cell current	237.7	A
Cell Power density	0.38	$W\,cm^{-2}$
Voltage efficiency	48.35	%

5.2 Thermodynamic analysis

The thermodynamic performance of each of the components introduced in the previous chapter will be analyzed herein.

The molar compositions of the gaseous streams of the system are presented in Table 5.6. Some of these compositions are design data (see Table 3.3), while the remaining result from material balances.

For a clearer understanding of the proposed system, Table 5.7 presents relevant properties calculated through MATLAB routine. These properties are, respectively, values of temperature, pressure, molar and mass flow, enthalpy, energy rate, entropy, entropy rate, exergy, and exergy rate of each flow represented in Figure 3.4. Given its complexity, the system under study was divided into subsystems to perform the thermodynamic analysis. The results of energy, entropy and exergy balances associated with the units are described in Tables 5.8, 5.9 and 5.10.

Table 5.6: Molar compositions of gaseous streams.

Node	Flow	Mole fraction						
		y_{CH_4}	y_{CO}	y_{CO_2}	y_{H_2O}	y_{H_2}	y_{O_2}	y_{N_2}
1	Air	-	-	0.000337	0.0217	-	0.2054	0.77253
2	Fuel	1	-	-	-	-	-	-
4-5	Fuel	1	-	-	-	-	-	-
6-7	Reformed Fuel	0.00632	0.16245	0	0.34387	0.48736	-	-
8	Shifted Fuel	0.00632	0.00258	0.15987	0.18399	0.64723	-	-
9-10	Anode-off gas	0.005666	0.0023106	0.1432	0.8197	0.02900	-	-
11-18	Exhaust gases	-	-	0.1284	0.2425	-	-	0.6291
20	Steam	-	-	-	1	-	-	-
21-22	Air	-	-	0.000337	0.0217	-	0.2054	0.7726
23-24	Cathode-off gas	-	-	0.00031138	0.1722	-	0.1137	0.7138

Table 5.7: Thermodynamic properties of every stream.

i	Description	T [°C]	P [kPa]	$\dot{n}$ [mol/s]	$\dot{m}$ [kg/s]	$\bar{h}$ [kJ/kmol]	$\dot{E}$ [kW]	$\bar{s}$ [kJ/kmol.K]	$\dot{S}$ [kW/K]	$\bar{x}$ [kJ/kmol]	$\dot{X}$ [kW]
1	Air	25	98.94	16.18	0.463	-5.4	-87.1	199.6	3229.6	0.015	0.2
2	Natural Gas	25	101.325	0.74	0.012	-74.9	-55.4	186.2	137.8	831.6	615.4
3	Water	25	101.325	2.20	0.053	-285.8	-628.8	69.9	153.8	900	1980
4	Narutal Gas	69	155.65	0.74	0.012	-73.3	-54.2	187.7	138.9	832.8	616.3
5	Natural Gas	627	155.65	0.74	0.012	-43.7	-32.3	236.6	175.1	847.8	627.4
6	Reformed Fuel + Steam	627	150.98	7.59	0.110	-140.3	-1065.0	214.5	1627.3	109.4	830.3
7	Reformed Fuel	180	146.45	7.59	0.110	-156.8	-1189.6	188.9	1433.4	100.6	763.5
8	Reformed Fuel	180	142.06	7.59	0.110	-159.5	-1210.4	188.2	1428.3	98.1	744.2
9	Anode-off gas	180	126.86	4.89	0.104	-249.9	-1222.5	208.3	1019.0	23.0	112.5
10	Anode-off gas	477	123.05	6.09	0.123	-202.2	-1231.5	231.4	1409.4	187.4	1141.6
11	Exhaust gases	762	119.36	12.09	0.314	-106.6	-1288.8	242.1	2927.0	17.2	207.6
12	Exhaust gases	696	90.17	12.09	0.314	-109.1	-1318.8	240.9	2913.3	15.0	181.7
13	Exhaust gases	571	87.47	12.09	0.314	-113.8	-1375.8	237.0	2865.4	11.5	139.0
14	Exhaust gases	604	87.47	12.09	0.314	-112.6	-1361.0	238.4	2882.6	12.3	148.6
15	Exhaust gases	847	84.84	12.09	0.314	-103.3	-1248.9	248.0	2998.4	18.7	226.2
16	Exhaust gases	613	82.30	12.09	0.314	-112.2	-1357.0	239.3	2893.2	12.4	149.4
17	Exhaust gases	541	79.83	12.09	0.314	-114.9	-1388.9	236.4	2858.8	10.6	127.8
18	Exhaust gases	508	77.43	12.09	0.314	-116.1	-1403.3	235.2	2843.8	9.7	117.9
19	Water	25	153.61	2.20	0.053	-285.8	-628.8	69.9	153.8	900	1980
20	Steam	112	151.58	5.42	0.098	-238.9	-1295.6	226.4	1227.9	1.2	6.7
21	Air	69	155.65	22.18	0.172	-4.1	-90.6	199.9	4433.6	1.2	27.2
21a	Air	69	155.65	16.18	0.463	-4.1	-66.1	199.9	3234.3	1.2	19.8
21b	Air	69	155.65	6.00	0.172	-4.1	-24.5	199.9	1199.3	1.2	7.4
22	Air	180	150.98	16.18	0.463	-0.8	-13.2	208.4	3372.4	2.0	31.6
23	Cathode-off gas	180	126.86	17.53	0.469	-38.4	-673.1	207.9	3644.4	1.8	32.1
24	Cathode-off gas	63	123.05	17.53	0.469	-41.0	-719.3	201.2	3526.6	1.2	21.0

In Table 5.8 are listed the values of lost energy (heat transferred) to the environment on various system units. The remaining units were considered adiabatic. The heat losses to the environment occur in the Water Gas Shifting and the Fuel Cell units.

Table 5.8: Heat transfer rates to the environment in some system units.

Component	$\dot{Q}$ [kW]
WGS	31
Fuel Cell	283
Global	314

Table 5.9 shows the entropy input and output rate values of each control volume, as well as the respective entropy generation rate in that subsystem. The values include the entropy transfers associated with heat losses.

The performance of the systems is influenced by the presence of irreversibilities and the generation of entropy is directly proportional to the magnitude of those irreversibilities. The term entropy generation acquires meaning when one compares its magnitude between the components of the system. The highest degree of entropy generation, and thus irreversibility, occurs in the Fuel Cell, Combustor and Steam Reformer.

When the entropy generation is positive, there are irreversibilities within the system and when it is zero, the process is reversible. In this system, all units are irreversible, with the exception of the water pump that is an ideal process.

Table 5.9: Input, output, and entropy generation rates in every system unit.

Component	$\dot{S}_{in}$ [kW]	$\dot{S}_{out}$ [kW]	$\dot{S}_{gen}$ [kW]
Air compressor	3.230	3.234	0.005
Fuel compressor	0.290	0.355	0.065
Water pump	0.155	0.155	0
HRSG	4.039	4.072	0.033
HX-1	0.279	0.355	0.075
HX-2	0.305	0.804	0.499
HX-3	0.094	0.189	0.095
HX-4	4.160	4.275	0.115
SR	4.226	5.088	0.862
WGS	4.253	4.318	0.066
Fuel Cell	1.817	2.603	0.787
Combustor	2.609	2.927	0.318
Gas turbine	0.547	0.544	0.003
Global	26.00	28.92	2.92

Exergetic and entropic analysis are related since both emerge from the Second Law of Thermodynamics. The loss of exergy in a system with less entropy generation is greater than the loss of exergy in a system that generates more entropy.

The irreversibility or destruction of exergy represents energy that could have been but has not been converted into work. This energy was, for example, lost in the form of heat to the environment.

The highest degree of exergetic destruction and therefore irreversibility occurs in the Fuel Cell, Combustor and Steam Reformer. When the boundaries for unit analysis are at room temperature, the loss of exergy associated with heat transfer is zero and thermodynamic inefficiency consists solely in the destruction of exergy within the control volume.

Table 5.10: Input, output, loss, and exergy destruction rates associated with system units.

Component	$\dot{E}x_{in}$ [kW]	$\dot{E}x_{out}$ [kW]	$\dot{E}x_{dest}$ [kW]
Air compressor	27.498	25.577	1.921
Fuel compressor	1.188	0.868	0.321
Water Pump	1.998	1.998	0
HRSG	64.290	62.751	110.633
HX-1	105.667	83.205	22.462
HX-2	239.634	90.813	148.821
HX-3	56.243	27.896	28.347
HX-4	148.829	102.208	46.622
SR	1516.354	1259.469	256.885
WGS	756.023	744.202	11.821
Fuel Cell	775.824	541.351	234.473
Combustor	1148.931	207.580	941.352
Gas turbine	162.878	162.147	0.731
Global	5005.36	3310.07	1137.03

The major source of irreversibilities is the internal thermal energy exchange associated with high-temperature gradients caused by heat release in combustion reactions. This mechanisms are the Fuel Cell, the Combustion Chamber and the Steam Reformer. The heat exchangers and the HRSG are also components of high exergy destruction.

The irreversibilities are due to the various phenomena, subject to the universal laws of thermodynamics, coupled with the natural degradation of materials and the increase of their disorder, where entropy plays an essential role: friction in all mechanical kinematic components, thermal resistances between components, heat gradients located at unfavorable points in the APU architecture, inefficient mixtures, convection and thermal irradiation in thermodynamic processes, losses through conduction through the materials, among others. When analyzing the components with the major irreversibility, and greater exergy losses, these may be the components where the efficiency of the components can be improved by the introduction of more efficient specific processes, alterations to the designs, reconfiguration of several components, using different materials.

Table 5.11 presents the energetic and exergetic efficiencies of every unit, evaluating this way their performance. The fuel processor efficiency is 91.80%, and the HT-PEMFC integrated system has an efficiency of 41.23%. A detailed exergy analysis system includes an exergy destruction calculation of each component and its comparison with the total system destruction. This exergy destruction quotient, present in Table 5.11, is calculated from Eq. 2.12 and is very useful in comparing the destroyed exergy in the various units of the system. The highest exergy destruction quotient occurs in the Combustion Chamber, followed by Steam Reformer and HT-PEMFC, as suggested in Table 5.10.

The overall results of the base case simulation of the HT-PEMFC APU system are shown in Table 5.12.

Comparing the results with those from Table 2.4, it is plausible to assume that this HT-PEMFC APU system presents a good performance. Nevertheless, further developments are required to achieve efficiencies such as those in the literature.

Exergetic analysis is shown as a useful tool for verifying the components with the major irreversibility and major exergy losses of the proposed APU. This tool is very important in a time where energy and environmental efficiency are urgent and differentiating issues in the current state of society's development. Although we are dealing with a fuel cell set in a cogeneration plant, the inefficiencies detected may be the object of our own use during the design and model of the HT-PEMFC APU, the incorporation of additional systems to recover internal thermal transfers, in order to increase the efficiency of the HT-PEMFC APU.

Table 5.11: Exergy efficiency and exergy destruction quotient of the subsystems and the global system.

Component	ψ (%)	γ_{dest} (%)
Air compressor	88.77	0.16
Fuel compressor	73.00	0.03
Water Pump	100	0
HRSG	41.70	9.30
HX-1	37.98	1.89
HX-2	44.80	12.51
HX-3	74.65	2.38
HX-4	65.93	3.92
SR	65.64	21.60
WGS	98.00	0.99
Fuel Cell	37.47	19.71
Combustor	76.40	23.04
Gas turbine	98.5	0.06

Table 5.12: Base case simulation results of the overall system.

Cell voltage	Net power	Electrical efficiency		Thermal efficiency		Cogeneration efficiency		Degree of thermodynamic perfection
		1st law	2nd law	1st law	2nd law	1st law	2nd law	
0.56 V	262.4 kW	41.23%	39.95%	31.86%	14.46%	61.64%	53.96%	54.88%

For example, the use of the exhaust gases from the turbine so that Steam Reformer, Water Gas Shifting, and the Combustion Chamber maintain their optimal properties to carry out their processes is a good example of that.

5.3 Preliminary Weight Estimates

To investigate the preliminary weight of the HT-PEMFC APU system based on the previously calculated data, a research for units with similar specifications and configurations is performed.

5.3.1 Air Compressor

During the flight envelope, air is compressed to the operating pressure for cruise, take-off, and landing phases and relies on ambient air during the ground phase. Hence, a compressor capable of using ambient air is still required. Compressed air is used as an oxidant in chemical reactions (occurring in the fuel cell and combustion chamber) and the power required to run the compressor is supplied by the turbine.
The air compressor must be able to compress a mass flow of air of 0.64 kg/s and have a compressor ratio of 1.5 atm. The P400-PRO jet engine (see Figure 5.12) compresses 0.67 kg/s of air at a compression ratio of 3.8. The compressor/expander weight is 3.65 kg [72]. For a flight depending only on ambient air, the compressor should be able to compress air at cruise altitude (12,000 m) however the P400-PRO turbine engine can only operate up to 10,000 m. Although it is unclear how accurate maximum altitude and compression ratio is, the compressor/expander weight impact is relatively small, provided that the jet engine used is of similar construction.

Figure 5.12: P400-PRO Turbine Engine [72].

5.3.2 Fuel Pump

The fuel compressor must be able to pressurize the fuel to the system operating pressure of 1.5 atm, in addition to providing the back pressure created by the flow.

A fuel flow rate of 0.021 kg/s (∼1260 ml/min) is required. Each MZR-7205 micro-annular gear pump (see Figure 5.13) is capable of pumping 288 ml/min, hence five pumps operating in parallel provide the required volume capacity. The maximum pressure is 40 bar and the maximum power is 44 W per pump for a total parasitic draw of 220 W per system. Each pump including an integral controller weights 1.08 kg for a total weight of 5.40 kg per system. The four pumps per system approach provided a degree of redundancy in fuel delivery, preventing a single pump failure from shutting down the HT-PEMFC APU system.

Figure 5.13: MZR-7205 micro-annular gear pump [73].

5.3.3 Water pump

Liquid water is pumped to the system to generate steam and react with CH_4 within the reformer unit. Based on steam-to-carbon ratio is possible to calculate the water flow rate required for this system which is 0.053 kg/s (3180 mL/min). Following the previous rationale, the water pump should consist of three 2282-M05X12 micro gear pump (see Figure 5.14), operating in parallel. Each 2252-M05X12 has a maximum flow rate of 1505 mL/min, considering the three pumps in parallel has more than enough volume capacity. The pressure capacity is 15.3 bar, a voltage capacity of 24 V, maximum continuous current of 4.20 A and works with fluid temperature range of -30 to 100 ℃ [74]. With a mass of 300 g per pump for a total weight of 0.90 kg per system. The pump includes a brushless motor configuration.

As the fuel pump, the two pumps per system approach will provide a degree of redundancy on water delivery, preventing a single pump failure from shutting down the power system.

Figure 5.14: 2282-M05X12 water pump [74].

5.3.4 Heat Exchangers

To preheat the fuel to the temperature of the reformer (900 K), to cool the reformed fuel to the shifting temperature (453 K) and to heat the unused fuel from the anode before it enters the combustion chamber, Heat Exchangers must provide the additional source of heat using the exhaust gases from the turbine. Additionally, a Heat Exchanger to preheat the compressed air before it enters the cathode using the excess of air from the fuel cell is required. The heat exchanger mass is calculated by Eq. 5.1 [75].

$$M_{HX} = M_{stp}Q \quad (5.1)$$

where M_{stp} is the specific thermal power of the selected heat exchanger. The heat required for the HX-1, HX-2, HX-3, HX-4 and HRSG are, respectively, 36 kW, 155 kW, 120 kW, 100 kW and 30 kW. The Model Titan AIR, H-1-20A-600 has a specific power of 1 kW/kg [75]. From Eq. 5.1 and the heat required for every heat exchanger we conclude that HX-1 weights 36 kg, HX-2 weights 155 kg, HX-3 weights 120 kg and HX-4 weights 100 kg.

5.3.5 Fuel processor

An integrated fuel processor systems enables fuel cells to operate using a wide range of available fuels ranging from gases (e.g. methane and propane) to conventional liquid fuels (diesel, gasoline and military logistics fuels including JP-8, JP-5, and Jet A) to alternative and unconventional liquid fuels such as biofuels and waste hydrocarbons recovered from industrial processes (e.g. paint solvents).

The fuel processor includes two separate units both used for the production of hydrogen-rich fuel gas: steam reforming and water gas shifting. The obtained hydrogen-rich gas is fed to the HT-PEMFC stack to power the APU. The steam reformer operates at 900 K and 1.5 atm and the WGS operates at 453 K and a pressure of 1.5 atm.

It is important to expose both units to air to obtain a better resistance to degradation. Commercial copper-based WGS catalysts are unsuitable for transportation applications because of the tendency of the catalysts used in these reactors to degrade under the severe conditions encountered in an aircraft. With platinum-based catalyst the WGS shows a long-term tolerance to fuel impurities. From similar uses it is estimated a weight of 15 kg and a volume of 10 L. The reformer uses a catalyst consisting of a small amount of rhodium metal dispersed onto a magnesia-alumina spinel support. The catalyst material is then coated onto a FeCrAlY metal foam. The catalyzed foam for the reformer is expected to require a volume of 15 liters with a weight of 11.3 kg.

Table 5.13: HT-PEMFC cruise full power system results.

	Cruise, 250 kW	
Inlet temperature	180	$^{\circ}\mathrm{C}$
Exit temperature	200	$^{\circ}\mathrm{C}$
Inlet pressure (cathode)	1.42	atm
Exit pressure (cathode)	1.40	atm
Ideal Stack voltage	186	V
Number of cells in a module	333	
Module power density	126.5	$\mathrm{W\,cm^{-2}}$
Module current	1426	A
Number of modules in a stack	6	
Stack heat generated	283	kW
Specific power	0.577	$\mathrm{kW\,kg^{-1}}$
Fuel flow rate	19.12	$\mathrm{kg\,h^{-1}}$
Cathode utilization	44.0	%

5.3.6 Fuel Cell Stack

The APU is sized to provide ground electrical power required by main engines to be started up, electrical energy to be supplied and the air conditioning to be turned on when the engines are shut down and to continue to provide the required electrical load during the cruise phase and in case of an emergency. In addition, the heat generated by the fuel cell is used for heating the cabin. Therefore, the crucial parameter to size the stack is the maximum power that must be delivered, which for this study is 263.16 kW. After selecting the design point, it is time to size the stack. The first step is to calculate the number of cells needed to deliver the ideal stack voltage.

According to the calculated cell voltage of 0.56 V from the selected design point and an ideal stack voltage of 186 V, we concluded from Eq. 3.6 that 333 cells should be combined in series to achieve the operating stack voltage. The second step is to calculate the required number of modules connected in parallel to achieve the target power. From Eq. 3.7, the operating current of the module is established at 1426 A. Thus, six modules placed in parallel can achieve the desired power to supply the A320. The total size of the stack depends on the cell area, the number of cells and the thickness of each cell. From the Antares DLR-H2, we can predict a stack weight of 454 kg [55].

5.3.7 DC/DC Converter

Fuel cell output voltage and current are regulated by the DC/DC converter to maintain a relatively constant voltage at the battery terminals. Adequate control of the output current and power systems is one of the main areas to ensure a long life of the HT-PEMFC APU system.

The DC/DC converter is also managed to avoid excessive fuel consumption of the fuel cell if adequate hydrogen (or reformer) is not available due to reformer status (during load increases, for example). With the increasing size of the aircraft, the hydraulic system and the need for redundant hydraulic distributions constitute a major weight contribution. The fuel cell provides DC power which can be directly provided to power hydraulic systems with electro-hydrostatic actuators, which are self-contained devices where a local electric pump powers a hydraulic actuator, and decrease the need for hydraulic distribution.

DC/DC power supplies can be used to convert power in several applications including avionics and actuators. Figure 5.15, shows the converter model MGV600T11K7 a DC/DC power supply resistant to water. Operates from a 600 VDC input and 270 VDC output. This converter presents a maximum power capability of 11.7 kW and a nominal efficiency of 89%. The device weight is 20.4 kg. For a capability of 250 kW the converter estimated weight is 120 kg.

Figure 5.15: MGV600T11K7 DC/DC converter.

5.3.8 Combustion Chamber

After the gases leave the HT-PEMFC ∼3.3% of the anode gas is directed to the combustion chamber. As the mass required for the turbine to operate both compressors is not sufficient, to the supplied amount of unused fuel and air extra methane is added to the combustion chamber with a flow of 0.019 kg/s.
Weishaupt purflam ® burners (see Figure 5.16) have remarkably low NO_x and CO emissions. The WL5 PB-H 1.24 is a compact burner that operates on a single stage with a capacity range from 28 to 32 kW, a mass flow of 2.4 to 2.7 kg/h and weights 12.9 kg.
The chemical equation that takes place inside the combustion chamber (Eq. 4.92), is herein analyzed based on the different fuel-air-ratios in order to predict the molar fractions of the exhaust gases (CO_2, H_2O N_2 and O_2) for complete combustion. The combustor must deliver targeted emission reductions through more efficient combustion at lower peak temperatures in order to eliminate or significantly reduce NO_x, CO_2, and unburned hydrocarbons. Figure 5.17 shows the results of this analysis, where it is possible to see the increment of the molar fraction of CO_2 and H_2O and the decrease of O_2, while N_2 remains constant as an inert gas does not participate in the combustion reaction. For the purpose of this work is considered the fuel-air ratio for which the oxygen equals zero, which means that λ is equal to 0.59. The gases exhaust the combustion chamber at an adiabatic flame temperature of 1035 K.

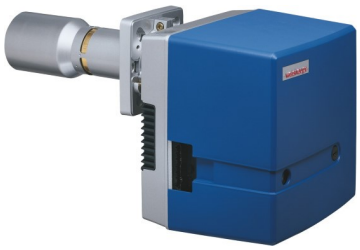

Figure 5.16: Weishaupt Olbrenner WL5 PB-H purflam.

5.3.9 Fuel Tank

The fuel used in the HT-PEMFC is methane. Methane has to be stored in a tank separated from the fuel for the main engines, as they burn jet fuel instead. It is estimated that for a flight from Porto to Amsterdam, the HT-PEMFC APU needs to carry 72 kg of methane onboard of an A320. Considering a tank that weighs 21 kg, the fuel tank system makes a total of 93 kg. Therefore, the positioning of the fuel tank is a critical factor in the design of the aircraft. As a consumable input, the emptying of the tanks can generate an undesirable change of the CG and put the aircraft stability at risk.

5.3.10 Water Tank

There are water tanks already onboard of the airplane, since drinkable water must be carried through the flight. Those tanks carry 200 L of portable water with a flow rate of 50 L/min and usable waste tank with

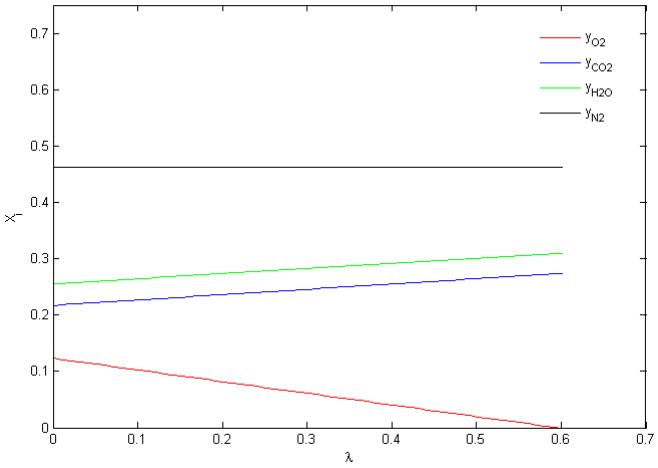

Figure 5.17: Molar compositions of exhaust gases from the combustion chamber.

a capacity of 177 L at the rear of the aircraft. The water will be supplied from the usable waste water tank so there is no need to carry an extra tank and water onboard. A major advantage of the fuel cell is that it produces water (vapor water for HT-PEMFC), which can be used for human consumption after passing through a condenser. This onboard production creates access to water without the need to carry it onboard, saving a lot of weight.
In addition, the water generated by the stack during a flight from Porto to Frankfurt is 487 kg at cruise conditions. This vapor water, could be condensed and used during the flight envelope, but it is out of the scope of the present work. In this case, we consider that the water produced by the stack is expelled with the exhaust gases.

5.4 Integration of the HT-PEMFC into the Airbus A320

Considering the installation of an HT-PEMFC APU on an Airbus A320, it is necessary to establish a balance between the fuel saved by a more efficient power generation system and the additional weight of the aircraft resulting in higher fuel consumption by the main engines, for a particular flight.

- The elimination of the turbine APU implies a saving of weight.
- The HT-PEMFC system efficiency results in a reduction in fuel consumption.
- Weight added to the aircraft by the HT-PEMFC system results in an increase of fuel consumed by the main engines.

The weight distribution of the HT-PEMFC APU system is summarized in Table 5.14. It is notable that the overall weight is dominated by the stacks, the converter and the fuel tank. These components account for 80% of the global mass system.

5.4.1 Fuel Savings due to Efficiency

The prevailing engine generators increase fuel burn at 126 kg/h to produce 250 kW at 18% efficiency evaluated at the 115 VAC bus. The DC power system produces 263.16 kWe for the ± 112 V bus. The fuel economy mass ratio depends on the efficiency of the HT-PEMFC. Table 5.15 provides information on the fuel economy mass ratio for an electric generation before considering the increases in fuel consumption of the main engine resulting from the increase in aircraft weight.

Table 5.14: Mass of every HT-PEMFC APU component considered in this system analysis.

Component	Mass, kg
Air compressor	3.65
Fuel compressor	1.08
Pump	0.90
HX-1	36
HX-2	155
HX-3	120
HX-4	100
HRSG	30
SR	11.3
WGS	15
HT-PEMFC	454
DC/DC Converter	119.62
Combustion Chamber	12.9
Fuel tank	93
Water tank	0
Global	1115

Table 5.15: Mass Rate of Fuel Savings for Electrical Generation. Does not include effect of HT-PEMFC mass.

Efficiency	Fuel Burn Rate in HT-PEMFC APU [kg/h]	Fuel savings for electrical generation over engine generators [kg/h]
85%	9.28	116.71
80%	9.87	116.13
75%	10.53	115.47
70%	11.28	114.72
65%	12.15	113.85
60%	13.158	112.84
55%	14.35	111.64
50%	15.79	110.21
45%	17.54	108.46
40%	19.74	106.26
35%	22.56	103.44

Accordingly, an HT-PEMFC efficiency of 41.29% provides a fuel economy of 106.9 kg/h at the nominal point of 265 kW.
Considering a typical flight from Porto to Frankfurt with a distance of 890 NM (∼1650 km) for the A320 flown in the stratosphere with M_{CR} = 0.78 yields 7174 s flight time and the impact of the HT-PEMFC APU efficiency (without considering the effect of HT-PEMFC APU mass) is 213 kg.

5.4.2 Impact of HT-PEMFC APU Weight on Aircraft Fuel Consumption

Before installing the new HT-PEMFC APU it requires some deinstallations of the current equipment, which can continue to be normally used.
Removing the APU and all Line Replaceable Units (-188 kg) plus removing almost all components, tubes, ducts, and wires only in the tail cone (-73 kg).
The elimination of part of the APU gives a total weight reduction of 261 kg (1.3 times the APU dry weight). Another important aspect is to reuse the maximum existing material from the APU previously installed so it does not go to waste. Therefore, everything from the air intake and the exhaust components are left in place as they are required for the HT-PEMFC APU system.

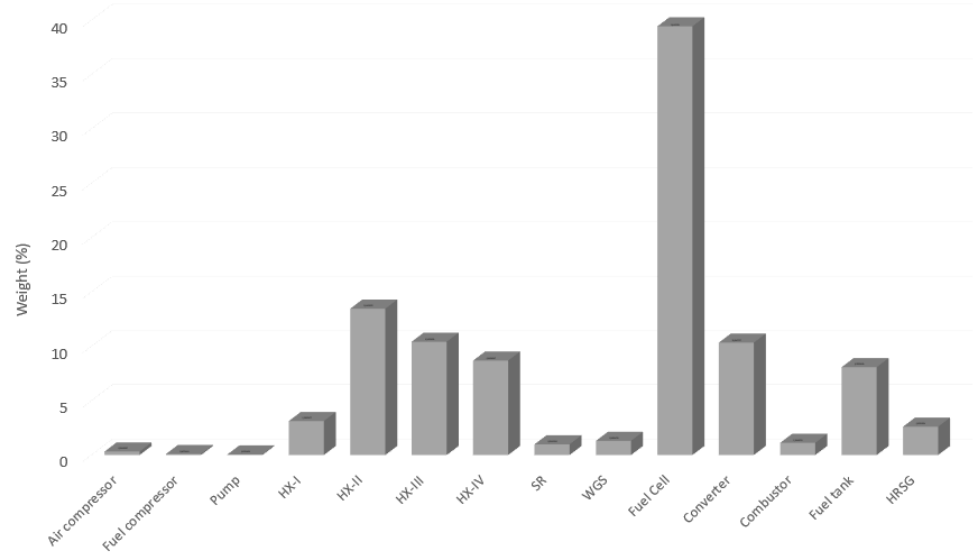

Figure 5.18: Weight percentage of every system unit.

On the other hand, the installation of the HT-PEMFC APU causes a total weight of 1115 kg as demonstrated in Table 5.14.

Figure 5.18 presents in the form of a bar chart the weight percentage of each unit. The HT-PEMFC, the converter, and the heat-exchangers are key players in the weight of the HT-PEMFC APU.

Considering the same flight conditions from Porto to Frankfurt described above, the impact of the HT-PEMFC APU installation weight results in an increase on the aircraft fuel of 16.9 kg when compared to existing generators for the same flight. Additionally, the weight of the fuel needed for the gas turbine to run the flight is removed as the methane used in the HT-PEMFC APU is already being counted.

5.4.3 Break-even Weight

Break-even weight is defined as the weight impact in which the additional fuel consumed by the main engines during a flight, as a result of the HT-PEMFC APU additional weight equals the fuel saved resulting from the higher efficiency of the HT-PEMFC generation system. The break-even weight is a function of the HT-PEMFC efficiency and also varies with the assumed length of the flight used to determine it.

The weight impact to the aircraft needs to account for the mass removed from the aircraft. Based on the conceptual design, the total weight impact of adding HT-PEMFC APU to supply the A320 is 1115 kg. This corresponds to a weight increment of 864 kg (after adjusting for elimination of the APU and reduction in converter weight) when compared to the conventional gas turbine APU.Figure 5.19 represents graphically the difference between the estimated weight impact for the fuel cell design point (0.56 V, 0.68 A/cm^2) and the break-even weight is the estimated weight reduction required to save fuel, which increases with the flight distance. The extent of weight reduction required is less for shorter flights.

In summary, the weight gain of the new APU system accounts for the weight impact of the HT-PEMFC system (1115 kg) and the fuel necessary to transport the mass increment calculated from Eq. 3.1 achieving a value of 61 kg for the considered flight. Meanwhile, the weight loss corresponds to the parts of the gas turbine APU removed (261 kg) and the fuel saved due to the HT-PEMFC APU system higher efficiency (213 kg).

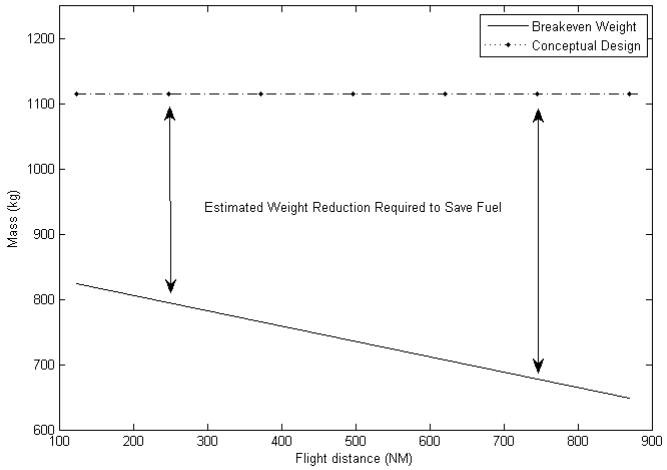

Figure 5.19: Plot comparing the estimated system weight in scoping calculation to the breakeven weight for 1.5 atm, 0.56 V/cell.

5.4.4 Emissions

HT-PEMFC APU burns a small amount of fuel through combustion. This combustion results in CO_2 emissions that contribute to the percentage of pollution by the aircraft. In addition, the weight added to the aircraft by HT-PEMFC not only requires more fuel consumed for a given flight but also results in higher CO_2 and NO_x emissions that must be considered.

In a flight from Porto to Frankfurt the two engines of the A320 are responsible for the emission of 162 kg of HC, 1844 kg of CO and 9147 kg of NO_x. Meanwhile, the HT-PEMFC APU exhausts a total mass of 132 kg of CO_2, derived from the incomplete methane reforming that resulted in the formation of other elements as CO_2, CO and H_2O and the burned fuel in the combustion chamber that is used in the heating system and then exhausted by the exhaust pipe and directly to the atmosphere.

Chapter 6

Conclusions

This study develops an HT-PEMFC system model used as an auxiliary power unit onboard an Airbus A320 and its performance under cruise conditions (12,000 m). This technology provides some benefits over other types of fuel cell systems. Mainly CO tolerance (high fuel flexibility), ease of cooling and no need for humidification. Nevertheless, it presents some inconveniences as long start-up time, faster material degradation, and expensive materials, that need to be considered in an APU application.

The first step was to perform a mathematical model of the fuel cell to investigate how different operating conditions (pressure, temperature, steam-to-carbon ratio, CO concentration) influence the performance of the HT-PEMFC. This was the starting point to explore some parametric modeling techniques. In the context of this work, a fuel processor model and a single-phase, steady state, isothermal one-dimensional electrochemical model were developed. After defining the specific power target output (250 kW), the HT-PEMFC APU system was signed to achieve that need. The aim was to determine the best stack configuration for parameter design, optimize fuel cell performance, and minimize stack weight. The results indicate that under allowed temperature range, an increase in the fuel cell stack temperature tends to increase the efficiency and power output of the system. Moreover, the fuel cell presents better performance at higher pressure, and the concentration of CO has negative effects on the cell above 5%.

The HT-PEMFC requires some auxiliary units, so the next step was to implement them into the system and start to build a conceptual design for the APU. The fuel cell is fueled by natural gas so, is equipped with a fuel reforming process system. Once having a good representation of the system it was important to account for generation possibilities to minimize the irreversibilities. Hence, energy and exergy analysis of the individual components and the overall system were performed. The exergy method enables to account for irreversibilities within the system. The following energy improvement opportunities were used:

- A heat recovering steam generator to reuse the hot exhaust gases from the turbine to produce water vapor for the fuel reforming process, and maintain the reformer and shifting temperature.
- The excess air from the fuel cell was implemented to preheat the inlet air of the cathode.
- The heat produced by the HT-PEMFC is used for cabin heating.

The best performance was generated, with an efficiency of 41.23%, by a cell operating temperature of 180 °C and pressure of 1.5 atm. The heat recovery for cabin heating had the objective of increasing the efficiency of the system and producing the necessary energy for the aircraft, with 69.5% efficiency.
Finally, the system was validated through thermodynamic balance model and, the fuel processor model and the fuel cell mathematical model showed very good agreement with experimental data under various operating conditions.
The exergetic method confirmed its usefulness in the analysis of energy systems. The major irreversibilities were generated by the fuel cell and the combustor chamber with an exergy destruction quotient of 19.71% and 23.04%, respectively.
A mass increment of 854 kg after removing a part of the conventional APU and installing the HT-PEMFC APU was predicted. The impact of this increment is canceled at the break-even point, where the weight

increment for the heavier system is equal to the fuel saved due to system efficiency of 41.23%.
In addition, HT-PEMFC APU promotes the use of renewable fuel in the aviation industry in a way that almost no NO_x emissions, which is not possible in a conventional APU.
In summary, this study allowed us to draw some conclusions regarding the HT-PEMFC APU as an attractive alternative to efficient onboard electrical power for aircraft and fuel consumption, as well as emissions reduction compared to APU gas turbine. Although these approaches achieve good performance there are many difficulties that need to be overcome when it comes to fuel cells. Nevertheless, the application of fuel cells will continue to be an intriguing and vibrant area of research toward the ultimate and ambitious goal: a completely electric aircraft.

6.1 Future Works

For future studies on the subject of a HT-PEMFC design and its thermodynamics evaluation, the following incursions into this theme are recommended:

- Improving the energy exchange efficiency and decreasing the irreversibility of fuel cell to further increase the system efficiency.
- Considering a power turbine system, in order to increase the overall power of the HT-PEMFC APU for a MEA.
- Considering onboard water recovering for onboard use and consumption.
- Development of a system using jet-fuel from the main engines and its fuel processing.
- Perform a computational fluid dynamic analysis of the HT-PEMFC to provide detailed information on the various processes that occur within the fuel cell.
- Analyze of different flow patterns (parallel, spiral, and serpentine) for flow-field design optimization.
- Considering an HT-PEMFC as the propulsion system of an UAV, analyze its performance for different propellers.

Bibliography

[1] D. A. Hensher, "Climate change, enhanced greenhouse gas emissions and passenger transport - What can we do to make a difference?" *Transportation Research Part D: Transport and Environment*, vol. 13, no. 2, pp. 95–111, 2008. 1

[2] A. Anger, "Including aviation in the European emissions trading scheme: Impacts on the industry, CO2 emissions and macroeconomic activity in the EU," *Journal of Air Transport Management*, vol. 16, no. 2, pp. 100–105, 2010. 1

[3] A. Liang, "Emerging Fuel Cell Developments at NASA for Aircraft Applications - Presentation at NASA Glenn Research Center," 2003. 1

[4] M. Gummalla, A. Pandy, R. Braun, T. Carriere, J. Yamanis, T. Vanderspurt, L. Hardin, and R. Welch, "Fuel Cell Airframe Integration Study for Short-Range Aircraft NASA STI Program . . . in Profile," 2006. 1

[5] M. Collares-Pereira and E. d. O. Fernandes, *Energias renováveis, a opção inadiável : contribuição para a definição de uma Política Energética Nacional na Área das Energias Renováveis*, 1st ed. SPES-Sociedade Portuguesa de Energia Solar, 1998. 1

[6] S. Eelman, I. Pozo, D. Poza, and T. Krieg, "Fuel Cell APU's In Commercial Aircraft – An Assessnent Of SOFC And PEMFC Concepts," *24th International Congress of the Aeronautical Sciences (IC)*, pp. 1–10, 2004. 2, 7, 13, 15, 18, 19

[7] T. Hordé, P. Achard, and R. Metkemeijer, "PEMFC application for aviation: Experimental and numerical study of sensitivity to altitude," *International Journal of Hydrogen Energy*, vol. 37, no. 14, pp. 10 818–10 829, 2012. 2, 18, 19

[8] Y. Liu, W. Lehnert, H. Janßen, R. C. Samsun, and D. Stolten, "A review of high-temperature polymer electrolyte membrane fuel-cell (HT-PEMFC)-based auxiliary power units for diesel-powered road vehicles," *Journal of Power Sources*, vol. 311, pp. 91–102, 2016. 2, 13, 14, 17

[9] L. L. Kohout and P. C. Schmitz, "An Analysis of Fuel Cell Options for an All-Electric Unmanned Aerial Vehicle," 2007. 2, 13, 15, 16

[10] A. Matelli, M. D. Almeida, and R. Jose, "Direct ethanol fuel cell as aircraft APU : a study for onboard waste heat recovery," vol. 6, 2018. 2, 12, 13, 15, 16, 22, 28

[11] "The Australian War Memorial." https://www.awm.gov.au/ (accessed February 5, 2019). 5

[12] "Aerotest Limited." https://aerotest.com/ (accessed January 13, 2019). 5, 6

[13] "Air Victory Museum - The Official Site." https://airvictorymuseum.com/ (accessed February 5, 2019). 6

[14] A. Herranz, "The APU and its benefits," *AERTEC Solutions*, 2015. 6, 7, 8

[15] D. Scholz, "An Optional APU for Passenger Aircraft," *5th CEAS Air and Space Conference*, no. 177, pp. 1–14, 2015. 6, 7, 8, 25, 89

[16] G. ho Kim, B. won Lee, H. Lu, and J. hyun Park, "Failure analysis of an aircraft APU exhaust duct flange due to low cycle fatigue at high temperatures," *Engineering Failure Analysis*, vol. 20, pp. 97–104, 2012. 6

[17] "The Deltic Group Inc." http://www.delticgroup.com (accessed June 12, 2018). 6

[18] M. J. Moran and H. N. Shapiro, *Fundamentals of Engineering Thermodynamics*, 2nd ed. Wiley, 2010, vol. 181, no. 4615. 7, 19, 20

[19] "National Aeronautics and Space Administration - NASA." https://www.nasa.gov/ (accessed June 11, 2018). 8

[20] K. M. Spencer and C. A. Martin, "Investigation of Potential Fuel Cell Use in Aircraft," *Institute For Defense Analyses*, no. December, 2013. 8, 15

[21] K. Rajashekara, J. Grieve, and D. Daggett, "Hybrid fuel cell power in aircraft," *IEEE Industry Applications Magazine*, vol. 14, no. 4, pp. 54–60, 2008. 8, 15, 16, 22

[22] S. Carlier, A. Celikel, N. Duchene, C. Eyers, and G. Mepsted, "GAES project: Potential Benefits of Fuel Cell Usage in the Aviation Context," Tech. Rep., 2006. 9, 18

[23] F. Aviation Administration, "Swedish Biofuel Performance Evaluation," Tech. Rep. 9

[24] J. S. Kinsey, M. T. Timko, S. C. Herndon, E. C. Wood, Z. Yu, R. C. Miake-Lye, P. Lobo, P. Whitefield, D. Hagen, C. Wey, B. E. Anderson, A. J. Beyersdorf, C. H. Hudgins, K. L. Thornhill, W. Edward, R. Howard, D. I. Bulzan, K. B. Tacina, and W. B. Knighton, "Determination of the emissions from an aircraft auxiliary power unit (APU) during the alternative aviation fuel experiment (AAFEX)," *Journal of the Air and Waste Management Association*, vol. 62, no. 4, pp. 420–430, apr 2012. 9

[25] P. Lobo, L. Rye, P. I. Williams, S. Christie, I. Uryga-Bugajska, C. W. Wilson, D. E. Hagen, P. D. Whitefield, S. Blakey, H. Coe, D. Raper, and M. Pourkashanian, "Impact of alternative fuels on emissions characteristics of a gas turbine engine - Part 1: Gaseous and particulate matter emissions," *Environmental Science and Technology*, vol. 46, no. 19, pp. 10 805–10 811, 2012. 9

[26] "EASA | European Union Aviation Safety Agency." https://www.easa.europa.eu/ (accessed May 2, 2018). 9

[27] E. M. Gallart, "Design of Auxiliary Power Unit (APU) for co-operation with a turboshaft engine," no. 900625, 2013. 9, 10

[28] E. H. D. Iii and S. Louis, "The Boeing Company," pp. 175–179, 2005. 9, 10, 14

[29] SKYBRARY, "SKYbrary Aviation Safety," 2019. 10

[30] A. Cooper, "Fire aboard empty 787 Dreamliner prompts investigation," 2013. 10

[31] "Lithium-Ion Aircraft Batteries as a Smoke/Fire Risk - SKYbrary Aviation Safety," 2019. 10

[32] "Pneumatic Systems," in *Aircraft Systems*, pp. 239–258. 11

[33] "Aircraft Ground Power Units - A "Flight" Review of the Principal British-made Products," *FLIGHT International*, 1965. 11

[34] F. Kock, "The free piston linear generator," no. August 2012, pp. 1–2, 2014. 12

[35] P. Van Blarigan, "Advanced internal combustion electrical generator," *U.S. DOE Hydrogen Program Review*, no. Williams 1996, pp. 1–16, 2002. 12

[36] M. Graef, P. Treffinger, S.-E. Pohl, and F. Rinderknecht, "Investigation of a high efficient free piston linear generator with variable stroke and variable compression ratio," *22nd International Battery, Hybrid and Fuel Cell Electric Vehicle Symposium and Exposition, EVS 2006*, vol. 1, pp. 116–120, 2006. 12

[37] T. Callahan and S. Ingram, "Free Piston Engine Linear Generator for Hybrid Vehicles Modeling Study," *Advanced Research Projects Agency Arlington, Virginia 22203-1714*, no. May, p. 45, 1995. 12

[38] S. Goto, K. Moriya, H. Kosaka, T. Akita, Y. Hotta, T. Umeno, and K. Nakakita, "Development of Free Piston Engine Linear Generator System Part 2 - Investigation of Control System for Generator," in *SAE Technical Paper Series*, vol. 1, apr 2014. 12

[39] "Fuel Cell Today | The leading authority on fuel cells," 2001. http://www.fuelcelltoday.com/ (accessed March 15, 2018). 13, 16

[40] I. EG&G Technical Services, "Fuel Cell Handbook," vol. 7 Edition, no. November, pp. 1–352, 2004. 12, 15, 20

[41] D. Aili, H. A. Hjuler, J. O. Jensen, and Q. Li, *High Temperature Polymer Electrolyte Membrane Fuel Cells: Approaches, Status, and Perspectives*, [1] D. Aili, H. A. Hjuler, J. O. Jensen, and Q. Li, High Temperature Polymer Electrolyte Membrane Fuel Cells: Approaches, Status and P. 1986., Eds., 1986. 13, 14, 19, 61

[42] S. Buckreub, "DLR Portal," 2016. https://www.dlr.de (accessed June 19, 2018). 14, 15

[43] G. Renouard-Vallet, M. Saballus, P. Schumann, J. Kallo, K. A. Friedrich, and H. Müller-Steinhagen, "Fuel cells for civil aircraft application: On-board production of power, water and inert gas," *Chemical Engineering Research and Design*, vol. 90, no. 1, pp. 3–10, 2012. 14, 18, 28

[44] P. G. Bavarsad, "Energy and exergy analysis of internal reforming solid oxide fuel cell-gas turbine hybrid system," *International Journal of Hydrogen Energy*, vol. 32, no. 17, pp. 4591–4599, 2007. 15, 22

[45] X. Zhang, S. H. Chan, G. Li, H. K. Ho, J. Li, and Z. Feng, "A review of integration strategies for solid oxide fuel cells," *Journal of Power Sources*, vol. 195, no. 3, pp. 685–702, 2010. 15

[46] E. Sciubba and C. Toro, "Modelling and simulation of a hybrid SOFC-GT system for an modelling and simulation of a hybrid SOFC-GT system for an aircraft auxiliary power unit," no. May, 2010. 15, 22

[47] L. F. Brown, "A comparative study of fuels for on-board hydrogen production for fuel-cell-powered automobiles," *International Journal of Hydrogen Energy*, vol. 26, no. 4, pp. 381–397, 2001. 19

[48] N. Dyantyi, A. Parsons, C. Sita, and S. Pasupathi, "PEMFC for aeronautic applications: A review on the durability aspects," pp. 287–302, 2017. 18

[49] J. Kallo, G. Renouard-vallet, M. Saballus, G. Schmithals, J. Schirmer, and K. A. Friedrich, "Fuel Cell System Development and Testing for Aircraft Applications," *18thWorld Hydrogen Energy Conference 2010 - WHEC 2010*, vol. 78, pp. 435–444, 2010. 18

[50] C. Werner, F. Gores, L. Busemeyer, J. Kallo, S. Heitmann, and M. Griebenow, "Characteristics of PEMFC operation in ambient- and low-pressure environment considering the fuel cell humidification," *CEAS Aeronautical Journal*, vol. 6, no. 2, pp. 229–243, jun 2015. 18

[51] L. Blomen and M. Mugerwa, "Fuel Cell Systems Explained," third edition., 2013. 19

[52] J. E. Freeh, C. J. Steffen, and L. M. Larosiliere, "Off-Design Performance Analysis of a Solid-Oxide Fuel Cell/Gas Turbine Hybrid for Auxiliary Aerospace Power," *3rd International Conference on Fuel Cell Science, Engineering and Technology*, no. December, pp. 265–272, 2005. 19, 22

[53] T. Choudhary and S. Krishna, "Thermodynamic Analysis of Solid Oxide Fuel Cell Gas Turbine Hybrid System for Aircraft Power Generation," *SAE Aerospace Congress and Exhibition 2017*, no. May 2000, 2017. 22

[54] G. Genç and S. Sarikoç, "Energy and exergy analysis of a solid-oxide fuel cell power generation system for an aerial vehicle (ISSA- 2015–139)," *International Journal of Green Energy*, vol. 15, no. 3, pp. 151–160, 2018. 22

[55] J. Kallo, "Will fuel cells change the aviation?" 2015. 22, 75

[56] A. H. Fakehi, S. Ahmadi, and M. R. Mirghaed, "Optimization of operating parameters in a hybrid wind-hydrogen system using energy and exergy analysis: Modeling and case study," *Energy Conversion and Management*, vol. 106, pp. 1318–1326, 2015. 22

[57] "Airbus." https://www.airbus.com/ (accessed February 28, 2019). 24

[58] D. Scholz, J. Peterson, and T. Alisch, "An Optiomal APU for Passenger Aircraft Based on the two project reports of," *5th CEAS Air and Space Conference*, 2005. 24

[59] "Rich and Greg's Airplane Page." http://alverstokeaviation.blogspot.com/2016/03/ (accessed March 7, 2019). 25

[60] A. Filippone, *Advanced aircraft flight performance*. Cambridge: Cambridge University Press, 2010, vol. 9781107024. 25

[61] S. Authayanun, M. Mamlouk, and A. Arpornwichanop, "Maximizing the efficiency of a HT-PEMFC system integrated with glycerol reformer," *International Journal of Hydrogen Energy*, vol. 37, no. 8, pp. 6808–6817, 2012. 33, 35, 38, 39, 64

[62] J. M. Keith, *The short-term hydrogen economy : fueling fuel cells from natural gas*. Knovel, 2011. 33

[63] J. C. Slattery and R. B. Bird, "Calculation of the diffusion coefficient of dilute gases and of the self-diffusion coefficient of dense gases," *AIChE Journal*, vol. 4, no. 2, pp. 137–142, jun 1958. 35

[64] F. Barbir, "PEM fuel cells: theory and practice. 2013," *Editorial ELSEVIER*, 2004. 35

[65] M. Mamlouk, T. Sousa, and K. Scott, "A High Temperature Polymer Electrolyte Membrane Fuel Cell Model for Reformate Gas," *International Journal of Electrochemistry*, vol. 2011, pp. 1–18, dec 2011. 37, 60

[66] T. Sousa, M. Mamlouk, and K. Scott, "A non-isothermal model of a laboratory intermediate temperature fuel cell using PBI doped phosphoric acid membranes," *Fuel Cells*, vol. 10, no. 6, pp. 993–1012, 2010. 38

[67] M. M. Mench, *Fuel cell engines*. John Wiley & Sons, 2008. 39

[68] S. McAllister, J.-Y. Chen, and A. C. Fernandez-Pello, *Fundamentals of Combustion Processes*, ser. Mechanical Engineering Series. New York, NY, United States: Springer New York, 2011. 43

[69] D. Di Bona, E. Jannelli, M. Minutillo, and A. Perna, "Investigations on the behaviour of 2 kW natural gas fuel processor," *International Journal of Hydrogen Energy*, vol. 36, no. 13, pp. 7763–7770, jul 2011. 65

[70] M. Nomnqa, D. Ikhu-Omoregbe, and A. Rabiu, "Parametric analysis of a high temperature PEM fuel cell based microcogeneration system," *International Journal of Chemical Engineering*, vol. 2016, 2016. 65

[71] Q. Li, R. He, J.-A. Gao, J. O. Jensen, and N. J. Bjerrum, "The CO Poisoning Effect in PEMFCs Operational at Temperatures up to 200℃," *Journal of The Electrochemical Society*, vol. 150, no. 12, p. A1599, 2003. 65, 66

[72] "P400-PRO Turbine Engine, 89 lbs Thrust, by JetCat, from JetCat, jc-p400-pro - Chief Aircraft Inc." 72, 73

[73] C. R. D. Resende, "HNP Mikrosysteme GmbH," pp. 6–8, 2012. 73

[74] "Model #2252-M05X12, M-Series - Magnetic Drive Gear Pumps On Flight Works, Inc." 73, 74

[75] D. Guida and M. Minutillo, "Design methodology for a PEM fuel cell power system in a more electrical aircraft," *Applied Energy*, vol. 192, pp. 446–456, 2017. 74

Appendix A

Annexes

A.1 Datasheets of estimated APU masses

Table A.1: Estimating the mass of the APU components [15].

Subsystem	Component	Mass [kg]
APU	APU dry mass	-145
	dummy	-15
	APU installation (structure)	-40
fuselage	tail cone (more lightweight design)	60
air	intake	2
	air vane	2
	air inlet with flap	10
	flap actuator	-2
	possible dummy for flap actuator	-0.5
exhaust	exhaust pipe and muffler	10
fuel system	fuel pump	-15
	fuel lines inside the tail cone	3
	fuel lines up to the cross feed valve (including shroud fasteners)	60
oil system	oil	-5
engine control	Electronic Control Box (ECB)	3
	ECB rack	
	electrical wires (incl. fasteners and structure)	15
starter	-	-10
ignition	integrated	
fire detection	1 fire extinguisher (one-shot-system)	-5
and extinguishing	fire pneumatic continuous loop detector	-3
bleed air system	ducts in tail cone	-5
	ducts up to cross bleed valve (including insulation, overheat electric continuous-loop detector and structure)	120
electrical	generator	-25
system	wiring from avionic compartment to starter and generator	90